MODELLING THE BATHYMETRIC INFLUENCE ON ICE MELT FOR AN IDEALIZED ICE-COVERED LAKE

By

Dana Arends

A thesis submitted to the

Department of Civil Engineering

in conformity with the requirements for

the degree of Master of Science (Engineering)

Queen's University

Kingston, Ontario, Canada

September 2024

Abstract

Despite the high abundance of lakes that experience ice cover formation at some point in their seasonal cycle, and the important role frozen lakes play for many communities, winter limnology remains underdiscussed compared to its summer counterpart. Previous work has investigated under-ice physical processes and differential heating to ice covers, but these topics have not been methodically correlated with the shape of the lake. This thesis examines the effect of basin-scale circulation systems interacting with bathymetry on melt rates.

A base setup was tested first, whereby seven cases of a symmetrical truncated cone lake shape with varying side slopes were simulated under idealized radiative forcing. The dominating circulation system in each case consisted of downslope flowing density currents driving lateral transport of heat to the lake interior, with compensating cooler fluid being transported back to the shore at the surface. Based on this persistent system, melting occurred first in the lake centre. The resulting final ice profile was strongly linked to the lake shape for each case.

The effect of Coriolis on the same idealized ice-covered lake was investigated next to better understand the changes as a non-rotating system transitioned to a rotating one. Five cases of decreasing Rossby number (Ro) were simulated for two selected bathymetries. The change to the basin-scale circulation system as Ro decreased involved a strengthening anticyclonic gyre moving outwards in extent with weakening cyclonic motion in the lake interior, and corresponding suppression of lateral heat transport from the density currents. During this transition in circulation regime, the ice melt pattern reversed, revealing greater melting occurring at the lake sides. It was concluded for this idealized ice-covered lake that (1) the effect of convection-driven mixing interacting alone with bathymetry caused the ice to melt inside-out, while (2) the effect of Coriolis on that interaction caused the ice to melt outside-in.

The trend of these effects was reinforced with real bathymetry data from Base Mine Lake, a pit lake located in northeast Alberta. Despite the many differences between the idealized setup and the real lake conditions, the real ice melt compared well with the simulation without Coriolis.

Acknowledgments

I would like to begin by thanking my supervisor Dr. Jason Olsthoorn for his constant guidance and support during my master's degree. His unfailing enthusiasm for fluid mechanics and mathematical modelling, and optimism during the many roadblocks I ran into inspired my confidence as a researcher and excitement for this field. This thesis wouldn't have been possible without the time and patience he dedicated to our brainstorming sessions that made many daunting tasks feel achievable. I am grateful to have worked with him as his first graduate student.

A big thank you to my parents and sisters for their unconditional love and support. I am so grateful for all their encouragement and advice through the years, and for all the laughter, happiness, and fun that distracted me from stressful times in school.

And to Kyle, from spending hours on the phone listening to my long stories about the ups and downs of graduate school, to letting me practice the same presentation to you over and over again, to bringing me dinner and treats while I worked late writing my thesis, I couldn't have made it to the finish line without you.

Table of Contents

List of Figures

List of Tables

List of Symbols and Abbreviations

AEM3D	Aquatic Ecosystem Model 3D
A_1	Visible fraction of non-reflected shortwave radiation
A_2	Infrared fraction of non-reflected shortwave radiation
AMSL	Above mean sea level
C	Scalar concentration
CFL	Courant-Friedrichs-Lewy
CML	Convective Mixed Layer
c_p	Specific heat capacity of water
$\frac{dh}{dt}$	Melt rate
dh_i	Change in blue ice thickness
ELCOM	Estuary and Lake Computer Model
$\epsilon_{\alpha\beta}$	Two-component permutation tensor
f	Coriolis parameter in 2.1; Inertial frequency otherwise
g	Gravity constant
h_n	Depth of each layer n (s = snow, e = white ice, and i = blue ice)
h	Maximum depth
H	Ice thickness
H_{min}	Minimum ice thickness
I_{sw}	Non-reflected shortwave radiation
iWQ	i Water Quality Model
K_n	Conductivity of each layer n (s = snow, e = white ice, and i = blue ice)

K_w	Conductivity of water
L_w	Latent heat of fusion of water
L	Characteristic length scale
M	Melt Rate
NASA LaRC	National Aeronautics and Space Administration Langley Research Centre
PAR	Photosynthetically active radiation
POWER	Prediction of Worldwide Energy Resource
Q_o	Conductive heat flux at the air interface
Q_{si}	Volumetric heat flux produced from the white ice formation
Q_{lw}	Longwave radiation heat flux
Q_s	Sensible heat flux
Q_e	Latent heat flux
Q_r	Rainfall heat flux
Q_f	Ice to water heat flux
Q_w	Water to ice heat flux
Q_{total}	Total non-penetrative fraction of surface flux
$Q_{adv,r}$	Advective heat flux
RANS	Reynolds-Averaged Navier Stokes
RDC	Radiatively Driven Convection
R	Surface radius
r	Bottom radius
Ro	Rossby number
Sc	Scalar sources

T_{md}	Temperature of maximum density
T_f	Freezing temperature of water
T_o	Surface ice temperature
T	Water temperature
T'	Temperature perturbation
$\bar{T}$	Horizontal mean temperature
T_{avg}	Mean temperature of centre r-z slice
T_w	Surface water temperature
T_{air}	Air Temperature
TKE	Turbulent Kinetic Energy
u	Horizontal velocity in x-direction
u_{slice}	Horizontal velocity in direction of slice
u_r	Radial velocity
U	Velocity in 2.1; Characteristic velocity scale in 4.2.3
UNESCO	United Nations Educational Scientific and Cultural Organization
v	Horizontal velocity in y-direction
Y_{slice}	y-coordinates of slice
X_{slice}	x-coordinates of slice
ΔH_{avg}	Average difference in final ice thickness between centre and sides
Δx	Horizontal resolution
Δz	Thermal boundary layer in 3.3.2; vertical resolution in Appendix B
Δt	Time step

η	Water surface elevation
θ_{slice}	Angle of slice with respect to x-axis
κ	Molecular diffusivity
λ_n	Extinction Coefficient of each layer n (s = snow, e = white ice, and i = blue ice)
μ	Gaussian curve mean
ν	Molecular viscosity
π	pi constant
ρ	Density
ρ_0	Reference density
ρ'	Density anomaly
ρ_n	Density of the surface layer n (s = snow, e = white ice, and i = blue ice)
ρ_i	Blue ice density
σ	Gaussian curve standard deviation

Chapter 1 :

Introduction

1.1 Background

It has been estimated that the highest abundance of lakes is found within latitudes of 45°-75° (Verpoorter et al., 2014). At latitudes above approximately 40°, lakes reside in perennial and seasonal ice zones, meaning these lakes will experience intermittent or annual ice formation (Sharma et al., 2019; Kirillin and Leppäranta, 2022). Many of these frozen lakes also play a role for surrounding communities, so knowledge of ice-covered lakes is an important branch of limnology to be explored. Ice cover can have practical purposes such as the use of ice roads in Northern Canada for transportation of food, supplies, and people, as well as the societal and recreational benefits of fishing and skating, and furthermore, ice-covered lakes can also be interconnected with the cultural identity of Indigenous communities (Sharma et al., 2019). As highlighted by Knoll et al. (2019), river and lake ice loss has had consequences in recent decades on cultural ecosystem services and benefits, such as cancellations to spiritual ceremonies, ice fishing and skating events, and postponing to ice road opening days. Although the belief that ice-covered lakes were relatively quiescent under the surface once prevailed, recent decades of research have demonstrated that winter lake conditions can in fact have significant activity relating to ecological processes, water circulation, and interactions with regional and local climates (Yang et al., 2017; Kirillin and Leppäranta, 2022). While the number of studies on the ice season for lakes are growing and expanding our understanding of the dynamic biogeochemical and hydrodynamic processes under-ice, progress in winter limnology is still far

behind the well-documented ice-free season (Kirillin et al., 2012). This lag is likely related to the unique technical challenges for data collection associated with winter field work, such as the cold conditions, unfamiliar methodology for equipment operation and instrument deployment, and safety risks (Block et al., 2019).

Research on ice-covered lakes has gained momentum particularly in response to the growing effect of climate change on ice cover (Kirillin et al., 2012). In the Experimental Lakes Area in northwestern Ontario, a climate sensitivity analysis was performed with a one-dimensional dynamics model on a small boreal lake and found a shifting of the ice cover duration by 18-47 days and decrease in ice thickness of 8-20 cm for the RCP 4.5 and RCP 8.5 climate scenarios (Dibike et al., 2024). Sharma et el. (2021) analysed long-term records of ice phenology for 60 lakes in the Northern Hemisphere and also reported an overall trend of later ice-on dates, earlier ice-off dates, and shorter ice duration, where those specific trends were 6 times faster in the last 25 years than previous years. They concluded that with increasing air temperature in recent decades being such a strong driver of ice dynamics, the projected worsening of climate warming will continue to exacerbate this trend, especially for higher latitude lakes experiencing polar amplification. It is expected that many lakes with seasonal ice cover will transition to have intermittent ice cover, and this crossover was noted to be dependent not only on latitude and altitude, but also lake depth and shape (Sharma et al., 2019). This suggests bathymetry might play an important role in predicting a lake's susceptibility to ice loss from climate change.

At the end of the ice-free period, lake temperatures drop sufficiently for the lake surface to reach its freezing temperature (Kirillin et al., 2012). Typically, mean water temperatures remain above freezing as freshwater lakes have a temperature of maximum density (T_{md}) near

4°C, which causes a unique inverse thermal regime as temperatures cooled below T_{md} form a stable stratification in the surface layer (Kirillin et al., 2012). In a study by Yang et al. (2021), a relationship was established between wind strength, surface area, and mean depth to winter thermal stratification based upon the mixing characteristics during the time between fall overturn when the water column is cooled to 4°C and just before ice-on. They defined a new categorization system identifying lakes as either "cryomictic" or "cryostratisfied", with the former representing a scenario of stronger surface winds resulting in a deeper cold layer or fully mixed water column between 0-1°C, and the latter labelling conditions of weaker wind leading to warmer average temperatures (2-4°C) and a shallower mixed layer (Yang et al. 2021). These stratification regimes tend to persist through the ice-covered period, which will then influence mixing during the warming period.

Ice formation begins once the surface water temperature reaches the freezing point near 0°C (T_f), depending on salt concentration, and will continue to increase in thickness as latent heat is released through conduction from the ice to the atmosphere (Kirillin et al., 2012). The freezing and thaw of ice is largely a vertical one-dimensional problem, with changes to ice depth being dependent on the balance of heat fluxes at the bottom and surface of the ice cover. The most common method for calculating ice growth is based upon Stefan's law that considers the heat flux through an ice sheet with a bottom temperature of T_f and surface ice temperature equal to the air temperature. The resulting integrated ice thickness becomes defined by the square root of negative degree days (see introduction of Ashton, 1989). The cover initially grows at the ice base to form congelation ice ("black ice" or "blue ice"), which is known for its high transparency that can allow nearly 95% transmission of photosynthetically active radiation (PAR) into the water column (Kirillin and Leppäranta, 2022; Hampton et al., 2015). In most lakes, snowfall will

accumulate on the initial ice layers, slowing down ice growth, and possibly causing flooding over top the ice cover if the weight of the snow overcomes the ice buoyancy. This flood water may then also freeze into snow-ice ("white ice") (Kirillin and Leppäranta, 2022). Snow-covered lakes will delay melting as well by reflecting incident light due to its high albedo and providing insulation to the water body because of snow's low heat conductivity properties (Kirillin and Leppäranta, 2022). In summary, the standard picture of ice cover layers consists of the primary ice, superimposed ice (white ice), and snow. The structure and texture of the primary ice layer can form differently depending on meteorological and hydrodynamic conditions, but lakes usually form black ice during calm, cool nights, so this ice type is likely accurate in representing most ice cover bases (Michel and Ramseier, 1971; Kirillin and Leppäranta, 2022). Ice melt is modelled according to the external atmospheric fluxes at the ice surface producing a net gain of heat (Kirillin and Leppäranta, 2022).

These differing ice cover layers (snow, white ice, and black ice) impact how heat is introduced into the water column, and thus motivates the division of the ice-covered period into two key stages: Winter I and Winter II (Kirillin et al., 2012). During Winter I, when snow cover is insulating the lake, the main source of heat to the lake comes from the stored heat in the sediments, which will drive mixing from density currents (Kirillin and Leppäranta, 2022; Kirillin et al., 2012). Winter II assumes the ice cover to be snow-free and more transparent, allowing penetrative solar radiation to drive circulation in a convective mixed layer (CML) (Kirillin and Leppäranta, 2022; Kirillin et al., 2012). Density currents are often produced from bottom heating, but horizontal convection in general develops from littoral warming which could also occur from inflows and penetrative solar radiation in shallow areas (Kirillin and Leppäranta, 2022). Differential heating generated by radiatively driven convection (RDC) has been observed

in lakes to produce a similar circulation response to Winter I with density currents forming in the shallow zones and converging into the centre of the lake (Farmer, 1975; Kirillin et al., 2015; Cortés and MacIntyre, 2020; Ulloa et al., 2019). Despite observations of this under-ice circulation system, the spatial variability in ice thickness during the melting period is not often attributed to the heat converging on the underside of the ice cover.

As an example, Woodcock (1965) studied the cause behind the star-shaped pattern often observed on ice sheets and found it was mostly attributed to the pressure applied by snow cover, which equilibrized via outflowing water from a hole in the ice in a radial pattern. It was inferred that the positions of the melt centres were likely influenced by under-ice convection cells that created leaks in the bottom of the ice cover, but this was not directly measured or observed in the paper (Woodcock, 1965). The same conclusion was drawn by Solarski and Rzetala (2022), who looked at the spatial variability of ice thickness on several temperate lakes in mountainous regions and found it to be a function of only snow cover and air temperature. However, the only inputs they considered were meteorological forcings so no potential relationship could be drawn between their ice thickness observations and any contributions from the water column. Earlier research that also commented on spatial variability of ice was done in the context of the thickness ranges of exclusively white ice and snow free ice (Bengtsson, 1986). In addition to concluding the key factors to be snow cover, snow drift, and exposure to solar radiation, the paper also specifically noted that while velocity and water temperature govern heat flow to the ice, there was not a similar link with water depth (Bengtsson, 1986). Overall, the research on spatial variability of ice has focused on the atmospheric components contributing to melting with only minor comments on the potential contribution of under-ice convection. While the magnitude of heat through the ice surface likely dominates the heat budget, it is still important

not to overlook the heat through the bottom of the ice in the case that feedback between the top and bottom of the ice exists and plays an interesting role in how lake ice melts.

In addition to sediment heating, penetrative solar radiation, and inflows, additional drivers of circulation and mixing in ice-covered lakes include seiching from wind-induced ice oscillations, rotational internal waves, and gyres (Kirillin et al., 2012). For lakes with characteristic horizontal length scales larger than the Rossby radius, Coriolis can play a major role in controlling large-scale rotational flows (Jansen et al., 2021). Furthermore, the significance of Coriolis has been found to increase in winter and be observed in lakes smaller than what would be required for observation in summer (Jansen et al., 2021). In a field study by Forrest et al. (2013), measurements from an autonomous underwater vehicle provided information on density and temperature anomalies that noted the existence of a cyclonic gyre within the convective layer. By evaluating the observations above and below the gyre, it was concluded that vertical transport was being influenced by the gyre (Forrest et al., 2013). In this paper, no other flow feature was discussed as also contributing to the observed circulation pattern, whereas Kirillin et al. (2015) evaluated the flow pattern caused by the combination of horizontal convection and Coriolis. In their study lake, runoff from the surrounding area warmed the littoral zone and formed a moat of open water, and this denser water travelled along the bottom slopes before upwelling into the centre of the lake (Kirillin et al., 2015). The return flow was then subjected to Coriolis forces and formed an anticyclonic gyre (Kirillin et al., 2015). Warm surface runoff is likely an important driver for ice melting along the boundary for many lakes given its warming effect to the littoral region water. Another paper discussing a combination of flow features observed the influence of Coriolis accompanied with density currents generated by sediment heating in a model of both a real lake as well as a simplified conical version (Huttula et

al., 2010). Both simulations displayed the same result of an anticyclonic gyre overlying a cyclonic one. It was also noted that the authors were unclear how the circulation characteristics would be affected by changing the geometry (Huttula et al., 2010). These papers do not directly discuss how ice melt rate is impacted by these flow fields, but there are clear implications for how the transport of heat under these conditions might affect the ice cover.

Research on the bathymetric effects to ice-covered lakes, while not absent, is limited. The influence of lake depth is investigated by Williams et al. (2004) who carried out a statistical analysis of the dependence of climatic, geographic, and bathymetric variables on ice covers. This paper questioned if lake depth or surface area might have any effect on maximum ice thickness using a single and double variable regression and found the relationship was poor, with climatic variables having the most significant influence (Williams et al., 2004). While bathymetric effects are addressed, its effect in relation to the melting period for ice covers is not studied. Williams et al. (2004) only considered the maximum ice thickness, which is likely to be observed soon before melting begins. It's possible closer to ice-off, a stronger bathymetric effect may have been noted. A more recent paper by Ramón et al. (2021) that examined the influence of bathymetric and geographic variables (lake size and latitude) used the Rossby number to incorporate both variables into one parameter, which was then modelled at three different orders of magnitude. This paper found unique velocity fields influenced by Coriolis and commented as well how littoral heating would be affected in each Rossby number scenario (Ramón et al., 2021). While ice melt was not directly discussed, the outcome of the research provides useful information about the bathymetric effects on temperature and velocity currents in a simplified lake model.

In summary, there is non-negligible heat circulation driven by under-ice physical processes, as shown in many other studies, but its effect to the ice melt rate is typically

overlooked or overshadowed by the significance of surface melting effects. The effect of local depth or maximum/mean depth on spatial ice variability and ice differences between lakes has been missing in previous work as well. A discussion of under-ice flow fields and heterogenous ice thickness has not been largely studied in combination with lake bathymetry. The motivation behind investigating the impact of bathymetry is to enhance our understanding of why ice covers melt in certain spatial patterns, where the lake shape is expected to produce an imprint, despite this link not being previously explored. Bathymetry features that alter the heat content in the lake, such as its volume, surface area, and maximum depth are anticipated to influence the overall melt rates due to increasing/decreasing relative contribution of heat flux from the water to the ice heat budget. However, another important aspect of bathymetry is the spatial variability of the bottom contours, which is expected to influence both the heat content in the lake as well as the spatial variability in the ice melt shape. Therefore, the key component focused on for this thesis involved changing the shape of the lake according to local depth.

1.2 Thesis Objectives and Layout

The research question being posed in this thesis is whether bathymetry plays a role in influencing lake currents to trigger an associated melt response in the ice cover distribution. The problem was simplified by modelling a hypothetical midlatitude, midsize ice-covered lake with idealized bathymetry and atmospheric input. This work has the following objectives:

1. Identify the dominant flow feature driving the circulation and heat transport based on the hydrodynamics of the water column
2. Quantify the differential heating subjected to the ice cover and resulting melt pattern caused by the specific identified under-ice flow structure

3. Determine if changes to bathymetry and ice melt response are correlated

This thesis continues with Chapter 2 providing a description of the Aquatic Ecosystem Model 3D (AEM3D) and explanation of ice modelling, as well the important equations used within AEM3D to calculate the ice depth discussed centrally in the subsequent chapters. Chapter 3 presents a base set up of the idealized ice-covered lake simulated with AEM3D and discusses the resulting ice melt derived from the foundational interaction between convection-driven mixing and bathymetry. Chapter 4 extends the numerical study to include the Earth's rotation, broken down in several cases of increasing Coriolis significance, and analyses how the effect of bathymetry and heat transport on ice melt changes across the transition from a non-rotating system to a rotating one. Chapter 5 applies the idealized setup discussed in the earlier chapters to real bathymetry data and compares the results to both the trends observed for the hypothetical bathymetry and satellite images of the real lake's ice melt. Chapter 6 summarizes the work done, major conclusions, and implications of the results. Appendix A goes through a simplified ice budget analysis based on calculated and modelled variables that revealed a bug in the AEM3D ice algorithm that has subsequently been corrected. Finally, Appendix B details the resolutions tests that justify the chosen model set-up.

1.3 References

Ashton, G. D. (1989). Thin ice growth. *Water Resources Research*, *25*(3), 564–566. https://doi.org/10.1029/WR025i003p00564

Bengtsson, L. (1986). Spatial Variability of Lake Ice Covers. *Geografiska Annaler: Series A, Physical Geography*, 68:1-2, 113-121. https://doi.org/10.1080/04353676.1986.11880164

Block, B. D., Denfeld, B. A., Stockwell, J. D., Flaim, G., Grossart, H. F., Knoll, L. B., Maier, D. B., North, R. L., Rautio, M., Rusak, J. A., Sadro, S., Weyhenmeyer, G. A., Bramburger, A. J., Branstrator, D. K., Salonen, K., & Hampton, S. E. (2019). The unique methodological challenges of winter limnology. *Limnology and Oceanography: Methods*, *17*(1), 42–57. https://doi.org/10.1002/lom3.10295

Cortés, A., & MacIntyre, S. (2020). Mixing processes in small arctic lakes during spring. *Limnology and Oceanography*, *65*(2), 260–288. https://doi.org/10.1002/lno.11296

Dibike, Y., Marshall, R., & de Rham, L. (2024). Climatic sensitivity of seasonal ice-cover, water temperature and biogeochemical cycling in Lake 239 of the Experimental Lakes Area (ELA), Ontario, Canada. *Ecological Modelling*, 489. https://doi.org/10.1016/j.ecolmodel.2024.110621

Farmer, D. M. (1975). Penetrative convection in the absence of mean shear. *Quarterly Journal of the Royal Meteorological Society*, *101*(430), 869–891. https://doi.org/10.1002/qj.49710143011

Forrest, A.L., Laval, B.E., Pieters, R. & Lim, D.S.S. (2013). A cyclonic gyre in an ice-covered lake. *Limnology and Oceanography*., 58(1), 2013, 363–375. https://doi.org/10.4319/lo.2013.58.1.0363

Hampton, S. E., Moore, M. V., Ozersky, T., Stanley, E. H., Polashenski, C. M., & Galloway, A. W. E. (2015). Heating up a cold subject: Prospects for under-ice plankton research in lakes. *Journal of Plankton Research*, *37*(2), 277–284. https://doi.org/10.1093/plankt/fbv002

Huttula, T., Pulkkanen, M., Arkhipov, B., Leppäranta, M., Solbakov, V., Shirasawa, K., & Salonen, K. (2010). Modelling circulation in an ice-covered lake. *Estonian Journal of Earth Sciences*, 2010, 59, 4, 298-309. https://doi.org/10.3176/earth.2010.4.06

Jansen, J., MacIntyre, S., Barrett, D. C., Chin, Y., Cortés, A., Forrest, A. L., Hrycik, A. R., Martin, R., McMeans, B. C., Rautio, M., & Schwefel, R. (2021). Winter Limnology: How do Hydrodynamics and Biogeochemistry Shape Ecosystems Under Ice? *Journal of Geophysical Research: Biogeosciences*, *126*(6), e2020JG006237. https://doi.org/10.1029/2020JG006237

Kirillin, G., & Leppäranta, M. (2022). Lake Ice Formation and Melt. Under-Ice Dynamics. In *Encyclopedia of Inland Waters* (pp. 534–545). Elsevier. https://doi.org/10.1016/B978-0-12-819166-8.00003-7

Kirillin, G. B., Forrest, A. L., Graves, K. E., Fischer, A., Engelhardt, C., & Laval, B.E. (2015). Axisymmetric circulation driven by marginal heating in ice-covered lakes. *Geophysical Research Letters*, 42, 2893–2900. https://doi.org/10.1002/2014GL062180.

Kirillin, G., Leppäranta, M., Terzhevik, A., Granin, N., Bernhardt, J., Engelhardt, C., Efremova, T., Golosov, S., Palshin, N., Sherstyankin, P., Zdorovennova, G., & Zdorovennov, R. (2012). Physics of seasonally ice-covered lakes: A review. *Aquatic Sciences*, *74*(4), 659–682. https://doi.org/10.1007/s00027-012-0279-y

Knoll, L. B., Sharma, S., Denfeld, B. A., Flaim, G., Hori, Y., Magnuson, J. J., Straile, D., & Weyhenmeyer, G. A. (2019). Consequences of lake and river ice loss on cultural ecosystem services. *Limnology and Oceanography Letters*, *4*(5), 119–131. https://doi.org/10.1002/lol2.10116

Michel, B., & Ramseier, R. O. (1971). Classification of river and lake ice. *Canadian Geotechnical Journal*, *8*(1), 36–45. https://doi.org/10.1139/t71-004

Ramón, C. L., Ulloa, H. N., Doda, T., Winters, K. B., & Bouffard, D. (2021). Bathymetry and latitude modify lake warming under ice. *Hydrology amd Earth System Sciences*, 25, 1813–1825. https://doi.org/10.5194/hess-25-1813-2021, 2021.

Sharma, S., Richardson, D. C., Woolway, R. I., Imrit, M. A., Bouffard, D., Blagrave, K., Daly, J., Filazzola, A., Granin, N., Korhonen, J., Magnuson, J., Marszelewski, W., Matsuzaki, S. S., Perry, W., Robertson, D. M., Rudstam, L. G., Weyhenmeyer, G. A., & Yao, H. (2021). Loss of Ice Cover, Shifting Phenology, and More Extreme Events in Northern Hemisphere Lakes. *Journal of Geophysical Research: Biogeosciences*, *126*(10), e2021JG006348. https://doi.org/10.1029/2021JG006348

Sharma, S., Blagrave, K., Magnuson, J. J., O'Reilly, C. M., Oliver, S., Batt, R. D., Magee, M. R., Straile, D., Weyhenmeyer, G. A., Winslow, L., & Woolway, R. I. (2019). Widespread loss of lake ice around the Northern Hemisphere in a warming world. *Nature Climate Change*, *9*(3), 227–231. https://doi.org/10.1038/s41558-018-0393-5

Solarski, M. & Rzetala, M. (2022). Determinants of Spatial Variability of Ice Thickness in Lakes in High Mountains of the Temperate Zone—The Case of the Tatra Mountains. *Water*, 14, 2360. https://doi.org/10.3390/w14152360

Ulloa, H. N., Winters, K. B., Wüest, A., & Bouffard, D. (2019). Differential Heating Drives Downslope Flows that Accelerate Mixed-Layer Warming in Ice-Covered Waters. *Geophysical Research Letters*, *46*(23), 13872–13882. https://doi.org/10.1029/2019GL085258

Williams, G., Layman, K.L., & Stefan, H.G. (2004). Dependence of lake ice covers on climatic, geographic and bathymetric variables. *Cold Regions Science and Technology*, 40, 3, 145-164. https://doi.org/10.1016/j.coldregions.2004.06.010.

Woodcock, A.H. (1965). Melt patterns in ice over shallow waters. *Limnology and Oceanography*, 10, R290-R297. https://doi.org/10.4319/lo.1965.10.suppl2.r290

Yang, B., Wells, M. G., McMeans, B. C., Dugan, H. A., Rusak, J. A., Weyhenmeyer, G. A., Brentrup, J. A., Hrycik, A. R., Laas, A., Pilla, R. M., Austin, J. A., Blanchfield, P. J., Carey, C. C., Guzzo, M. M., Lottig, N. R., MacKay, M. D., Middel, T. A., Pierson, D. C., Wang, J., & Young, J. D. (2021). A New Thermal Categorization of Ice-Covered Lakes. *Geophysical Research Letters*, *48*(3). https://doi.org/10.1029/2020GL091374

Yang, B., Young, J., Brown, L., & Wells, M. (2017). High-frequency observations of temperature and dissolved oxygen reveal under-ice convection in a large lake. *Geophysical Research Letters*, 44, 12, 218–12,226. https://doi.org/10.1002/2017GL075373

Verpoorter, C., Kutser, T., Seekell, D. A., & Tranvik, L. J. (2014). A global inventory of lakes based on high-resolution satellite imagery. *Geophysical Research Letters*, *41*(18), 6396–6402. https://doi.org/10.1002/2014GL060641

Chapter 2 :

Modelling Methods

2.1 Description of AEM3D

The Aquatic Ecosystem Model (AEM3D) is a three-dimensional hydrodynamic model based on its well-recognized predecessor, the Estuary and Lake Computer Model (ELCOM), and offers coupling to the iWQ water quality model (Zamani et al. 2020; Hodges and Dallimore, 2022). Applications of AEM3D to lakes and reservoirs include simulating the response of velocity, temperature, salinity, nutrients, and biogeochemistry to a series of forcings such as wind, tides, surface heating and cooling, inflows, withdrawals, bubblers, and mixers (Hodges and Dallimore, 2016). The governing transport equations solved are the unsteady Reynolds-Averaged Navier Stokes (RANS), with the Boussinesq approximation and an assumption of hydrostatic pressure, given by the following equations of momentum and continuity:

$$\frac{\partial U_\alpha}{\partial t} + U_j \frac{\partial U_\alpha}{\partial x_j} = -g\left\{\frac{\partial \eta}{\partial x_\alpha} + \frac{1}{\rho_0}\frac{\partial}{\partial x_\alpha}\int_z^\eta \rho' dz\right\} + \frac{\partial}{\partial x_1}\left\{\nu_1 \frac{\partial U_\alpha}{\partial x_1}\right\} + \frac{\partial}{\partial x_2}\left\{\nu_2 \frac{\partial U_\alpha}{\partial x_2}\right\} + \frac{\partial}{\partial x_3}\left\{\nu_3 \frac{\partial U_\alpha}{\partial x_3}\right\} - \epsilon_{\alpha\beta} f U_\beta \quad (1)$$

$$\frac{\partial U_j}{\partial x_j} = 0 \quad (2)$$

where U is the velocity for three dimensions j = 1, 2, 3 and two α = 1, 2, η is the free-surface elevation, ρ_0 is the reference density, ρ' is the density anomaly, g is gravity, ν is the molecular viscosity, $\epsilon_{\alpha\beta}$ is the two-component permutation tensor, and f is the Coriolis constant (Hodges et al., 2000; Hodges and Dallimore, 2022).

The free surface evolution is calculated by vertically integrating the continuity equation using a kinematic boundary condition,

$$\frac{\partial \eta}{\partial t} = -\frac{\partial}{\partial x_\alpha}\int_0^\eta U_\alpha dz\,. \tag{3}$$

Processes that can be modelled are listed in the user manual as baroclinic and barotropic responses, rotational effects, tidal forcing, wind stresses, surface thermal forcing, inflows, outflows, and the transport of salt, heat, and passive scalars (Hodges and Dallimore, 2016). The transport of scalars, such as temperature, are governed by the following equation, with C representing a scalar concentration, Sc is the scalar sources, and κ the molecular diffusivity:

$$\frac{\partial C}{\partial t} + \frac{\partial}{\partial x_j}\left(CU_j\right) = \frac{\partial}{\partial x_1}\left\{\kappa_1 \frac{\partial C}{\partial x_1}\right\} + \frac{\partial}{\partial x_2}\left\{\kappa_2 \frac{\partial C}{\partial x_2}\right\} + \frac{\partial}{\partial x_3}\left\{\kappa_3 \frac{\partial C}{\partial x_3}\right\} + S_C. \tag{4}$$

AEM3D is run in hydrostatic mode, which neglects the vertical momentum equation with the hydrostatic pressure assumption such that the continuity equation is applied to the horizontal velocity field to compute the vertical velocities. Hydrostatic conditions can significantly reduce run times of the model and are appropriate for small vertical velocities, while resolving vertical acceleration and nonhydrostatic pressure in nonhydrostatic mode are important in adequately capturing small-scale internal waves and convective processes (Wadzuk and Hodges, 2004; Parsapour-Moghaddam and Rennie, 2017).

Heat exchange between the water surface and the atmosphere is defined by the non-penetrative (longwave radiation, sensible heat, and evaporative heat) and penetrative (shortwave radiation) components (Hodges and Dallimore, 2022). AEM3D follows a 7-stage numerical time-stepping scheme, which was adapted from Casulli and Cheng (1992). This begins with either heating or cooling of the surface layer, then the mixed-layer model is applied for mixing of scalar concentrations and momentum, if wind energy is introduced, it is applied in the wind-mixed layer as a momentum source, and next, changes to the free-surface and velocity field are

solved (Hodges and Dallimore, 2022). The remaining steps involve horizontal diffusion of momentum and scalars, and advection of scalars (Hodges and Dallimore, 2022). The Cartesian grid is comprised of rectangular cells that can have variable vertical spacing while the horizontal spacing is fixed as uniform, with scalar concentrations and the free-surface height computed at the cell centre and velocities defined at the cell face following the Arakawa-C grid system (Hodges et al. 2000). The mixing model in AEM3D for vertical turbulent closure is based on turbulent kinetic energy (TKE), where the vertical mixing is modelled with a separate 1D model for turbulent transport in each water column and a 3D approach for capturing the transport of TKE (Hodges and Dallimore, 2022). The 3D mixed-layer model determines the viscosity and diffusion terms in the momentum and scalar transport equations (1) and (4) based on the mixing energy budget (Hodges and Dallimore, 2022).

2.2 AEM3D Ice Model

2.2.1 Theoretical Background

The ice model in AEM3D couples the surface-layer thermodynamics model with the hydrodynamics to solve the steady-state heat conduction equation between three layers: blue ice, white ice, and snow. The equation consider conditions from the atmosphere above the ice layers and the water column below to calculate ice depths at each horizontal location of the grid (Oveisy et al., 2012). Ice formation begins when the water surface reaches freezing temperatures (T_f) and continues to grow at the ice-water interface from imbalances between the latent heat of freezing released from the ice bottom to the atmosphere (through the ice layers) and the heat flux from the water body to the ice (Oveisy et al., 2012; Leppäranta, 2015). Snow will initially accumulate directly on top of the blue ice until its weight exceeds the ice's buoyancy, and water

will flood the snow on the surface to form white ice (Oveisy et al., 2012). Ice growth does not occur at the surface, only at the ice-water interface where the ice temperature is fixed at the freezing temperature T_f. Cooling at the surface only results in a decrease to the upper surface ice temperature (T_o), where the surface refers to the air-ice interface (Patterson and Hamblin, 1988). However, ice melting occurs both at the surface and the ice-water interface, with the surface melting dependent on both the meteorological fluxes and the heat conduction at the air interface (Patterson and Hamblin, 1988). The surface melting flux is controlled by an equilibrium condition, which states that when the surface temperature of the ice is less than the freezing temperature ($T_o < T_f$), the total flux at the surface will be zero (Patterson and Hamblin, 1988). If this is not in equilibrium, a net heat loss in the ice surface, and subsequent decrease to ice thickness, must occur to appropriately adjust the ice temperature back down to T_f (Patterson and Hamblin, 1988). When surface warming occurs, the ice temperature can only be raised until it reaches the melting temperature, at which point any excess heat will be spent on surface melting, thus decreasing the blue ice depth (Patterson and Hamblin, 1988). Simultaneously, changes in ice thickness can occur at the bottom from imbalanced fluxes when warming water temperatures cause the heat flux from the water to the ice to become greater than the flux from the ice to the water (Oveisy et al., 2012; Leppäranta, 2015). The ice layers and heat fluxes considered in the model are shown in Figure *2-1* below. Note T_o is defined here to represent a general ice temperature at the ice-air interface.

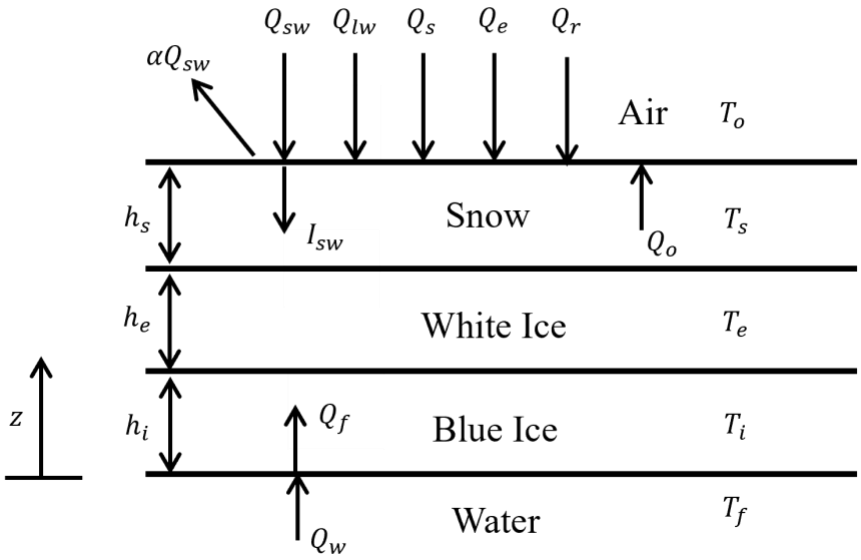

Figure 2-1. Schematic of ice layers, heat fluxes, and temperatures for the ice model (adapted from Oveisy et al., 2012).

The heat transport equations implemented in the AEM3D ice model are based on those described in Oveisy et al. (2012), which improved the model given in Rogers et al. (1995) to be coupled with the Estuary and Lake Computer Model (ELCOM), the precursor to AEM3D. Rogers et al. (1995) first established the three-layer model following the two-layer steady-state heat conduction equations that Patterson and Hamblin (1988) developed to separate the incident solar radiation into visible and infrared spectral bands. With application of the temperature continuity and heat flux boundary conditions, and the assumptions of steady-state and negligible ice/snow cover advection, the solution to the heat conduction equation becomes,

$$\left(\frac{h_s}{K_s}+\frac{h_e}{K_e}+\frac{h_i}{K_i}\right)(Q_o-I_{sw})=\left(T_f-T_o\right)-A_1I_{sw}\left[\frac{1-\exp(-\lambda_{s1}h_s)}{K_s\lambda_{s1}}+\exp(-\lambda_{s1}h_s)\frac{1-\exp(-\lambda_{e1}h_e)}{K_e\lambda_{e1}}+\right.$$
$$\left.\exp(-\lambda_{s1}h_s-\lambda_{e1}h_e)\frac{1-\exp(-\lambda_{i1}h_i)}{K_i\lambda_{i1}}\right]-A_2I_{sw}\left[\frac{1-\exp(-\lambda_{s2}h_s)}{K_s\lambda_{s2}}+\exp(-\lambda_{s2}h_s)\frac{1-\exp(-\lambda_{e2}h_e)}{K_e\lambda_{e2}}+\right.$$
$$\left.\exp(-\lambda_{s2}h_s-\lambda_{e2}h_e)\frac{1-\exp(-\lambda_{i2}h_i)}{K_i\lambda_{i2}}\right]+Q_{si}h_s\left(\frac{h_s}{K_s}+\frac{h_e}{K_e}+\frac{h_i}{K_i}\right)+\frac{Q_{si}h_s^2}{2K_s}, \quad (5)$$

where the subscripts refer to s = snow, e = white ice, and i = blue ice, h_n is the depth of each layer, Q_o is the outward conductive heat flux at the air interface, I_{sw} is the nonreflected shortwave radiation with A_1 and A_2 the fraction divided into visible and near infrared, respectively (I_{sw} can also be separated into ultraviolet light in AEM3D for the water quality model), and λ_n is the attenuation coefficient for each spectral band and each layer. Q_{si} is the volumetric heat flux produced from the white ice formation and K_n is the thermal conductivity of each layer (Oveisy et al., 2021).

At the top of the frozen layer, the surface flux condition for regulating the ice temperature is given by the heat balance:

$$Q_{total}=Q_o+Q_{lw}+Q_s+Q_e+Q_r=\begin{cases}0 & T_0<T_f\\ \rho_nL_w\frac{dh_n}{dt} & T_0=T_f\end{cases} \quad (6)$$

where Q_{lw}, Q_s, Q_e, Q_r are the fluxes from longwave radiation, sensible heat, latent heat, and rainfall, respectively, which make up the non-penetrative fraction of the total surface flux. If melting occurs, ρ_n refers to the density of the surface layer and L_w is the latent heat of fusion of water. There is no condition for $T_0 > T_f$ because the model forces T_0 to equal T_f and uses the excess total flux to trigger melting.

At the blue ice-water interface, the accretion and ablation of the ice is calculated:

$$\frac{dh_i}{dt} = \frac{Q_f - Q_w}{\rho_i L_w}, \tag{7}$$

$$Q_f = Q_o - A_1 I_{sw}[1 - \exp(-\lambda_{s1} h_s - \lambda_{e1} h_e - \lambda_{i1} h_i)] - A_2 I_{sw}[1 - \exp(-\lambda_{s2} h_s - \lambda_{e2} h_e - \lambda_{i2} h_i)], \tag{8}$$

$$Q_w = -K_w \frac{dT_w}{dz}, \tag{9}$$

where Q_f is the flux from the ice to the water and Q_w is the flux from the water to the ice, which is based only on the temperature gradient across the thermal boundary layer between the water surface and ice bottom (defined as a default value of 0.039 m in AEM3D).

For this thesis' use of the ice model, precipitation (rainfall and snow) is not considered, reducing the equations to no longer consider the snow or white ice layers. The expressions for the outward conductive heat flux at the air interface (Q_o) and the flux from the ice to the water (Q_f) can therefore be simplified to,

$$Q_o = \frac{(T_f - T_o) - I_{sw} A_1 \left(\frac{1-\exp(-\lambda_{i1} h_i)}{K_i \lambda_{i1}}\right) - I_{sw} A_2 \left(\frac{1-\exp(-\lambda_{i2} h_i)}{K_i \lambda_{i2}}\right)}{\left(\frac{h_i}{K_i}\right)} + I_{sw}, \tag{10}$$

and

$$Q_f = Q_o - I_{sw} A_1 (1 - \exp(-\lambda_{i1} h_i)) - I_{sw} A_2 (1 - \exp(-\lambda_{i2} h_i)) \ . \tag{11}$$

2.2.2 Source Code Details

The model specifies an ice thickness initialisation value of 0.001 m and an initial condition for ice temperature of T_f. That is, when the surface water temperatures become equal or less than T_f, the blue ice depth is assigned an instant value of 0.001 m.

In the ice thermodynamic subroutine, the ice surface melt and ablation formulas (equations 6-7) are applied, which both follow the same general process: once the net heat flux is used to estimate a change in ice depth, if this step decrease to ice depth is greater than the current ice depth, the ice depth is set to zero, otherwise the change in depth is subtracted from the current ice depth. For both conditions, a flux representing the equivalent water volume of melted ice returned to the water column is determined. In short, there is no restriction to step increases during accretion, but the step size is limited by ice thickness during ablation.

The first step of the code is to find the root of equation 6 using bisection with an initial ice temperature estimate of $T_0 = 15℃$ and upper and lower bounds of 20°C and -50°C, respectively. Q_{total} is iteratively solved by summing all the fluxes given in equation 6, with Q_o calculated according to the ice temperature estimate (equation 10). To complete the iteration, the following conditions must both be satisfied: $Q_{total} < 1$ and the difference between the upper and lower temperature bounds <0.001. If $Q_{total} \leq 0$, the ice temperature estimate is set as the new upper temperature bound and if $Q_{total} > 0$, then the ice temperature estimate becomes the lower temperature bound.

After solving equation 6, the code checks whether the ice temperature is above zero. Under freezing conditions, this check will not be necessary, and the iteration will continue re-estimating a negative ice temperature until the convergence limits are reached. Under melting conditions when Q_{total} cannot reach zero without T_0 exceeding T_f, the temperature check loop will force $T_0 = T_f$, and recalculate equation 6 accordingly. The resulting imbalance to Q_{total} will then be used to calculate a melt rate that reduces the total ice depth. Regardless of whether the temperature check is performed, the last part of this overall loop is to calculate Q_w and Q_f (equation 9 and 11) based on the final iterated Q_o (equation 10).

In summary, under freezing conditions, Q_{total} is iterated to equal zero because the ice temperature is allowed to be negative, so this results in zero melt rate contribution from the surface, which makes sense because freezing only takes place from the ice-water bottom interface (Patterson and Hamblin, 1988). However, under melting conditions, the surface temperature of the ice ($T_0 = T_f$), and any residual of Q_{total} is used to calculate surface melting.

If freezing is occurring, AEM3D will output negative ice temperature values and $Q_{total} < 1$, and if melting is occurring, AEM3D will output T_0 = 0 and $Q_{total} > 0$.

The equations and process discussed above were examined through test simulations of a cylinder bathymetry with constant winter and spring conditions (run separately) to compare calculated and modelled parameters. In doing so, a minor bug was identified in the ice code that is detailed in Appendix A.

2.3 References

Casulli, V., & Cheng, R. T. (1992). Semi-implicit finite difference methods for three-dimensional shallow water flow. *International Journal for Numerical Methods in Fluids*, *15*(6), 629–648. https://doi.org/10.1002/fld.1650150602

Hodges, B., & Dallimore, C. (2022). Aquatic Ecosystem Model: AEM3D, Hydrodynamics Science Manual. Hydronumerics: Docklands, Australia

Hodges, B., & Dallimore, C. (2016). Aquatic Ecosystem Model: AEM3D, User Manual. Hydronumerics: Docklands, Australia

Hodges, B. R., Imberger, J., Saggio, A., & Winters, K. B. (2000). Modeling basin-scale internal waves in a stratified lake. *Limnology and Oceanography*, *45*(7), 1603–1620. https://doi.org/10.4319/lo.2000.45.7.1603

Leppäranta, M. (2015). Freezing of Lakes and the Evolution of Their Ice Cover; *Springer*: Heidelberg, Germany, 2015; pp. 91–129.

Oveisy, A., Boegman, L., & Imberger, J. (2012). Three-dimensional simulation of lake and ice dynamics during winter. *Limnology and Oceanography,* 57(1), 43-57, doi:10.4319/lo.2012.57.1.0043

Parsapour-Moghaddam, P., & Rennie, C. D. (2017). Hydrostatic versus nonhydrostatic hydrodynamic modelling of secondary flow in a tortuously meandering river: Application of Delft3D. *River Research and Applications*, 33(9), 1400–1410. https://doi.org/10.1002/rra.3214

Patterson, J. C., & Hamblin, P.F. (1988). Thermal simulation of a lake with winter ice cover. *Limnology and Oceanography,* 33: 323–338, doi:10.4319/lo.1988.33.3.0323

Rogers, C. K., Lawrence, G.A., & Hamblin, P.F. (1995). Observations and numerical simulation of a shallow ice-covered midlatitude lake. *Limnology and Oceanography*, 40(2), 374-385, doi:10.4319/lo.1995.40.2.0374

Wadzuk, B. M., & Hodges, B. R. (2004). Hydrostatic and Non-hydrostatic Internal Wave Models. *Center for Research in Water Resources*, University of Texas at Austin

Zamani, B., Koch, M., & Hodges, B. R. (2020). Effects of morphology in controlling propagation of density currents in a reservoir using uncalibrated three-dimensional hydrodynamic modeling: Effects of morphology in propagation of density currents. *Journal of Limnology*, 79(3). https://doi.org/10.4081/jlimnol.2020.1942

Chapter 3 :

The Influence of Bathymetry on Ice Melt for an Idealized Ice-Covered Lake

3.1 Introduction

Most lakes are covered in ice for part of the year (Verpoorter et al., 2014; Kirillin and Leppäranta, 2022). Frozen lakes are intertwined with many societal, cultural, and recreational uses and are invaluable to the communities that rely on and benefit from them (Sharma et al., 2019). With projected climate warming, the trend of shortening ice seasons is expected to continue and some lakes in the Northern Hemisphere may even transition from having annual winter ice to intermittent ice cover (Sharma et al., 2019). Ice loss has noteworthy consequences to cultural ecosystem services and benefits, where climate variability in recent decades has contributed to the inability to use river and lake ice for ceremonial, skating, fishing, and transportation related activities in the same ways as the past (Knoll et al., 2019). This threat to lake ice has driven more interest towards research in winter limnology, but there are still many unanswered questions to explore (Kirillin et al., 2012). Sharma et al. (2019) noted that each lake's response to increasing air temperatures will be different, with mean depth, elevation, and shoreline complexity playing a significant role in dictating the likelihood of ice loss. Though under-ice conditions were once believed to be more stagnant, recent work has shown how heat fluxes through the ice can drive water circulation (Kirillin et al., 2012; Yang et al., 2017). Given that lake depth and shape are defining features for ice loss susceptibility, there is need to better understand how bathymetry influences circulation and warming to the ice cover.

The importance of solar radiation in driving mixing in ice-covered lakes has been discussed in previous work. Farmer (1975) observed radiatively driven convection (RDC) causing mixed layer deepening in an ice-covered lake though density currents plunging into the stable fluid below. Depending on the solar radiation intensity, ice extinction coefficient, and initial water temperature profile, solar radiation can be significant enough to spur penetrative convection (Matthews and Heaney, 1987). Mixed layer warming has been modelled both with (Ulloa et al., 2019) and without (Farmer, 1975; Mironov et al., 2001) the consideration of horizontal fluxes from gravity currents. Ulloa et al. (2019) modelled RDC in an ice-covered lake with sloping sides and determined that the contribution of heat from shallow areas to the centre was important in closing the heat budget of mixed layer warming, and that lake shape controlled the relevance of this lateral heat transport. In the later stages of winter when the snow layer has effectively disappeared and RDC dominates, this process will govern the vertical temperature structure under the ice.

Further, solar radiation can play a key role in three mechanisms of ice melt: absorption into the ice interior, atmospheric warming which results in increased heat flux from the air to the ice surface, and heat flux at the ice base from the water layer warmed by RDC (Kirillin and Leppäranta, 2022). Spatial variability to the ice cover can thus be associated with nonuniform surface and interior ice cover characteristics (i.e., snow drift, albedo feedback, extinction coefficients), or nonuniform water temperature distribution. This chapter focuses exclusively on the nonuniform melting response to under-ice processes, with the idealized scenario of spatially uniform meteorological conditions. The intention of this set up is to quantify the melting resulting from differential heating of the lake. Certain melting patterns are driven by weather such as pressure effects from snow cover contributing to the star-shaped pattern observed in

several freshwater ponds and lakes (Woodcock, 1965), while others can be driven by under-ice processes unique to a lake, such as the ice rings observed in Lake Baikal for decades formed from anticyclonic eddies (Kouraev et al. 2016). It is for cases where annually repeating melting patterns that cannot be easily explained by atmospheric conditions that understanding heat transport in the water column becomes especially useful. Lakes are naturally dynamic systems, though some characteristics remain unchanging on shorter year-to-year timescales, such as its morphometry, latitude, and altitude. These lake characteristics would innately interact with other physical, chemical, and biological properties of a lake. The importance of lake shape to ice melt is expected to be based on two aspects: changes to the magnitude of heat flux from the water to the ice heat budget and spatial variability in the ice melt shape due to varying lake depths. Previous work has established the relevance of under-ice physical processes in transporting heat, but there is a missing connection between how the shape of a lake might interact with these currents to induce the melting patterns observed at the surface. This work aims to simplify the situation to derive a foundational understanding of bathymetry's influence on ice melt so that we may understand better the drivers behind melting patterns.

3.1.1 Purpose

The intended use of AEM3D for this project was to simulate the response of ice melt to changing bathymetry based on idealized lake conditions. In the simplest version of this analysis, inflows/outflows and sediment heating were excluded, leaving the atmospheric forcing as the only source of heating to the lake. This case also included a weak stratification, and omitted Coriolis, or wind-induced ice cover oscillations, whose influence would complicate the observed circulation pattern. Furthermore, there was no snow input to maintain spatially uniform

penetration of solar radiation to the ice cover. The resulting conditions are thus expected to capture the direct correlation between varying lake depths and ice thickness heterogeneity.

3.2 Methods

3.2.1 Model Set up

The physical set up of the simulation is meant to mimic a midsize ice-covered lake with 1.5 km width and 10 m maximum depth forced by idealized, but realistic, warming atmospheric conditions. The highest concentration of lakes are located at boreal and arctic latitudes and the highest abundance of lakes are small (0.002-0.01 km^2), but they represent a much lower percentage of non-glaciated land surfaces while medium and large lakes dominate the global areal extent of lakes (Verpoorter et al., 2014). With a surface area of ~2 km^2 for this idealized lake, it is corresponding to a medium scale lake. Melting of the ice cover begins right away in combination with warming of the water column from the depth-averaged initial water temperature of 0.5°C. The shape of the lake, a truncated cone, is kept intentionally simple to provide a basis for correlating its interaction with melting patterns before complexity can be introduced.

There were three inputs considered in the model set up: the meteorological forcing, an initial profile for the water temperature, and an initial uniform ice thickness. The forcing was designed to be moderate-mild to achieve melting results over a long enough time frame to allow for time-averaged analyses. In the simulations, the beginning of "spring" was set to be April 1st and run until all ice melted, which was approximately a month and a half of simulation time. Using Kingston, Ontario (44.2° N, 76.5° W), as the reference location for the lake, hourly shortwave radiation was downloaded from the NASA Langley Research Centre (LaRC)

Prediction of Worldwide Energy Resource (POWER) for 2018-2022. The (rounded) mean peak shortwave radiation for the 5-year dataset was approximately 600 W/m^2 with 14 hours of daylight for the month of April. These values were used in developing the idealized solar radiation input as a gaussian distribution centered around noon. It is noted that the hours of daylight were tuned to match a $\mu \pm 4\sigma$ (99.99%) width of the gaussian distribution, while the solar radiation observations in Kingston reported daylight according to a width closer to 2σ ($\sigma = 3$), meaning the quantity of solar radiation input to the model is lower than the observations (but the peak values are aligned). For air temperatures, a diurnal sinusoidal function with a range of 0-10°C was used under the assumption that these values could serve as mild but still reasonable spring conditions. The daily mean air temperatures reported by Environment and Climate Change Canada – Meteorological Service of Canada for Kingston in April were downloaded for 2018-2022, and the 5-year daily averages fluctuated between 0-10°C between the beginning to end of the month, which validated the reasonability of the range used in the model. Although peak air temperatures may occur later in the afternoon due to the delay of land surfaces warming, the idealized data peak was centered at noon to match the solar radiation for simplicity. Also operating on a daily cycle, the wind speed turned on at noon for 4 hours and then turned off again, with a magnitude of 5 m/s. However, this did not affect the hydrodynamics while the ice cover was present. Cloud cover remained at a constant fraction of 0.5. The water temperature initial condition was defined as a linear profile from 0°C at the surface to 1°C at the lake bottom. A linear profile provided a simple approach to represent a weakly stratified water column without defining a specific surface mixed layer depth. The 1°C bottom temperature was chosen according to a Cryomictic regime, as defined by Yang et al. (2021). We assumed an initial ice thickness of 0.35 m based upon preliminary numerical experiments under moderate freezing

conditions. The relevant parameters and forcings are illustrated in the schematic below (Figure 3-1).

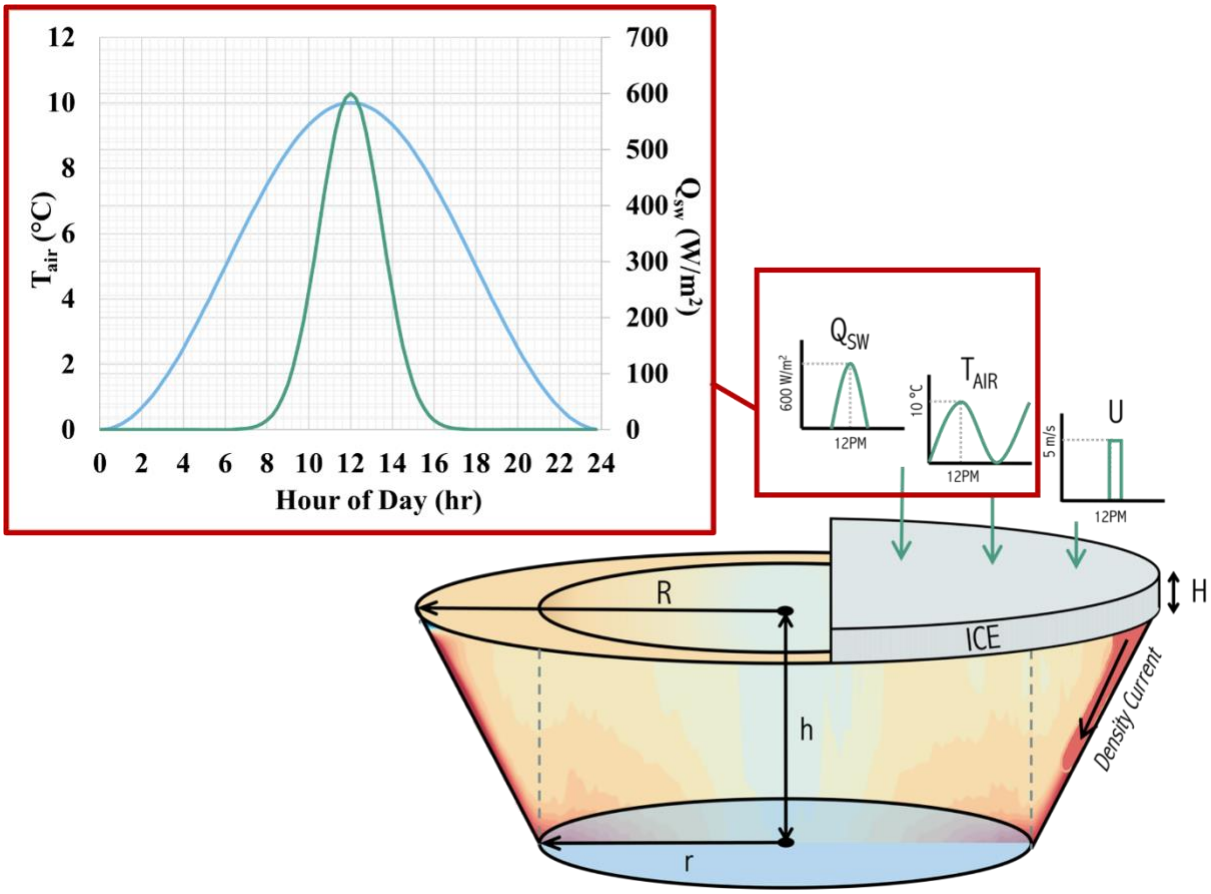

Figure 3-1. Schematic of key bathymetry variables and relevant meteorological input. Lake surface radius (R) and maximum depth (h) are constant at 750 m and 10 m, respectively, while bottom radius (r) changes between test cases. Solar radiation (Q_{SW}) is represented by a gaussian curve with mean (μ) centred at noon, standard deviations (σ) of 1.5 hours (chosen such that Q_{SW} > 0.01 W/m^2 for 14 hours), and amplitude of 600 W/m^2 at 12PM; Air temperature varies sinusoidally according to $T_{AIR} = 5\cos(2\pi(t-12)/24) + 5$ with a period of 12 hours and peak at 12PM; Wind speed is constant at 5 m/s for 4hrs each day, beginning at 12PM. Total ice thickness is defined by H.

3.2.2 Model Description

The idealized ice-covered lake was simulated using the three-dimensional hydrodynamic Aquatic Ecosystem Model (AEM3D), which is based on its well-recognized predecessor, the Estuary and Lake Computer Model (ELCOM), and offers coupling to the iWQ water quality model (Zamani et al. 2020; Hodges and Dallimore, 2022). The governing transport equations solved are the unsteady Reynolds-Averaged Navier Stokes (RANS), with the Boussinesq approximation and an assumption of hydrostatic pressure (Hodges and Dallimore, 2022). The model uses the UNESCO equation of state to calculate density based on temperature, pressure, and salinity, however this set up is simulating a freshwater lake, with salinity set to zero.

The ice algorithm in AEM3D is based on the model presented by Rogers et al. (1995) and was first coupled to ELCOM by Oveisy et al. (2012) to improve numerical simulations of winter processes through incorporating the effect of ice covers on lake hydrodynamics and biogeochemistry. The core theory behind the ice model is to use the modelled surface-layer thermodynamics and atmospheric fluxes to solve the steady-state heat conduction equation between three layers: blue ice, white ice, and snow (Oveisy et al. 2012). Given that the solution is resolved at each grid point, the model can capture spatial variability in the ice layer components based on heterogeneity in the lake surface layer (Caramatti et al. 2019). A limitation in this model is the neglection of the various physical processes that might break up and advect the ice cover (Oveisy et al. 2012).

For the model lake, a 6.25x6.25 m horizontal grid with 0.25 m uniformly spaced vertical layers was used, resulting in 240 horizontal and 40 vertical grid cells. A resolution test revealed that as the grid spacing reduced from 25 m to 6.25 m, or 25 cm to 10 cm vertically, there were no

significant changes to the large-scale physical processes. The finer grid did resolve more smaller-scale features, as was expected, but these were not necessary to observe the relationships between lake shape and ice melt. The chosen resolution reflected the best combination to adequately resolve all key features while maintaining a computational effort that suited the study (i.e., one case can be run overnight). The timestep of the simulation was 22.5 seconds, with output saved hourly, and this was sufficient to satisfy the Courant-Friedrichs-Lewy condition (Appendix B).

3.2.3 Simulation Cases

To study a bathymetric-induced change in the ice melt, a single bathymetric feature was chosen to modify between cases. The cases modelled a symmetrical truncated cone with constant surface radius (R) and maximum depth (h), as illustrated in Figure 3-1. Five variations of the side slope for this shape were created by gradually decreasing the bottom radius (r), as well as a reference cylinder and cone case with the lake bottom being either completely flat or sloping, respectively. Although side slope was the only bathymetric feature being modified, the mean depth and volume of each slope case differed accordingly as well.

Table 3-1: Ratio of bottom to top radius for slope number label

Slope Number	r/R
1	1
2	5/6
3	2/3
4	1/2
5	1/3
6	1/6
7	0

The AEM3D simulations for each slope case were analyzed based on the modelled output of blue ice depth, water temperature, and velocity. The intended analysis aimed to (1) identify the dominant flow feature driving the circulation and heat transport based on the hydrodynamics of the water column, (2) quantify the differential heating subjected to the ice cover and resulting melt pattern due to the identified under-ice flow structure, and (3) correlate the way in which the changes to bathymetry altered the heat transport.

3.2.4 Analysis Methods

The output variables were daily averaged to better distinguish the overall daily effect of the solar radiation and air temperature to the system. Additional variables discussed in characterizing the system were the ice melt rate and the advective heat flux. The melt rate ($M = -\frac{dH}{dt}$) was determined with the modelled ice depth (H) using a central difference method and single-sided differences at the beginning and end of the time-period. A positive melt rate was defined as a decrease in ice thickness. The advective heat flux ($Q_{adv,r}$) corresponds to the radial transport of heat within the lake and is calculated

$$Q_{adv,r} = \rho c_p T' \cdot u_r \tag{1}$$

using the temperature perturbation from the mean (T'),

$$T' = T - \overline{T} \tag{2}$$

The calculations performed in this chapter used a rz-slice through the domain centre, so temperature mean ($\overline{T}$) was computed at each depth as

$$\overline{T} = \frac{\pi \int T \cdot r dr}{\pi \int 1 \cdot r dr} \tag{3}$$

to account for the use of the centre slice. This was found to be representative of the radial average due to the lake's symmetry. Using T' rather than T in equation 1 ensured that temperature magnitudes (always >0) were not masked by velocity direction so that it is easier to distinguish if a negative heat flux is transporting warmer ($T' > 0$) or cooler water ($T' < 0$) relative to a positive heat flux.

The date that simulation results were snapshotted and compared was set as May 5th, despite the simulation being run for 2 months until the end of May. For each slope case, Figure *3-2* provides the minimum ice thickness (H_{min}), melt rate of H_{min} (dH/dt_{min}), and the mean temperature of the entire rz-slice (T_{avg}). The end date was selected according to the criteria of (1) before the minimum ice depth melts below 0.02 m, (2) melt rates approaching zero but prior to peaking from sudden melting and (3) before temperature of maximum density (T_{md}) is reached. Slope 7 has the smallest volume, so it is the first case to reach T_{md} and experience rapid ice melt, thus cutting off the results on May 5th allows for all cases to be properly captured.

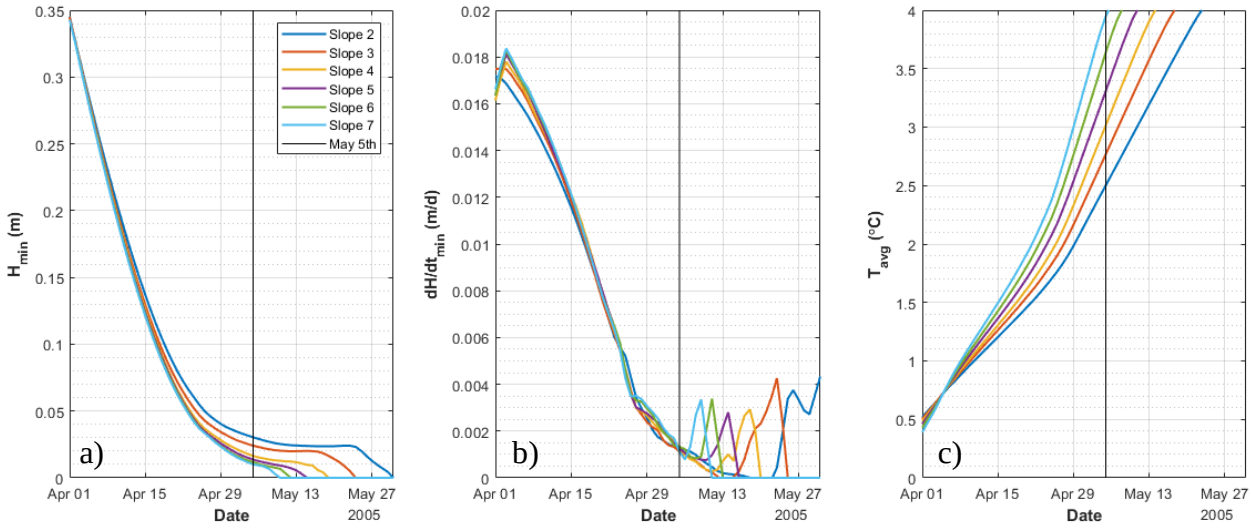

Figure 3-2. Timeseries of the (a) minimum ice thickness, (b) melt rate of minimum ice thickness, and (c) mean water temperature of centre slice for each slope case. The vertical black line denotes May 5th, which is comparison date in this study.

3.3 Results

3.3.1 Hydrodynamics

Without any inflows/outflows, sediment heating, or precipitation, the only source of heating to the lake is through sensible heating at the surface and penetrative solar radiation, and without snow cover to affect albedo or restrict light attenuation via white ice formation, solar radiation evenly penetrates the ice cover. The blue ice in the model has attenuation coefficients of 3.75 m^{-1} and 20 m^{-1} for visible and near infrared light, respectively, so most of the solar radiation can penetrate the 0.35 m ice cover. The surface layer and shallow depths will thus heat up first. As the water column begins entirely below the temperature of maximum density, this warming will drive convection. Except for the cylinder case, the modelled hydrodynamics have preferential warming of the shallower sloping regions, which results in warmer (denser) water

that flows downslope. These downwelling plumes drive a net recirculation within the lake, with a net radially outward flow near the surface ice.

We begin with a discussion of Slope 3 as a representative case, where we will highlight any significant differences between cases. The daily averaged temperature perturbation (the temperature difference from the horizontal mean, given by equation 2 and 3), radial velocity, and vertical velocity are plotted in Figure 3-3 on May 5th, the cut off date of the simulation. The temperature perturbation here is $\pm$0.15°C from the mean, but throughout the simulation the temperature of the entire lake slice is increasing from an average of 0.5°C to 2.7°C, for Slope 3 (Figure 3-2c). We see that the temperature perturbation is warmer along the sides of the lake than the centre with an associated negative inward radial velocity, consistent with the presence of a gravity current. The resulting circulation produces surface velocities that are radially outwards while beneath that, velocities are moving towards the centre of the lake. This velocity field indicates that as the gravity currents on both sides of the lake reach the bottom, they will be transported inwards and drive an upwelling current as they intersect, which in turn causes a net outward movement of water at the surface to replace the displaced fluid. The vertical velocities show convection plumes across the entire cross-section due to the surface layer warming, which will promote mixing and convection throughout the lake. Considering the results from temperature perturbation and velocity along the centre slice together, it is evident that the circulation cells driving heat upwards are more contained along the sides of the centre region (i.e., R = 200-500 m), while surrounding R = 0, mixing is dominated by vertical convection.

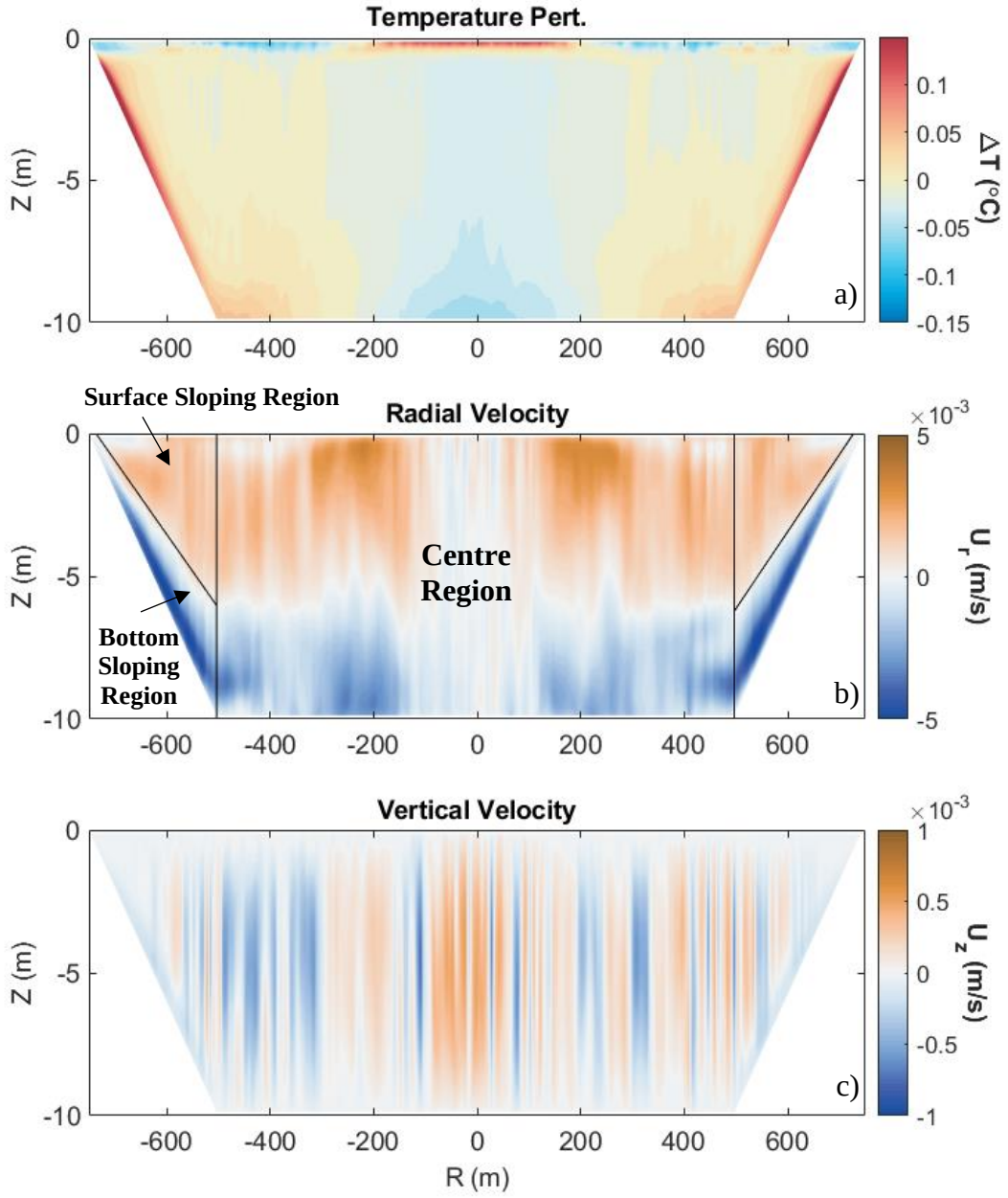

Figure 3-3. Hydrodynamics of Slope 3 in a daily-averaged snapshot of the cut off date of the simulation of May 5th: (a) temperature perturbation, (b) radial velocity with black lines denoting the boundaries to three key regions of the lake, and (c) vertical velocity

We observe three key regions in the lake: the centre, the sloping region surface layer, and sloping region bottom layer. We delineate the two sloping regions according to the median depth

where radial velocities are zero, shown by the black lines in Figure 3-3b. These regions represent the areas where heat is on average flowing from one to another, which ultimately dictates the resulting thermal structure underneath the ice layer contributing to melting. Figure *3-4* shows the average temperature of the sloping regions relative to the mean temperature of the centre. On average, the temperature in the bottom layer of the sloping region is warmer than the centre because the gravity currents are continuously forming. On the other hand, the temperature is colder near the surface of the sloping regions as the upwelling current pushes the cooler water originally in the centre to the sides of the lake. It is expected that the shallowest depths of a lake will warm first, but this model highlights that it is only the bottom layer of the shallow area that is experiencing accelerated warming. This is an important distinction because it is the surface water that will dictate the melting based on the temperature gradient to the ice, and cooler waters at the lake sides will result in milder gradients.

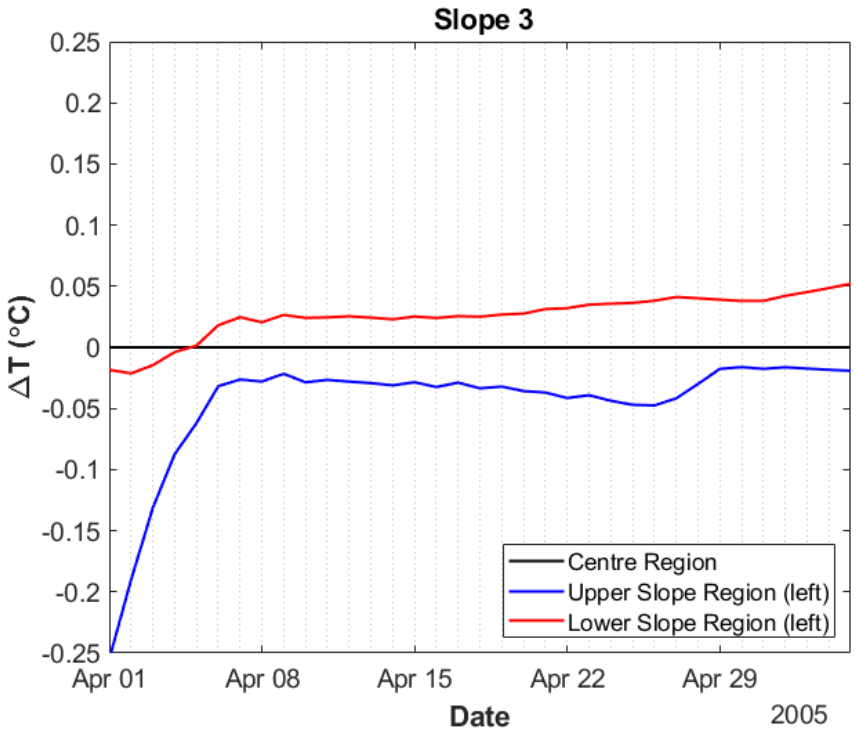

Figure 3-4. Average temperature in upper and lower layers of sloping region relative to the mean temperature of centre region (for Slope 3)

The movement of heat in the lake can be further quantified with the heat flux at the boundary where the three regions intersect (vertical line shown in Figure 3-3b), which is the radius where the sloping sides meet the flat bottom (Figure *3-5*). Given the symmetry in the lake, the circulation cells are mirrored on either side of the lake, which is expected to be reflected in the ice melt. The advective heat flux at the intersection point displays negative magnitudes at the bottom depths and surface layer, however, radial velocities are moving negatively inwards and positively outwards at each of those locations, respectively, indicating the transport of warmer water at the bottom and cooler water at the surface. In the middle depths, the heat flux is weaker but is indicating roughly three layers of movement: warmer water being transported to the sides

below the surface waters, cooler water moving outwards, and cooler water being transported inwards above the bottom waters.

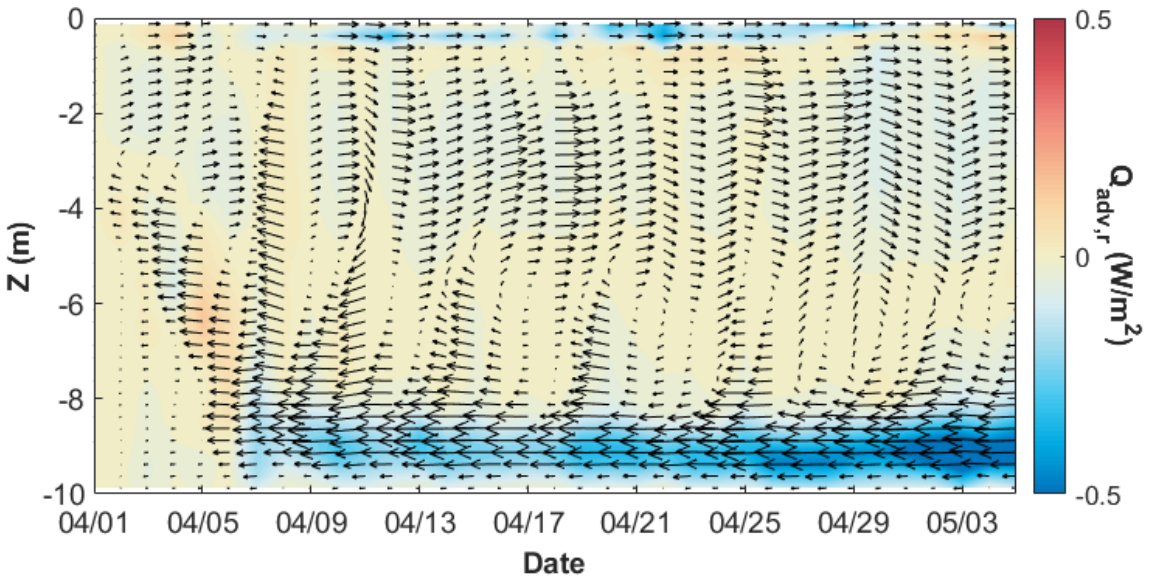

Figure 3-5. Vertical distribution of radial heat flux based on temperature perturbation in time at the location of intersection between sloping region and flat bottom (for Slope 3).

The conceptual model illustrates that heat is being transported from the sloping sides were the gravity currents first form to the centre of the lake, forcing the fluid there to be pushed upwards and this will in turn cause a compensating outwards (towards the lake edge) circulation near the surface. Since cooler water is being displaced outwards to the sides of the lake, this region is expected to be subjected to lower melting according to a milder temperature gradient between the surface layer water and ice temperature. The hydrodynamics presented here provide evidence for the simple organized circulation system that would occur under baseline input, and

it is clear how that system is moving heat around the water column to eventually lead to heterogeneity in the surface water temperatures.

3.3.2 Ice Melt

Heat flux to the bottom interface of the ice is modelled in AEM3D following Fourier's Heat Law:

$$Q_w = -K_w \frac{(T_w - T_f)}{\Delta z} \quad (4)$$

where the vertical distance is the thermal boundary layer specified by AEM3D as a default value of Δz =0.039 m, K_w is water conductivity, T_f is the freezing temperature, and T_w is the surface water temperature. Contribution of physical processes in the lake to melting of the ice cover is therefore calculated in AEM3D to be a function of surface water temperature alone. While velocity is not considered in the ice heat budget, it is important in identifying the regions with increased movement of heat to the surface. Areas with continuous heat convergence will result in higher melt rates compared to the areas where heat was observed to be moving away. This pattern is reflected in the melt rates shown in Figure *3-6*. There is evidence of distinct spatial variability to the melt pattern, with the fastest rates located in the centre where the hydrodynamics of the lake indicated heat was converging. The snapshot on May 5th suggests there is a small radius of higher melt rates, but this is likely an artifact of the periodicity of the upwelling currents, whereas for a time average of the last 10 days of the simulation, Figure *3-6*b indicates there is also a ring of higher melt rates at R ~ 500 m.

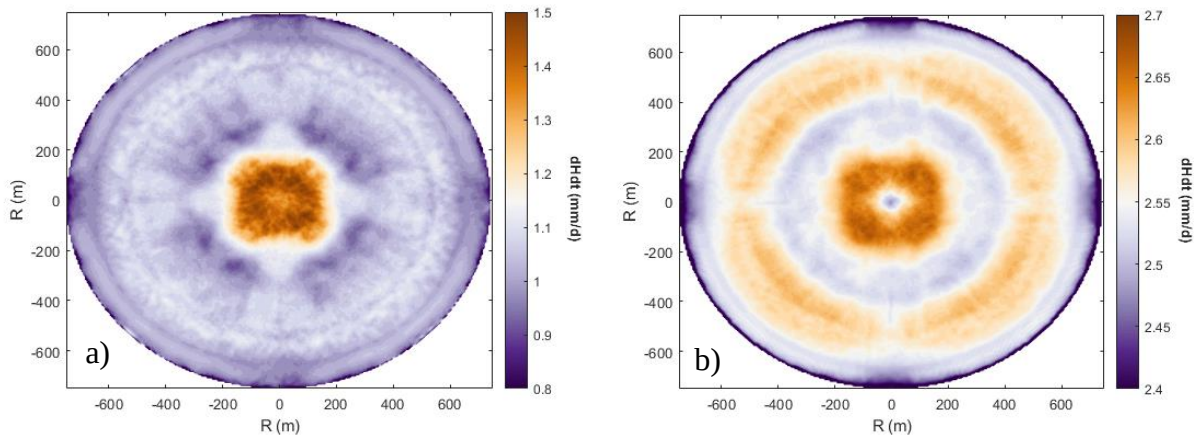

Figure 3-6. (a) Daily averaged melt rates on the simulation cut off date of May 5th, and (b) 10-day average of melt rates between Apr 25th-May 5th (for Slope 3)

The ice profile at the end of the simulation date shows a clear signature of bathymetry for each slope case (Figure *3-7*). The ice is consistently thinnest in the centre region and linearly increasing in depth towards the edges of the profile. It is clear bathymetry is driving the heterogeneous melting because that is the only factor changing between the slope cases.

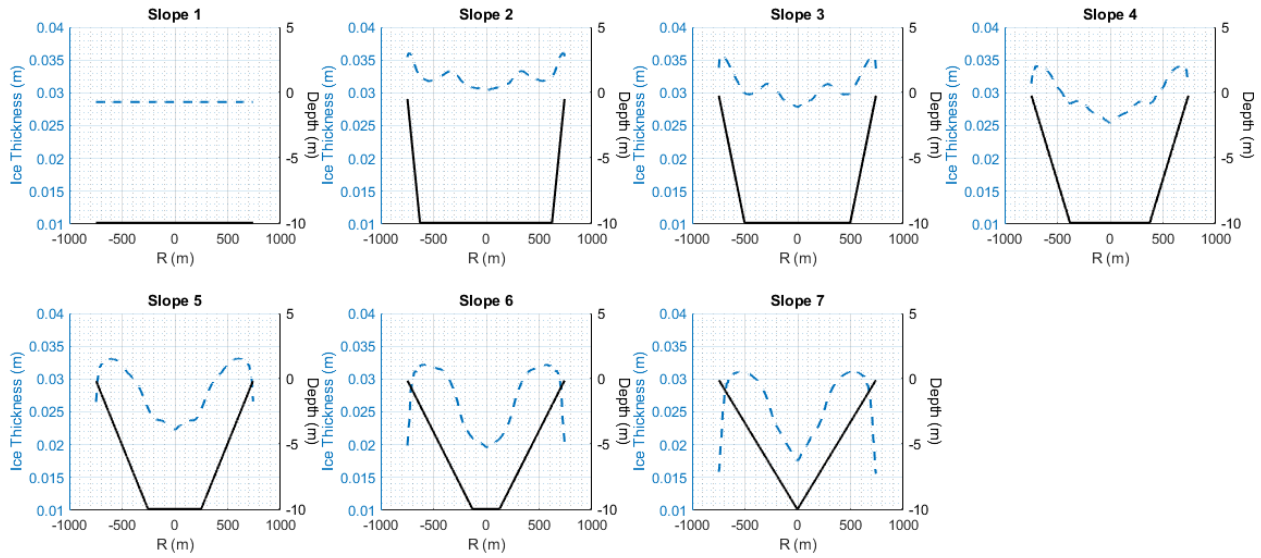

Figure 3-7. Ice depth profile along centreline of lake on May 5th for each slope case

This chapter has inferred the contribution of heat from the water column to ice melt based on the net ice thickness output, but the resulting ice shape is not only a product of melting at the bottom interface of the ice cover. In reality, ice depth will also decrease at the air-ice interface in response to thermodynamic fluxes from the atmosphere. If the total melt rate is broken down into its contribution from the surface and bottom, the surface melting is more significant in magnitude (Figure *3-8*).

At the start of the melting period, the surface melt rate is much higher than the bottom melt rate, but they begin to converge as time progresses. This suggests that under uniform meteorological input, the spatial variability in ice thickness may not be visible from the surface of the lake at the start of the melting period. However, as the ice thins and the relative significance of melting from the surface is reduced, the heterogeneity of the bottom interface may encourage preferential melting, which would intensify the variability observed at the surface.

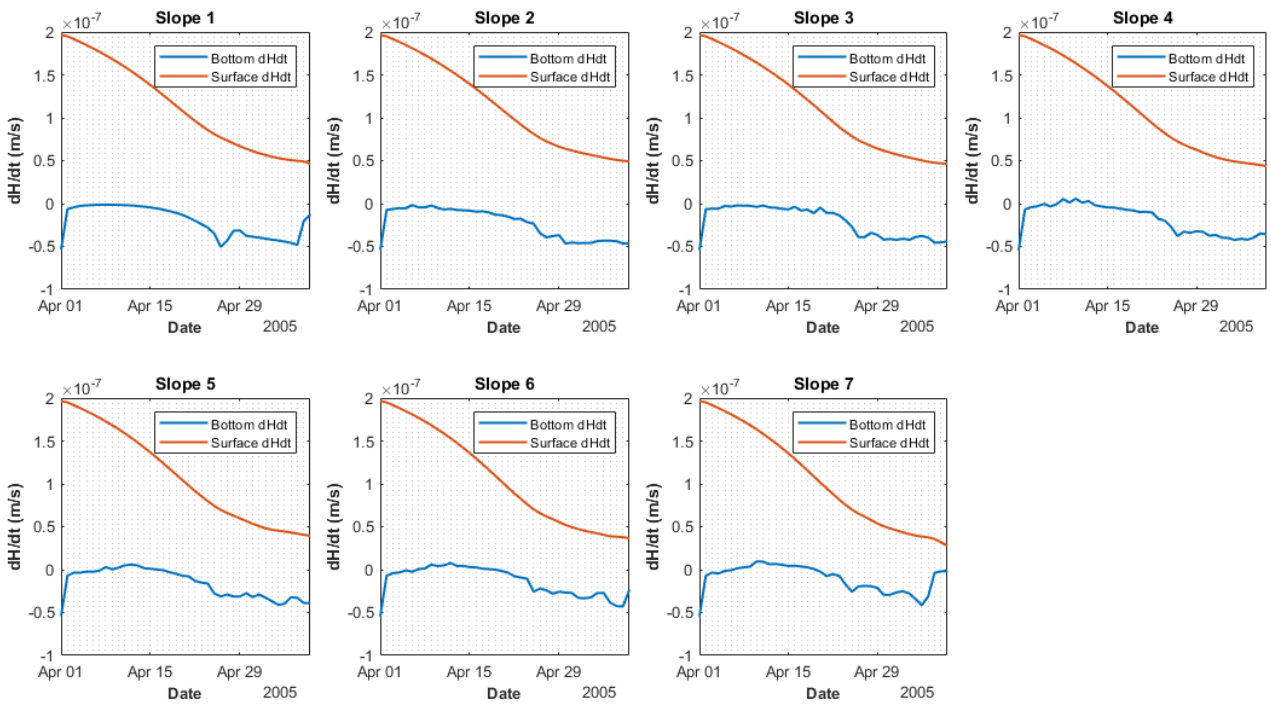

Figure 3-8. Melt rates calculated at the surface and bottom of ice cover for each slope case

3.4 Discussion

The modelled hydrodynamics of this setup, though idealized and simplified, are designed to model the convective stage of an ice-covered period, known as Winter II (Jansen et al. 2021; Kirillin et al. 2012). The nature of the under-ice circulation during this stage is characterized as being driven by penetrative solar radiation through an ice cover whose snow layer has presumably already melted (Jansen et al. 2021). There are two components to the convection induced: the convective mixed layer (CML) plumes and gravity currents (Bouffard and Wüest, 2019; Forrest et al. 2008).

Warming of the littoral regions and subsequent generation of density currents in spring has been previously observed in field and numerical studies of ice-covered lakes (Cortés and

MacIntyre, 2020; Forrest et al. 2008; Kirillin et al. 2015; Ulloa et al. 2019; Salonen et al. 2014). There is a consensus in many studied lakes on the presence of lateral temperature gradients regardless of if they stem from radiatively driven convection (RDC), inflow intrusions, meltwater runoff, or sediment heating. Thus, while the source of the differential heating may vary, the resulting basal heat distribution in the lake remains the same irrespective of other lake-specific flow features also contributing to under-ice currents. This thesis successfully identified the dominant flow feature modelled by AEM3D to be shallow water warming initiating gravity currents that transport heat to the lake interior in addition to convection plumes across all lake depths. This result frames a simplified underlying circulation system that coheres with previous work on ice-covered lakes.

The contribution of external radiative forcing to surface layer warming has previously been found to be more significant than under-ice horizontal fluxes (Ulloa et al. 2019; Ramón et al. 2021). The effect of strong radiative flux to surface ice melt can also be emphasized by spatial variability in snow fall, snow drift, and the resulting transparency of the ice type (Bengtsson, 1986; Forrest et al. 2008; Kirillin and Leppäranta, 2022; Solarski and Rzetala, 2022). Similar to those findings, the results from these simulations indicate that warming at the ice surface due to atmospheric forcing is more significant in magnitude than the under-ice warming. However, with spatially uniform surface melting, the precise effect of the under-ice thermal structure on the heterogeneity of ice depth can be analysed in isolation and the results indicate a strong interdependency. Previous field studies are unable to separate the variable precipitation input, while the 2D and 3D numerical studies performed by Ulloa et al. (2019) and Ramón et al. (2021), respectively, on the lake circulation driven convective mixed layer (CML) warming and deepening do not comment on the heterogeneity of ice depth that would occur in response. With

this idealized 3D numerical setup, a systematic breakdown of how fundamental mixing processes can induce differential heating to the bottom interface of the ice cover is shown, while this correlation is often hidden behind layers of complexity in real lakes. The modelled convection demonstrates that with the continuous recycling of bottom waters to the surface at the centre of the lake, the deepest regions experience accelerated melting relative to the shallower areas, and this is reflected in the blue ice melt pattern. It is intuitive to expect the littoral regions to melt first, giving they are warming up first, but AEM3D models the opposite case except right in the corner. This may be a result of the ambiguous littoral zones in the idealized bathymetry, or an artifact of the model's inability to capture broken ice.

The varying slope cases illustrate plainly that ice thickness mimics the shape of the bathymetry under base conditions, but conceptually the bottom melting must be dependent on the surface-layer temperature only. The temperature heterogeneity under the ice therefore must be a direct artifact of the bathymetry-driven circulation. It is shown that the large-scale flow features remain present as side slope changes, with melting concentrated in the centre and linearly decreasing towards the lake edges. However, each adjustment to the slope alters the relative volume of interior and shallow sloping waters, which will influence the rate of warming, the speed of the gravity current, and size of the upwelling current. Those bathymetric-induced changes will be reflected at the surface with thinner ice depth spanning the size of the lake centre as the side slope progresses from vertical to mild. It can be confirmed that bathymetry does play a role in ice melt, and it is expected that its effect will matter even as the circulation patterns change with additional features.

3.5 Limitations

The constraints of this analysis include the assumptions made to develop the simulations, the limitations of AEM3D, and the application of the results. For the base case to achieve its purpose, it only required enough details to observe a connection between bathymetry, convection, and ice melt, with all other parameters that might introduce, or influence currents considered ancillary. Thus, conditions such as precipitation, sediment heating, strong stratification, Coriolis force, ice cover oscillations, and inflows/outflows were omitted. In reality, these conditions are not ancillary but can be significant features for many lakes similar in size and latitude to the hypothetical one. While the assumptions might prevent the direct comparison of these results to a real lake, it is expected that sediment heating, strong stratification, and inflows would not fundamentally change the hydrodynamics of downslope gravity currents and surface layer convection, which are observed flow features under ice (Cortés and MacIntyre, 2020; Forrest et al. 2008; Kirillin et al. 2015; Ulloa et al. 2019; Salonen et al. 2014). Sediment heating is considered a limitation to the model as well due to its current inability to be included. The effect of a snow cover is significant in many studies of ice melt, but less so for the ice-covered period dictated by RDC, which is represented here. For a 1.5 km lake with lateral velocity scales on the order of 10^{-3} m/s, Coriolis is expected to have a strong influence on currents. The purpose of neglecting Coriolis in this chapter, despite scaling suggesting it will be important, was to first understand the background flow features driven by convection alone. The results from the base case may not physically accurate in representing most ice-covered lakes effected by Coriolis, but the information is still useful in setting up the foundation for a modelling study. Though this is a notable limitation of the results presented in this chapter, the next chapter aims to delve deeper on the effect of Coriolis on the system. Symmetrical

bathymetry is another assumption not likely to be reflected in real lakes. It is possible that some characteristics of the upwelling current are a by-product of the mirrored gravity currents intersecting, however, the overall results are not expected to change significantly. As long as the warming shallow waters are denser than surrounding fluid, the plumes will be pulled downwards by gravity until they restabilize at deeper depths, and this will provide a consistent upward displacement of water at these depths to account for the new fluid accumulating underneath.

Using AEM3D in this context highlighted two specific modelling limitations. The first is that to maintain a reasonable computation efficiency, the model was run in hydrostatic mode. The governing equations thus simplify the vertical momentum equation according to a hydrostatic pressure assumption, resulting in vertical velocities calculated based on continuity with the horizontal velocities. Nonhydrostatic models are most important for resolving details at fine grid resolutions, such as internal waves and convection processes (Parsapour-Moghaddam and Rennie, 2017). By considering nonhydrostatic pressure negligible, there is potential for error in the vertical velocity magnitudes and convection cells sizing. However, the vertical velocities produced by the model are an order of magnitude smaller than lateral velocities, and the density gradients are relatively weak for the observed minor temperature perturbations. Furthermore, the goal of this analysis was principally concerned with the large-scale flow features while finer-scale details were considered out of scope. Ghane (2022) utilized AEM3D in hydrostatic mode to model turnover events in a small temperate lake, and a nonhydrostatic test revealed that the quantitative differences between the two runs were small enough to not significantly impact the overall temperature structure in the lake, so the hydrostatic simplification was deemed a reasonable compromise for the large computational effort of nonhydrostatic mode. The second limitation of AEM3D was its lack of feedback between the shape of the ice as it melts and the

hydrodynamics. Since the ice model only references surface temperature, other processes that could amplify the signal shown in this chapter are not considered.

Given that the modeling approach uses idealized bathymetry and input, the model cannot be validated with collected data. After the addition of the ice algorithm to ELCOM, the ice model was successfully validated with Lake Ontario and Harmon Lake data (Oveisy et al. 2012). While AEM3D is the updated and improved successor of ELCOM, it was not validated separately, so an ice budget analysis was performed using the AEM3D output and the equations described in Oveisy et al. (2012). The ice budget was successfully closed, and the calculated and modelled values agreed (Appendix A). Furthermore, both AEM3D and ELCOM have previously been validated successfully in recent hydrodynamic studies, increasing confidence and reliability of these models for application to this work (Oveisy et al., 2012; Ghane and Boegman, 2021; Zhao et al., 2021; Caramatti et al., 2019; Zamani et al., 2020). Another limitation of the results is the small perturbation in ice thicknesses spatially in combination with the surface melting being responsible for majority of the total ice melt. The melt pattern discussed here might perhaps not be visible from the surface of the lake, but even a minor contribution from the water to ice thinning could lead to preferentially melting in those areas. It is reasonable to expect interannual variability in the winter meteorological conditions and ice composition, suggesting inconsistency in the melt pattern year-to-year might occur. However, for lakes that see a repeating pattern of thinnest ice in the same region, these results can support the possibility of bathymetry playing a role in those cases.

3.6 Conclusion

This chapter successfully simulated differential melting of ice covers and under-ice heat transport. Both of these processes have been observed in other field and numerical studies, but the effect of basin scale circulation on ice melts has not been previously discussed with this type of setup. It is still not well understood how intrinsic properties of lakes, such as its shape, might be intertwined with the physical processes and ice melt observations. It can be difficult to pinpoint the source of variability in melt patterns because many parameters cannot be fixed, and the effect of individual lake or external characteristics cannot be easily isolated. However, the simplistic nature of these simulations allows for such an isolation, and the result is clear: bathymetry does play a role in influencing circulation and mixing. It has been shown that without other features masking its effect, there is a direct relationship between bathymetry and ice melt. Even if the relative contribution of heat from the water column is less than the air, the specific way in which the under-ice flow structure could contribute to ice thickness heterogeneity is valuable information. In a real lake, observations of variable ice thickness over a single winter will be dominated by atmospheric conditions and ice quality/composition, given its significance to the ice heat balance. However, atmospheric conditions experience interannual variability unlike the unchanging nature of bathymetry, so a repeating effect or characteristic in the melt pattern over multiple years might suggest contribution from bathymetry-driven circulation. While the assumptions made for the numerical analysis may be limiting, the largest benefit is learning that even a relatively small effect to the ice melt from under-ice mixing will have a signature of bathymetry. There is opportunity to build upon this work by considering how additional features that modify the under-ice circulation might enhance or diminish the role

bathymetry plays. Another opportunity to extend this study should involve measuring lakes with significant side slopes to validate whether differential melting is observed.

3.7 References

Bengtsson, L. (1986). Spatial Variability of Lake Ice Covers. *Geografiska Annaler: Series A, Physical Geography*, 68:1-2, 113-121. https://doi.org/10.1080/04353676.1986.11880164

Bouffard, D., & Wüest, A. (2019). Convection in Lakes. *Annual Review of Fluid Mechanics*, 51(1), 189–215. https://doi.org/10.1146/annurev-fluid-010518-040506

Caramatti, I., Peeters, F., Hamilton, D., & Hofmann, H. (2019). Modelling inter-annual and spatial variability of ice cover in a temperate lake with complex morphology. *Hydrological Processes*, 34, 691-704, doi: 10.1002/hyp.13618

Cortés, A., & MacIntyre, S. (2020). Mixing processes in small arctic lakes during spring. *Limnology and Oceanography*, 65(2), 260–288. https://doi.org/10.1002/lno.11296

Farmer, D. M. (1975). Penetrative convection in the absence of mean shear. *Quarterly Journal of the Royal Meteorological Society*, *101*(430), 869–891. https://doi.org/10.1002/qj.49710143011

Forrest, A. L., Laval, B. E., Pieters, R., & Lim, D. S. S. (2008). Convectively driven transport in temperate lakes. *Limnology and Oceanography*, 53(5part2), 2321–2332. https://doi.org/10.4319/lo.2008.53.5_part_2.2321

Ghane, A. (2022). Phosphorus and Oxygen Dynamics Between Fall and Spring Turnover Events in a Small Canadian Shield Lake. Ph.D thesis. Queen's University.

Ghane, A., & Boegman, L. (2021). Turnover in a small Canadian shield lake. *Limnology and Oceanography*, 66(9), 3356–3373. https://doi.org/10.1002/lno.11884

Hodges, B., & Dallimore, C. (2022). Aquatic Ecosystem Model: AEM3D, Hydrodynamics Science Manual. Hydronumerics: Docklands, Australia

Jansen, J., MacIntyre, S., Barrett, D. C., Chin, Y.-P., Cortés, A., Forrest, A. L., et al. (2021). Winter limnology: How do hydrodynamics and biogeochemistry shape ecosystems under ice? *Journal of Geophysical Research: Biogeosciences*, 126, e2020JG006237. https://doi.org/10.1029/2020JG006237

Kirillin, G. & Leppäranta, M. (2022). Lake Ice Formation and Melt. Under-Ice Dynamics. *Encyclopedia of Inland Waters, 2nd Edition*. https://doi.org/10.1016/B978-0-12-819166-8.00003-7

Kirillin, G. B., Forrest, A. L., Graves, K. E., Fischer, A., Engelhardt, C., & Laval, B.E. (2015). Axisymmetric circulation driven by marginal heating in ice-covered lakes. *Geophysical Research Letters*, 42, 2893–2900. https://doi.org/10.1002/2014GL062180.

Kirillin, G., Leppäranta, M., Terzhevik, A., Granin, N., Bernhardt, J., Engelhardt, C., Efremova, T., Golosov, S., Palshin, N., Sherstyankin, P., Zdorovennova, G., & Zdorovennov, R. (2012). Physics of seasonally ice-covered lakes: A review. *Aquatic Sciences*, 74(4), 659–682. https://doi.org/10.1007/s00027-012-0279-y

Knoll, L. B., Sharma, S., Denfeld, B. A., Flaim, G., Hori, Y., Magnuson, J. J., Straile, D., & Weyhenmeyer, G. A. (2019). Consequences of lake and river ice loss on cultural ecosystem services. *Limnology and Oceanography Letters*, *4*(5), 119–131. https://doi.org/10.1002/lol2.10116

Kouraev, A. V., Zakharova, E. A., Rémy, F., Kostianoy, A. G., Shimaraev, M. N., Hall, N. M. J., & Ya. Suknev, A. (2016). Giant ice rings on lakes B aikal and H ovsgol: Inventory, associated water structure and potential formation mechanism. *Limnology and Oceanography*, *61*(3), 1001–1014. https://doi.org/10.1002/lno.10268

Matthews, P. C., & Heaney, S. I. (1987). Solar heating and its influence on mixing in ice-covered lakes. *Freshwater Biology*, *18*(1), 135–149. https://doi.org/10.1111/j.1365-2427.1987.tb01302.x

Mironov, D., Terzhevik, A., Kirillin, G., Jonas, T., Malm, J., & Farmer, D. (2002). Radiatively driven convection in ice-covered lakes: Observations, scaling, and a mixed layer model. *Journal of Geophysical Research: Oceans*, *107*(C4). https://doi.org/10.1029/2001JC000892

Oveisy, A., Boegman, L., & Imberger, J. (2012). Three-dimensional simulation of lake and ice dynamics during winter. *Limnology and Oceanography*, 57(1), 43-57, doi:10.4319/lo.2012.57.1.0043

Parsapour-Moghaddam, P., & Rennie, C. D. (2017). Hydrostatic versus nonhydrostatic hydrodynamic modelling of secondary flow in a tortuously meandering river: Application of Delft3D. *River Research and Applications*, 33(9), 1400–1410. https://doi.org/10.1002/rra.3214

Ramón, C. L., Ulloa, H. N., Doda, T., Winters, K. B., & Bouffard, D. (2021). Bathymetry and latitude modify lake warming under ice. *Hydrology and Earth System Sciences*, 25(4), 1813–1825. https://doi.org/10.5194/hess-25-1813-2021

Rogers, C. K., Lawrence, G.A., & Hamblin, P.F. (1995). Observations and numerical simulation of a shallow ice-covered midlatitude lake. *Limnology and Oceanography*, 40(2), 374-385, doi:10.4319/lo.1995.40.2.0374

Salonen, K., Pulkkanen, M., Salmi, P., & Griffiths, R. W. (2014). Interannual variability of circulation under spring ice in a boreal lake. *Limnology and Oceanography*, 59(6), 2121–2132. https://doi.org/10.4319/lo.2014.59.6.2121

Sharma, S., Blagrave, K., Magnuson, J. J., O'Reilly, C. M., Oliver, S., Batt, R. D., Magee, M. R., Straile, D., Weyhenmeyer, G. A., Winslow, L., & Woolway, R. I. (2019). Widespread loss

of lake ice around the Northern Hemisphere in a warming world. *Nature Climate Change, 9*(3), 227–231. https://doi.org/10.1038/s41558-018-0393-5

Solarski, M. & Rzetala, M. (2022). Determinants of Spatial Variability of Ice Thickness in Lakes in High Mountains of the Temperate Zone—The Case of the Tatra Mountains. *Water*, 14, 2360. https://doi.org/10.3390/w14152360

Ulloa, H. N., Winters, K. B., Wüest, A., & Bouffard, D. (2019). Differential Heating Drives Downslope Flows that Accelerate Mixed-Layer Warming in Ice-Covered Waters. *Geophysical Research Letters*, 46(23), 13872–13882. https://doi.org/10.1029/2019GL085258

Woodcock, A.H. (1965). Melt patterns in ice over shallow waters. *Limnology and Oceanography*, 10, R290-R297. https://doi.org/10.4319/lo.1965.10.suppl2.r290

Yang, B., Wells, M. G., McMeans, B. C., Dugan, H. A., Rusak, J. A., Weyhenmeyer, G. A., Brentrup, J. A., Hrycik, A. R., Laas, A., Pilla, R. M., Austin, J. A., Blanchfield, P. J., Carey, C. C., Guzzo, M. M., Lottig, N. R., MacKay, M. D., Middel, T. A., Pierson, D. C., Wang, J., & Young, J. D. (2021). A New Thermal Categorization of Ice-Covered Lakes. *Geophysical Research Letters*, *48*(3). https://doi.org/10.1029/2020GL091374

Yang, B., Young, J., Brown, L., & Wells, M. (2017). High-frequency observations of temperature and dissolved oxygen reveal under-ice convection in a large lake. *Geophysical Research Letters*, 44, 12, 218–12,226. https://doi.org/10.1002/2017GL075373

Verpoorter, C., Kutser, T., Seekell, D. A., & Tranvik, L. J. (2014). A global inventory of lakes based on high-resolution satellite imagery. *Geophysical Research Letters*, *41*(18), 6396–6402. https://doi.org/10.1002/2014GL060641

Zamani, B., Koch, M., & Hodges, B. R. (2020). Effects of morphology in controlling propagation of density currents in a reservoir using uncalibrated three-dimensional hydrodynamic modeling: Effects of morphology in propagation of density currents. *Journal of Limnology*, 79(3). https://doi.org/10.4081/jlimnol.2020.1942

Zhao, J., Valipour, R., León, L. F., & Rao, Y. R. (2021). High-resolution hydrodynamic modelling to study year-round circulations and inter-basin exchanges in Lake Winnipeg. *Journal of Great Lakes Research*, 47(3), 798–811. https://doi.org/10.1016/j.jglr.2020.12.004

Chapter 4 :

Effect of Coriolis on an Idealized Ice-Covered Lake

4.1 Introduction

Lake hydrodynamics in winter are categorized into two stages: Winter I where the release of sediment-stored heat generates downslope gravity currents, and Winter II where solar radiation can penetrate the ice cover to drive vertical convection (Kirillin et al. 2012). Penetrative solar radiation is often associated with circulation and deepening of a surface mixed layer through radiatively driven convection (RDC) (Farmer, 1975; Mironov et al., 2002). However, this process has also been observed to generate gravity currents that can travel offshore, similar to those produced by sediment heating as a result of littoral region warming (Jansen et al., 2021). Horizontal convection and lateral flows may develop from snowmelt water runoff (Kirillin et al. 2015; Cortés and MacIntyre, 2020), river inflow (Salonen et al., 2014), or differential warming of shallow areas (Ulloa et al., 2019; Forrest et al., 2008).

For ice-covered lakes, the time scales of these density-driven flows are much slower compared to the ice-free season, rendering the likelihood of current deflection by Coriolis much more significant (Kirillin et al., 2015). The Rossby radius of deformation provides a length scale for characterizing the relative importance of the Earth's rotation on horizontal flows whereby lakes larger than the Rossby radius will experience rotational effects (Kirillin et al., 2012). A dimensionless measure of rotation effects can also be used with the Rossby Number (Ro), which divides the Rossby radius by the characteristic horizontal length scale of a lake. Furthermore, Coriolis force in the winter is expected to have more significance than the summer due to slower velocities (Jansen et al., 2021). The circulation response driven by Coriolis has been observed in

previous work to produce under-ice gyres that play an important role in heat transfer (Forrest et al., 2013, Rizk et al., 2014, Kirillin et al., 2015, Huttula et al., 2010). Many lakes are located within latitudes of 40°-80°, where lakes are both more inclined towards developing ice covers as well as being influenced by Coriolis force, depending on size (Kirillin et al., 2012). Thus, these rotational flows discussed in other studies are likely an important component to the fundamental circulation system of most ice-covered lakes (Rizk et al. 2014). However, understanding of the influence of rotation on heat transport still remains limited (Ramon et al., 2021).

In a numerical study by Ramon et al. (2021), the authors show that varying Coriolis importance, parameterized by the Rossby number (Ro), sets up unique circulation responses to horizontal convection. Building off the 2D mixed-layer heat balance by Ulloa et al. (2019), the 3D model presented by Ramon et al. (2021) estimates the contribution of advected heat to the lake interior for the different Ro simulations, and their results yielded that as rotation increased, vertical and radial heat transfer became suppressed. The relevance of Coriolis to under-ice warming regimes is clear, particularly how the transition between ageostrophic and geostrophic balances can alter the velocity and temperature patterns (Ramon et al., 2021). The relationship between this transition of increasing rotational effect and resulting ice melting patterns, however, has not been discussed.

4.1.1 Purpose

The previous chapter highlighted how bathymetries with differing surface/bottom radius ratios will influence the magnitude and size of the upwelling current bringing heat to the surface layer of the lake centre, and these differences were reflected in the associated heterogeneous ice profile. It is expected based on the previous observations on this topic that the addition of

Coriolis to the model will have an effect to the lateral heat transport, but this chapter aims to also comment on changes to the ice cover shape. The transition from zero rotation to stronger rotation will be studied according to the simulated hydrodynamics to systematically understand how the progression in mixing systems occurs and to assess how the influence of bathymetry may be exaggerated or suppressed by Coriolis.

4.2 Methods

4.2.1 Model Description

The simulations are performed by the three-dimensional hydrodynamic Aquatic Ecosystem Model (AEM3D), which is updated from its well-recognized predecessor, the Estuary and Lake Computer Model (ELCOM). The governing transport equations solved are the unsteady Reynolds-Averaged Navier Stokes (RANS), with the Boussinesq approximation and an assumption of hydrostatic pressure (Hodges and Dallimore, 2022). The model uses the UNESCO equation of state to calculate density based on temperature, pressure, and salinity, however this set up is simulating a freshwater lake, so salinity is zero.

The ice algorithm in AEM3D is based on the model coupled to ELCOM by Oveisy et al. (2012) to improve numerical simulations of winter processes through incorporating the effect of ice covers on lake hydrodynamics and biogeochemistry. The ice model uses the modelled surface-layer thermodynamics and atmospheric fluxes to solve the steady-state heat conduction equation between three layers: blue ice, white ice, and snow (Oveisy et al. 2012; Rogers et al., 1995). The solution is resolved at each grid point, allowing the model to capture spatial variability in the ice layer components based on heterogeneity in the surface water temperatures

(Caramatti et al. 2019). A limitation in this model is the neglection of the various physical processes that might break up and advect the ice cover (Oveisy et al. 2012).

4.2.2 Model Setup

The physical set up of the modelled lake described in Chapter 3 is kept consistent here as a truncated cone shaped bathymetry with a 1.5 km width (2R) and 10 m maximum depth (h), shown in Figure *4-1*. Based on the resolution tests performed for Chapter 3, discussed in Appendix B, horizontal and vertical grid spacing of 6.25 m and 0.25 m, respectively, were chosen to balance the desired computational efficiency with sufficient resolution of the key large-scale physical processes. The same timestep of 22.5 s was used because it was found to satisfy the Courant-Friedrichs-Lewy condition due to the relatively small under-ice velocities in the base cases, and the velocities observed in this Chapter remain similarly small.

The inputs to the model remained the same to represent moderate-mild melting conditions for a weakly stratified water column. The meteorological forcing consisted of air temperature, solar radiation, and wind speed operating on a daily cycle with values peaking at noon. Air temperatures varied sinusoidally between 0-10°C, while solar radiation followed a gaussian distribution centred over noon at a maximum value of 600 W/m^2 and 14 hours of sunlight. The wind speed, although not expected to contribute to mixing of water below the ice cover, was left as an input that turned on at noon for 4 hours and then turned off again, with a magnitude of 5 m/s. Cloud cover remained at a constant fraction of 0.5. All other meteorological input was omitted or kept constant at their default value. A weakly stratified water column was represented by an initial linear water temperature profile of 0°C at the surface to 1°C at the lake bottom. The 1°C bottom temperature was chosen according to a Cryomictic regime, as defined

by Yang et al. (2021). Finally, a fixed initial uniform ice thickness was set at a magnitude of 0.35 m. Preliminary model runs with a 2-month freezing period predicted approximately 0.35 cm of ice under a range of conditions, therefore this was set as the initial value for the melting scenarios considered here. The problem setup along with the relevant meteorological forcing are illustrated in Figure *4-1*.

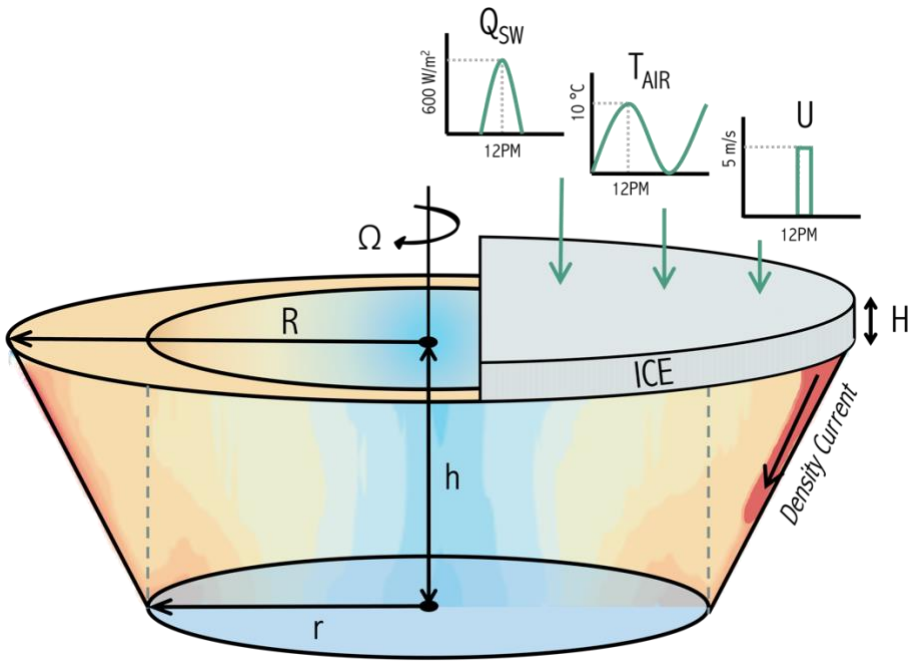

Figure 4-1. Schematic of key bathymetry variables and relevant meteorological input. Lake surface radius (R) and maximum depth (h) are constant at 750 m and 10 m, respectively, while bottom radius (r) changes between test cases. Solar radiation (Q_{SW}) is represented by a gaussian curve with mean (μ) centred at noon, standard deviations (σ) of 1.5 hours (chosen such that Q_{SW} > 0.01 W/m^2 for 14 hours), and amplitude of 600 W/m^2 at 12PM; Air temperature varies sinusoidally according to $T_{AIR} = 5\,cos(2\pi(t-12)/24) + 5$ with a period of 12 hours and peak at 12PM; Wind speed is constant at 5 m/s for 4hrs each day, beginning at 12PM. Total ice thickness is defined by H.

4.2.3 Simulation Cases

In this chapter, we considered simulation cases with different bathymetries that are consistent with those considered in the previous simulations in the absence of Coriolis. The results of the last chapter suggested that the same large-scale circulation pattern was present regardless of the side slope, therefore the number of slope variations analysed here was reduced to two cases. The chosen cases, summarized in Table *4-1*, have bathymetries that are neither the steepest or mildest slopes, with roughly 55% and 88% sloping surface area relative to the total lake surface area. This allows us to observe cases with different bottom bathymetry to comment on any changes to the ice melt response from Coriolis.

Table 4-1: Ratio of bottom to top radius for slope number label, and latitudes run for both cases

Slope Number	r/R	Latitudes Run
3	2/3	0°, 15°, 20°, 30°, 45°
5	1/3	0°, 15°, 20°, 30°, 45°

The interaction between bathymetry and ice melting was established in Chapter 3, but to properly understand how Coriolis' effect will change this interaction, it needs to first be investigated how the circulation in the lake transitions from a system with zero rotation to one with strong rotational forcing. The relative importance of rotation on the system can be characterized by a Rossby number (Ro), which defines a dimensionless ratio of the fluid's inertia to Coriolis force given by

$$R_o = \frac{U}{fL}, \tag{1}$$

where U and L are characteristic velocity and length scales, respectively, and f is the inertial frequency dependent on latitude. In this system, the most relevant timescale was the one

associated with the gravity current reaching the lake centre, thus the scales used were the peak radial velocity and surface radius. The characteristic radial velocity was defined as the median value of the maximum daily and azimuthally averaged radial velocity. Chapter 3 highlighted the results from Slope 3 because the overall circulation system was the same between bathymetries, and Figure *4-2* below also demonstrates the minor differences to the velocity magnitudes (using maximum surface velocity as an example) in the base cases.

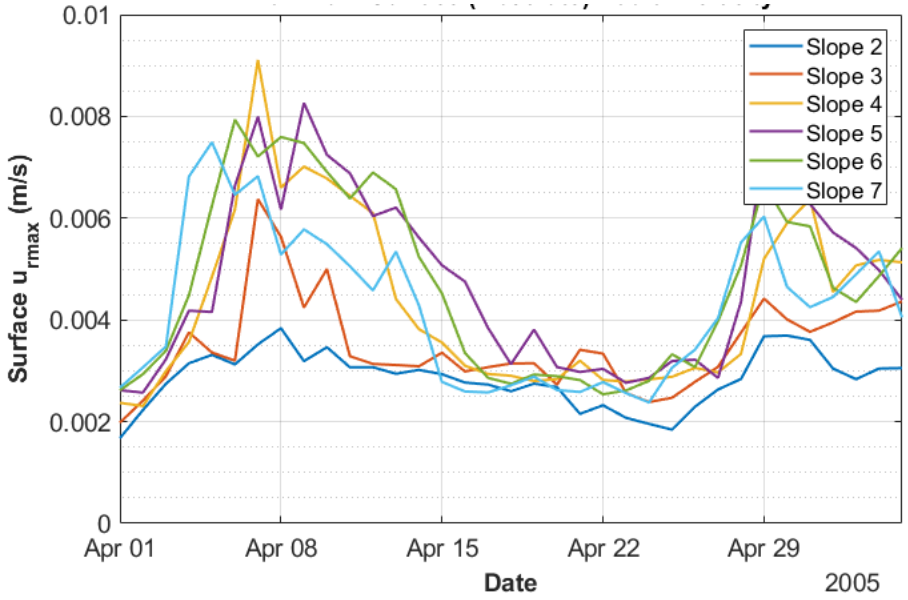

Figure 4-2. Maximum (absolute) surface radial velocity for all slope cases, from the base case simulations.

Therefore, the more appropriate variables to tune to modulate Ro for this Chapter was reasoned to be lake radius and latitude, which is used to calculate f. Between those options, latitude was found to provide more flexibility in maintaining resolution and computer run time compared to changing lake sizes.

There were five latitude iterations run for each slope case: 0° (i.e., no Coriolis force), 15°, 20°, 30°, and 45°. Except for the 0° case, the corresponding Ro values were all less than 1, verifying Coriolis' importance (see Figure *4-3*).

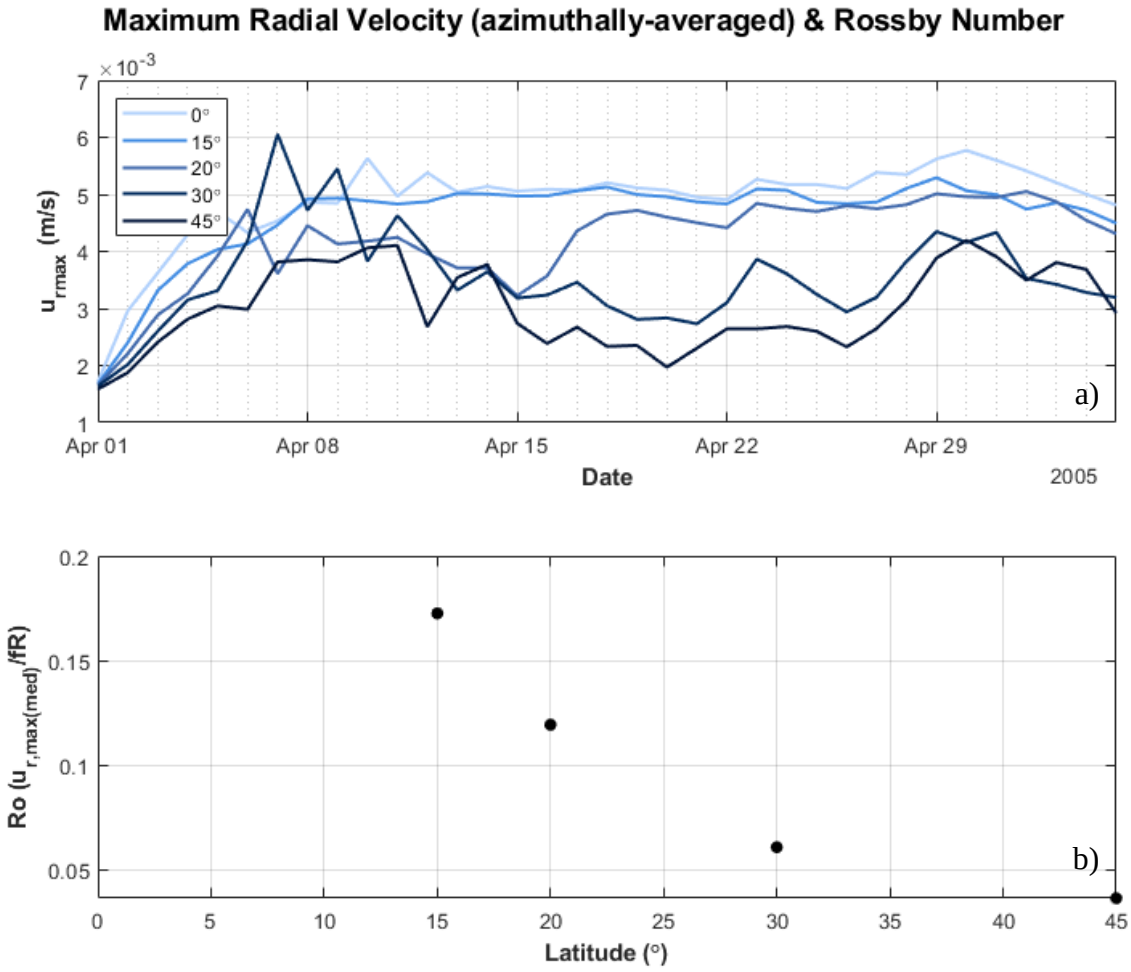

Figure 4-3. (a) The maximum daily and azimuthally averaged radial velocity for Slope 3. (b) The calculated Rossby number based on the median value for each case in (a). Note that latitude 0° case has Ro =∞, so it is not included in plot.

The chosen latitudes do not represent realistic locations for ice-covered lakes, but rather a simple method for tuning realistic Ro values. Based on the trend shown in Figure 4-3b, further increasing latitude would likely produce Ro with order of magnitude 10^{-3}. In the study by Ramon et al. (2021), they calculated the median Ro value for a distribution of lakes within latitudes 45-75° to be 10^{-1}-10^{0}, with 10^{-3} being less common. To satisfy the objective of analysing the gradual transition of decreasing Ro, it was found that five cases was adequate, so the range of Ro covered here was cut off at 10^{-2} since lower values have not been observed as often in real lakes. It is also important to note that at a latitude of 45°, the length scale of a lake would need to be greater than 20 m for Ro < 1 (with velocity scale 10^{-3} m/s). On the other hand, with the same velocity scale, Ro of O(10^{-1}) and O(10^{-2}) would correspond to length scales of ~200 m and ~450 m, respectively, for latitudes 70-90°.

4.2.4 Analysis Methods

Repeating the processing performed in Chapter 3, each slope and latitude case were analyzed according to the modelled output of blue ice depth, water temperature, and velocity. The intended analysis aimed to identify the how Coriolis changed the dominant flow feature observed in the base cases and quantify the differences in the resulting melt pattern, as well as determine how the ice profiles compare between the slope cases under this new circulation system.

Additional steps in the output processing that remained the same as the previous chapter include using daily averaged variables, and calculated values of ice melt rate and advective heat flux. The key difference in this method is the use of the full lake domain to calculate averages for each z-layer, due to the expected asymmetry of the circulation. To keep consistency with

snapshots on or near the simulation end date for the no Coriolis cases, May 5th was maintained as the cut-off date following the criteria discussed in section 3.2.4 of Chapter 3: (1) before sudden increase in melt rates indicating all ice is melted, (2) before the minimum ice depth melts below 0.02 m and (3) before the first of the slope cases reaches temperature of maximum density (T_{md}).

4.3 Results

4.3.1 Hydrodynamics

The processes for heat transport introduced to the water column remains unchanged from the previous simulations such that the changes to the initial temperature profile begin with shallow water warming that creates a density imbalance. Gravity currents are still expected to form under the same external forcing, but the transport of heat after that point will then be influenced by Coriolis. The velocity field under a rotating system becomes more three-dimensional as the fluid driven towards the lake centre is deflected instead and the transient motion becomes more difficult to capture in a single snapshot in time. However, we can still interpret any repeating or differing mixing responses to increasing degrees of Coriolis force.

The snapshot of centre temperature, centre radial velocity, and surface azimuthal velocity shown in Figure *4-4* was taken on May 5th. Latitude was used as a proxy for characterizing an increasing strength of Coriolis, with latitude 0° being identical in effect to excluding Coriolis from AEM3D's setup. Without Coriolis, the key components from the simulations discussed in Chapter 3 are the same: warm dense plume flowing downslope and warmer surface temperature in the centre relative to the sides. Once Coriolis is included, a consistent pattern can be observed regardless of latitude or bathymetry. The temperature perturbation is consistently colder in the centre than the lake sides, and the positive perturbation signal of the gravity current is more

diffuse. The dominating flow structure highlighted here is gravity currents becoming swept up in a rotating gyre where the warming water can accumulate and diffuse throughout the side regions, and cooler water stays effectively trapped in the centre.

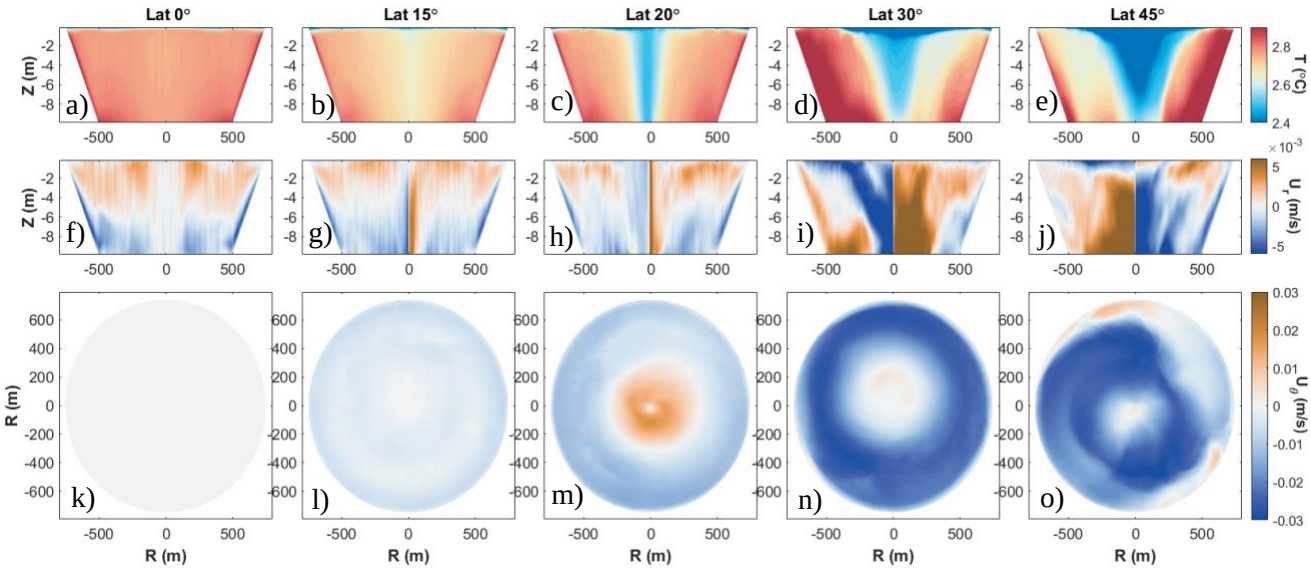

Figure 4-4. Hydrodynamics of Slope 3 on a daily averaged snapshot on the simulation cut off date, on May 5th, with (a)-(e) water temperature, (f)-(j) radial velocity through centre of lake, and (k)-(o) azimuthal velocities at surface.

The radial velocities in Figure *4-4* indicate some presence of cells circulating bottom waters to the surface, but it is clearly modified from what was seen without Coriolis. The abrupt change in magnitude along the centreline suggest water is moving in one direction, likely because of the lateral shifting of the gyre across the lake. Evidence for both anticyclonic and cyclonic circulation is observed in the azimuthal velocities and implies that each latitude case had a slightly different circulation regardless of the similarities in the temperature field. The

latitude 15° (Ro = 0.172) case had the weakest rotational motion in combination with the least restriction of lateral heat transport, while the latitude 20° (Ro = 0.119) case displays notable positive and negative azimuthal velocities and a distinct colder region in the centre, highlighting the transition to a gyre-dominated circulation system. The remaining latitude cases present similar results in both velocity and temperature perturbation patterns, with the latitude 45° (Ro = 0.036) case presenting the clearest anticyclonic gyre (i.e., minimal to no positive azimuthal velocity). Ramon et al. (2021) determined a trend in their modelling results of decreased inwards heat advection as Ro decreased, which is consistent with the results presented here. Additionally, the increasing strength of the outer gyre was also aligned with the modelling results of Ramon et al. (2021), shown by the rings of gyres moving in opposite directions for Ro of $O(10^{-1})$ and anticyclonic gyre with weak cyclonic motion in the centre for Ro of $O(10^{-2})$ in Figure *4-4*. In time, there is an oscillatory pattern shifting the region of cooler water around the lake, which pushes a corresponding warmer pocket of water to the opposite side.

To better distinguish the differences in heat distribution at the surface for each latitude run, the temperature perturbation was plotted in time across a centre slice through the surface layer (Figure *4-5*). Without Coriolis, the familiar pattern of warmer centre and cooler side temperatures can be observed, but this develops differently with Coriolis. As latitude increases (i.e., Ro decreases), the cool region in the centre becomes more predominant, with warmth being increasingly pushed to the sides. Latitude 15° (Ro = 0.172) starts to display elements of Coriolis-induced circulation, but the system re-adjusts, and the force trapping cooler water in the centre is weak. The periodicity of the gyre progression can also be seen for higher latitudes in Figure *4-5* with the arms of warm water protruding into the centre and a matching depression of cooler water into the sides on the opposite side of the lake around the radius of 500 m.

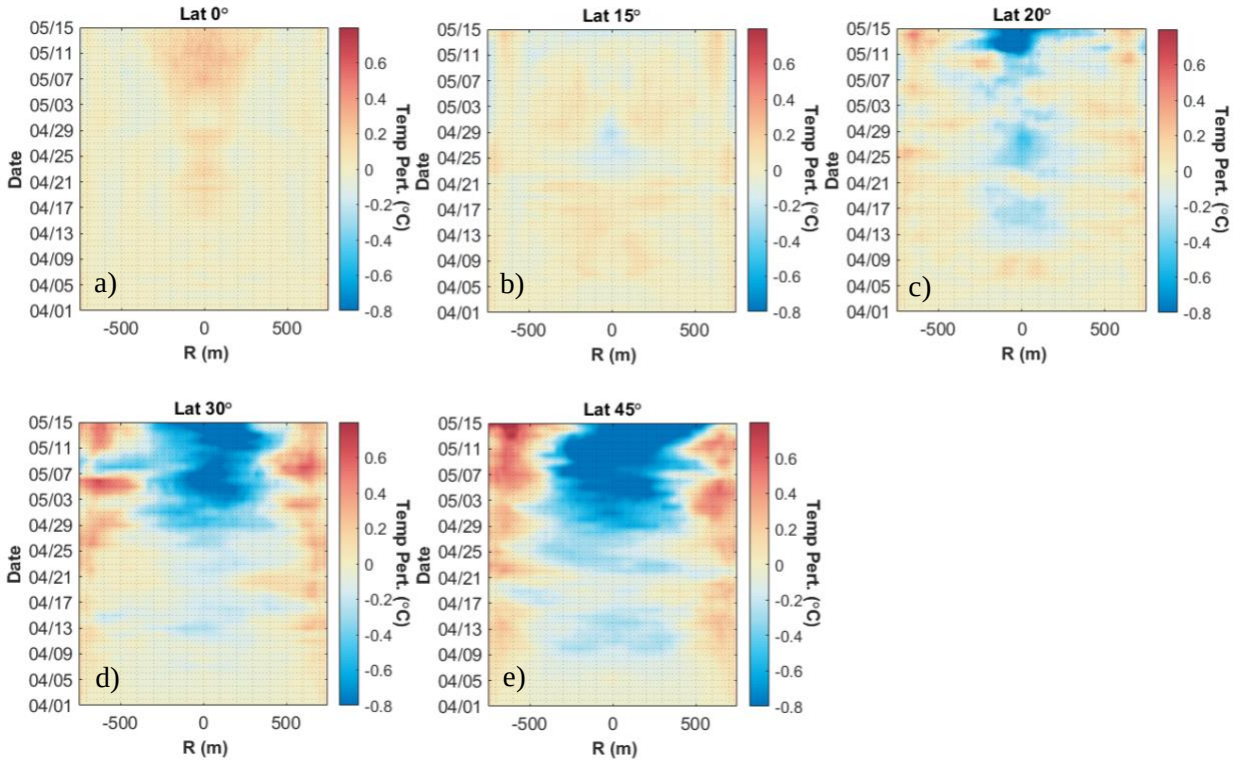

Figure 4-5. Temperature perturbation along centre axis of lake through time for each latitude run, presented for Slope 3.

In a non-rotating system, movement of heat in the lake could be easily understood via the radial advective heat flux and particularly the consistency in the heat of the gravity currents leaving the sloping region to the centre. However, the heat flux becomes less organized with Coriolis because the trapped heat in the lake sides will extend back and forth over the slope/centre boundary as a result of the oscillations, thus indicating a lack of consistent transport into or out of the sloping region. Figure *4-6* highlights the disruption to the heat transport and helps provide illustrative context for understanding why the interior remains colder, namely that

the heat flux with Coriolis is no longer consistently moving towards the lake centre at the bottom and away from the centre at the surface

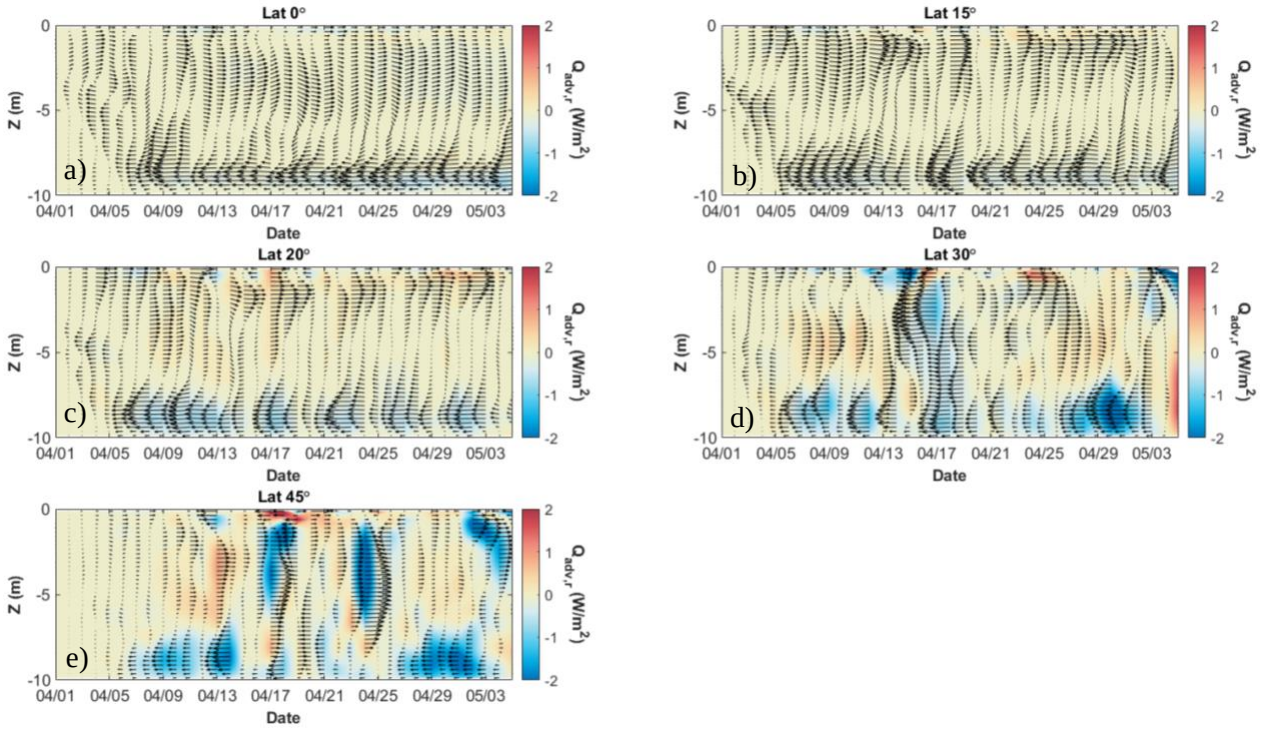

Figure 4-6. Advective heat flux based on temperature perturbation and radial velocity, plotted at the sloping/centre region boundary for Slope 3.

4.3.2 Ice Melt

A distinct quality of the melting pattern in the base cases (without Coriolis) was increased melting in the centre relative to the sides of the lake. This was attributed to the consistent inwards transport of heat. The hydrodynamics with Coriolis indicates that rather than net transport to the centre, heat becomes contrastingly contained outside the centre region. The movement of the gravity currents is suppressed due to their constant deflection, which prevents the lateral heat advection. The outcome of this is to have relatively warm surface temperatures at

the sides and cooler temperature in the centre, meaning preferential melting will take place in the sloping regions first. A snapshot of the ice profile was taken on the simulation cut-off date of May 5th (Figure *4-7*a, b). The transition in ice profiles from no Coriolis to the lowest Rossby number case (Ro = 0.036) shows a progression from thinnest ice in the centre to thickest. Furthermore, higher latitudes (lower Ro) display a widening of the thickest section in correspondence with increased relative importance of rotational force causing the spatial extent of the gyre to grow. To quantify how the trends of melting change with the latitude runs, the average difference to the ice thickness on the snapshotted day was calculated. The difference in ice thickness was computed as the difference between the mean ice thickness in the sloped region (grey shaded area in Figure *4-7*a, b) and the mean ice thickness in the centre (unshaded). The final panel in Figure *4-7* reiterates the transition from a negative difference in ice depth (i.e., centre is thinner) to a positive difference (i.e., centre is thicker). However, the key characteristic to note is that this crossover occurs approximately above Rossby numbers of 0.15. For velocities all within the same order of magnitude, it is shown here that the seemingly small decreases to Ro might matter in shifting the circulation regime and locations of increased melting.

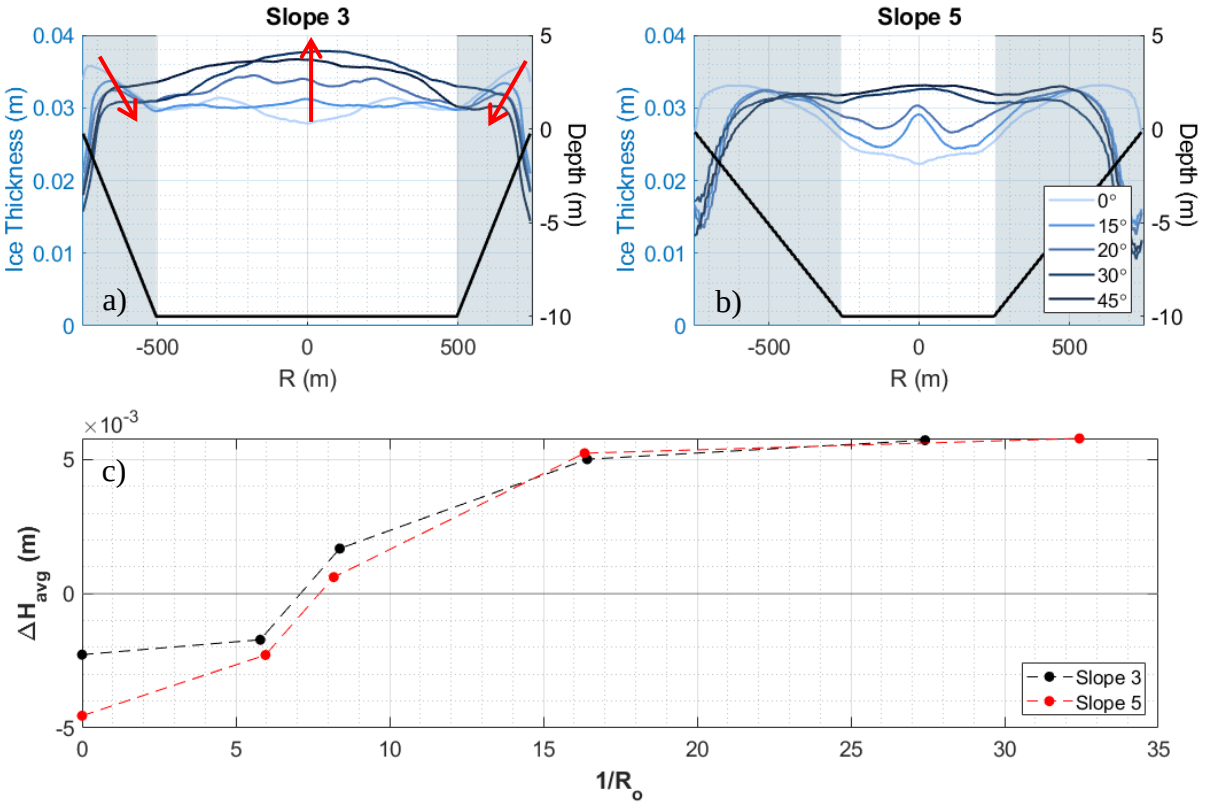

Figure 4-7. Final ice depth for each latitude run and the difference between average ice depth in centre and sides on final date. (a)-(b) Ice depth for the two slope cases on May 5th are shown as solid blue lines are for ice thicknesses of each latitude run, solid black lines denote the lake bathymetry, and shaded grey area indicate the side regions included in average; (c) average difference in ice thickness between centre and sides ($\Delta H_{avg} = H_{avg(centre)} - H_{avg(sides)}$) for both slope cases

4.4 Discussion

The idealization of a rotating lake system provides an opportunity to observe the correlation between Coriolis-driven mixing and ice melt. It was shown in Chapter 3 that bathymetry, an innate characteristic of a lake, influenced ice melting, so it is expected that

processes dependent on this characteristic will also have a consistent effect. The force of Coriolis on a given lake is variable according to its size, latitude, and velocity, but it would have an ever-present interaction with the bathymetric-induced circulation discussed in the previous chapter. Given that ice-covered lakes are subjected to some degree of rotation, Coriolis is typically a key element of the foundational circulation system in a lake.

The modelled hydrodynamics in this analysis highlight the changes to heat transport in the lake when the baseline conditions are affected by the Earth's rotation. These changes from the cases without and with Coriolis involve (1) the formation of a gyre in the lake interior, and (2) the inhibition of vertical and lateral motion. Previous work has also reported on the evidence of gyres and responding lake circulation in ice-covered lakes (Rizk et al., 2014; Forrest et al. 2013; Kirillin et al. 2015; Huttula et al. 2010).

The work presented here aimed to investigate the impact of increasing the relative importance of Coriolis, and the results suggests that the overall movement of heat changes with increasing latitude despite the lake's size and maximum velocities staying roughly constant. The characteristic velocity of the lake, defined in this study as the median value in time of the maximum azimuthally averaged absolute radial velocities was on the scale of 10^{-3} m/s for the latitudes 0, 15, 20, 30, and 45°. The inertial frequency varied little between cases ($f \sim 0.4\text{x}10^{-4}$ – $1\text{x}10^{-4}$), resulting in Rossby numbers with orders of magnitude between 10^{-1}-10^{-2}. The circulation for latitude 30° (Ro = 0.061) and 45° (Ro = 0.036) compared well with a study by Ramon et al. (2021), which showed the suppression of cross-shore transport from the littoral zone to the interior and the development of an anticyclonic gyre as a result of a geostrophic balance for Ro of $O(10^{-2})$. Contrastingly, for Ro of $O(10^{-1})$, gravity currents were modelled to still advect to the centre and allow interior warming but these currents become deflected into a cyclonic gyre with

the return flow in the littoral zone traveling in an anticyclonic gyre, representing an ageostrophic regime (Ramon et al., 2021). The latitude 20° simulation (Ro = 0.119) displayed similar behaviour to the $O(10^{-1})$ results in their study of two gyres with opposing rotational directions, however a key difference here is that the latitude 20° case also simultaneously exhibited characteristics of trapping heat in the lake sides. Differing from the other cases, latitude 15° (Ro = 0.172) still allowed heat from the gravity currents to be transported to the centre of the lake while displaying much milder surface azimuthal velocities, which is more alike to the warming trends associated to Ro $O(10^{-1})$ by Ramon et al. (2021) but not the velocity field. Based on the velocity field response to Ro of $O(10^{-3})$ shown in Ramon et al. (2021), it is expected that the results discussed here would continue its trend with a strengthening outer anticyclonic gyre and further suppression of cross-shore heat transport .

Despite differing methods to calculate the velocity scale for Ro, as well as the numerical modelling components such as the meteorological input and lake bathymetries with more/less prominent littoral regions, the results of this chapter agree well with the conclusions discussed by Ramon et al. (2021) while also considering the ice cover in the heat budget of the lake. Regardless of the Ro reported, there is overlap between the gyre circulation pattern in combination with its effect to heat transport. Based on the Ro values calculated in this work: $0.05 < Ro \prec 0.1$ resulted in more exaggerated lateral and vertical heat suppression than the higher Ro runs with an anticyclonic gyre and distinct cooler interior water, Ro ~ 0.12 demonstrated a pattern of centre and outer gyres rotating in opposite directions, allowing some distribution of heat to the centre but still a steady constraint of most heat in the sloping region, and finally $0.2 > Ro > 0.15$ (including $Ro \rightarrow \infty$ for latitude 0°) presented less disruption of heat transport to the centre with a less persistent, weaker gyre. In general, each latitude simulation involved a

circulation system with a gyre and, irrespective of rotating direction, some degree of reduced interior warming from the gravity currents.

A key objective of this work aims to use the knowledge of Coriolis' effect on the lake's physical mixing to better interpret the associated ice melt patterns. Despite the characteristic differences in the circulation patterns underneath the ice, the changes to the final ice profile follow a stepwise trend. Simply, with reducing Ro, ice thickness in the centre on average increases and ice thickness in the sides decreases. This trend in ice melt agrees with the discussed hydrodynamics where the surface temperature in the centre becomes increasingly colder with stronger Coriolis force while the radiatively generated gravity currents continue to add heat to the sloping region. The transition in the dominating under-ice circulation pattern from no Coriolis to the lowest Ro value is also reflected in the final ice profile. It is only after the latitude 15° run (Ro = 0.172), that the difference in ice depth between the centre and sides changes from negative to positive, which also corresponds to the switch to the more geostrophic balanced anticyclonic motion. Despite still being within the same order of magnitude, when Ro < 0.15, the outside region of the ice cover melts first, whereas for Ro > 0.15, the inside region melted first.

With the distinction between the sloping and centre region playing a role in defining the melting tendencies, this chapter also looked at the effect of two bathymetries with different sloping region surface areas. The size of the gyres did not change much because peak velocities remained relatively constant, however the region of thicker ice stayed contained in the centre region even if the extent of cooler water was wider. The ice depths were overall lower with larger % sloping region because of lower water volumes warming quicker, and the average difference between ice depth in the centre and sides was slightly milder.

4.5 Limitations

The limitations previously discussed in Chapter 3 are still relevant here for this analysis, with the core constraints including the idealized assumptions, AEM3D limitations, and validation of the results to reported data. Adding Coriolis helped address the previous chapter's greatest limitation, but it still omits precipitation, sediment heating, strong stratification, ice cover oscillations, and inflows/outflows. The decision to exclude these features revolved around the intention to (1) avoid over complication of the system, such as through snowfall introducing heterogenous penetrative radiation or needing to disentangle currents influenced by oscillations versus gravity currents, as well as (2) leave out features that would likely reinforce the gravity current mechanism already being observed, such as sediment heating and inflows. A key result of this work was the reversed trend to ice thickness heterogeneity from the no Coriolis scenario, and this was not able to be validated with real ice-covered lakes melting behavior. This consideration is impeded by limited available data on the spatial characteristics of ice cover thickness during the melting period. The idealized truncated cone shape was a necessary simplification to begin understanding the interaction of bathymetry and ice melt, but the shape nevertheless limits applicability to many lakes affected by Coriolis. Future work to strengthen this analysis should examine the transition of rotational force on more complicated bathymetry and observe if the key results fundamentally change.

4.6 Conclusion

The dependency of Coriolis on lake size and latitude makes it as intrinsically important to the heat transport in a lake. While under-ice gyre movement has been discussed before in

numerical simulations and field studies, there is still more to understand on how these circulation systems develop and interact with the lake's shape. Past work has highlighted a variety of circulation systems driven by Coriolis force that can develop in ice-covered lakes, emphasizing how unique physical processes can be to a specific lake. This study differs from others by using a hypothetical lake with foundational features and driving forces present in most lakes to identify how the core elements of Coriolis-induced mixing develop without additional lake-specific influences. By increasing the relative significance of rotation on a simple, idealized lake while keeping all other features constant, it was observed how lateral heat movement becomes progressively disrupted and constrained to the sides. Consequentially, the ice cover tended towards increased melting in the sloping region, which occurred after a shift in the mixing regime to more geostrophic conditions. In real lakes, melting at the sides can be attributed to warm runoff, warm inflows possibly entering with increased velocity, and shallow depths. However, as shown here, an additional factor accelerating melting in shallower area may be attributed to Coriolis force. There is also a clear contribution from the bathymetry changing aspects of the ice melt magnitude and shape as the gyre develops because any differences in the results between the slope cases are directly correlated to lake bottom interacting with the flow features. Many limitations still exist in such a simplistic numerical setup, but it provides helpful groundwork to build upon with increasing complexity and compatibility with real lakes. Coriolis is a realistic forcing to many lakes, and it is likely that its presence would cause a repeating, observable signal in the ice melting pattern that may not otherwise be associated with the Earth's rotation. The results of this analysis undoubtedly demonstrate Coriolis's signal in the ice melt, and future work could also explore the effect of other factors excluded here on this signal.

4.7 References

Caramatti, I., Peeters, F., Hamilton, D., & Hofmann, H. (2019). Modelling inter-annual and spatial variability of ice cover in a temperate lake with complex morphology. *Hydrological Processes*, 34, 691-704, doi: 10.1002/hyp.13618

Cortés, A., & MacIntyre, S. (2020). Mixing processes in small arctic lakes during spring. *Limnology and Oceanography*, *65*(2), 260–288. https://doi.org/10.1002/lno.11296

Farmer, D. M. (1975). Penetrative convection in the absence of mean shear. *Quarterly Journal of the Royal Meteorological Society*, *101*(430), 869–891. https://doi.org/10.1002/qj.49710143011

Forrest, A. L., Laval, B. E., Pieters, R., & S. S. Lim, D. (2013). A cyclonic gyre in an ice-covered lake. *Limnology and Oceanography*, 58(1), 363–375. https://doi.org/10.4319/lo.2013.58.1.0363

Forrest, A. L., Laval, B. E., Pieters, R., & Lim, D. S. S. (2008). Convectively driven transport in temperate lakes. *Limnology and Oceanography*, 53(5part2), 2321–2332. https://doi.org/10.4319/lo.2008.53.5_part_2.2321

Hodges, B., & Dallimore, C. (2022). Aquatic Ecosystem Model: AEM3D, Hydrodynamics Science Manual. Hydronumerics: Docklands, Australia

Huttula, T., Pulkkanen, M., Arkhipov, B., Leppäranta, M., Solbakov, V., Shirasawa, K., & Salonen, K. (2010). Modelling circulation in an ice-covered lake. *Estonian Journal of Earth Sciences*, 59(4), 298. https://doi.org/10.3176/earth.2010.4.06

Jansen, J., MacIntyre, S., Barrett, D. C., Chin, Y., Cortés, A., Forrest, A. L., Hrycik, A. R., Martin, R., McMeans, B. C., Rautio, M., & Schwefel, R. (2021). Winter Limnology: How do Hydrodynamics and Biogeochemistry Shape Ecosystems Under Ice? *Journal of Geophysical Research: Biogeosciences*, *126*(6), e2020JG006237. https://doi.org/10.1029/2020JG006237

Kirillin, G. B., Forrest, A. L., Graves, K. E., Fischer, A., Engelhardt, C., & Laval, B.E. (2015). Axisymmetric circulation driven by marginal heating in ice-covered lakes. *Geophysical Research Letters*, 42, 2893–2900. https://doi.org/10.1002/2014GL062180.

Kirillin, G., Leppäranta, M., Terzhevik, A., Granin, N., Bernhardt, J., Engelhardt, C., Efremova, T., Golosov, S., Palshin, N., Sherstyankin, P., Zdorovennova, G., & Zdorovennov, R. (2012). Physics of seasonally ice-covered lakes: A review. Aquatic Sciences, 74(4), 659–682. https://doi.org/10.1007/s00027-012-0279-y

Mironov, D., Terzhevik, A., Kirillin, G., Jonas, T., Malm, J., & Farmer, D. (2002). Radiatively driven convection in ice-covered lakes: Observations, scaling, and a mixed layer model. *Journal of Geophysical Research: Oceans*, *107*(C4). https://doi.org/10.1029/2001JC000892

Oveisy, A., Boegman, L., & Imberger, J. (2012). Three-dimensional simulation of lake and ice dynamics during winter. *Limnology and Oceanography*, 57(1), 43-57, doi:10.4319/lo.2012.57.1.0043

Ramón, C. L., Ulloa, H. N., Doda, T., Winters, K. B., & Bouffard, D. (2021). Bathymetry and latitude modify lake warming under ice. *Hydrology and Earth System Sciences*, 25(4), 1813–1825. https://doi.org/10.5194/hess-25-1813-2021

Rizk, W., Kirillin, G., & Leppäranta, M. (2014). Basin-scale circulation and heat fluxes in ice-covered lakes. *Limnology and Oceanography*, 59(2), 445–464. https://doi.org/10.4319/lo.2014.59.2.0445

Rogers, C. K., Lawrence, G.A., & Hamblin, P.F. (1995). Observations and numerical simulation of a shallow ice-covered midlatitude lake. *Limnology and Oceanography*,40(2), 374-385, doi:10.4319/lo.1995.40.2.0374

Salonen, K., Pulkkanen, M., Salmi, P., & Griffiths, R. W. (2014). Interannual variability of circulation under spring ice in a boreal lake. *Limnology and Oceanography*, 59(6), 2121–2132. https://doi.org/10.4319/lo.2014.59.6.2121

Ulloa, H. N., Winters, K. B., Wüest, A., & Bouffard, D. (2019). Differential Heating Drives Downslope Flows that Accelerate Mixed-Layer Warming in Ice-Covered Waters. *Geophysical Research Letters*, 46(23), 13872–13882. https://doi.org/10.1029/2019GL085258

Yang, B., Wells, M.G., McMeans, B.C., Dugan, H.A., Rusak, J.A., Weyhenmeyer, G.A. et al. (2021). A new thermal catagorization of ice-covered lakes. *Geophysical Research Letters*, 48, e2020GL091374. https://doi.org/10.1029/2020GL091374

Chapter 5 :

Application of Idealized Setup to Real Bathymetry Data

5.1 Introduction

The underlying goal of this thesis is to investigate the role that bathymetry plays in ice melt, modulated by the lake hydrodynamics. The applicability of this work is thus strengthened by considering how the conclusions drawn in Chapter 3 and 4 uphold with real bathymetry data. In this chapter, the same idealized setup discussed in the preceding chapters (i.e., meteorological forcing, initial temperature profile, and initial unform 0.35 m thick ice cover) is applied to the bathymetry of Base Mine Lake.

5.2 Methods

Base Mine Lake is a pit lake located in northeast Alberta, Canada (57°1'N, 111°37'W, elevation 308 m AMSL, surface area 7.8 km^2) (Tedford et al., 2019). It has a maximum depth of 13.2 m with relatively steep side walls. The bathymetric survey, provided to us by Dr. Edmund Tedford, had a horizontal resolution of 1 m, which was converted to 6.25 m to match the resolution chosen for the idealized truncated cone bathymetry. The vertical resolution of the simulations was similarly maintained at 0.25 m. The velocities modelled in this chapter were in same order of magnitude as the previous chapters, so a time step of 22.5 s was maintained. With this setup, the real bathymetry data was run through the Aquatic Ecosystem Model 3D (AEM3D). The model simulated 2 months of melting conditions from April 1st – May 31st, with results compared on May 5th to be consistent with the previous chapters. Figure *5-1* contains the

bathymetry contours with a solid red line indicating a cross-sectional slice passing through both the deeper eastern side of the lake and shallower western side.

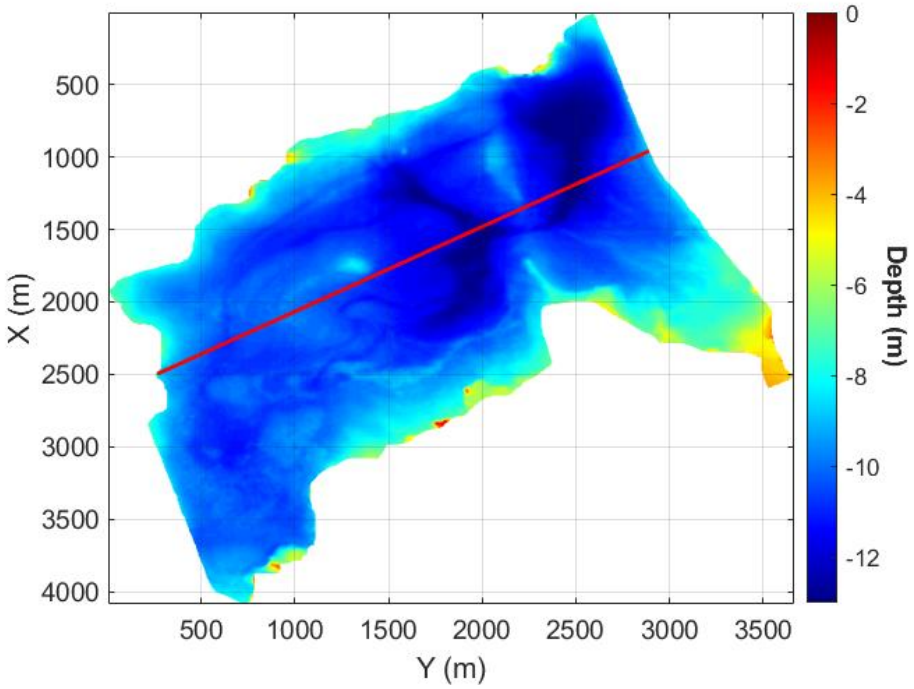

Figure 5-1. Bathymetry of Base Mine Lake with horizontal resolution of 6.25 m (altered from the 1 m survey resolution to match coarser grid of idealized bathymetry simulations). Solid red line represents the cross-sectional slice presented from right (east) to left (west).

The real bathymetry setup was run both with and without Coriolis. For the Coriolis case, the latitude was set at the real value of 57.1°. The full domain was considered here due to the asymmetrical nature of the lake, so temperature perturbation (T') was calculated by subtracting the temperature by the horizontal mean at each depth, consistent with the Chapter 4 method. Velocity along the slice was computed based the angle of the cross-sectional slice to the horizontal y-axis,

$$\theta_{slice} = \tan^{-1}\frac{Y_{slice}}{X_{slice}} \quad (1)$$

$$u_{slice} = u\cos\theta_{slice} + v\sin\theta_{slice}. \quad (2)$$

5.2 Results & Discussion

The surface temperature and ice depth on May 5th for the no Coriolis and Coriolis runs are given in Figure *5-2*. Without Coriolis, the warmest temperatures are along centreline of the lake with the highest values occurring in the deepest depths. The thinnest ice depths also correspond with those regions. Including Coriolis shifted the circulation into a more dynamic, complicated system, similar to what was noted in Chapter 4. Figure *5-2*b is a plot of the surface temperature, from which we infer the presence of several, smaller rotational features rather than the basin-scale gyres observed with the simpler bathymetry. The ice melt pattern in the Coriolis run mirrors the movement of heat at the surface, as expected.

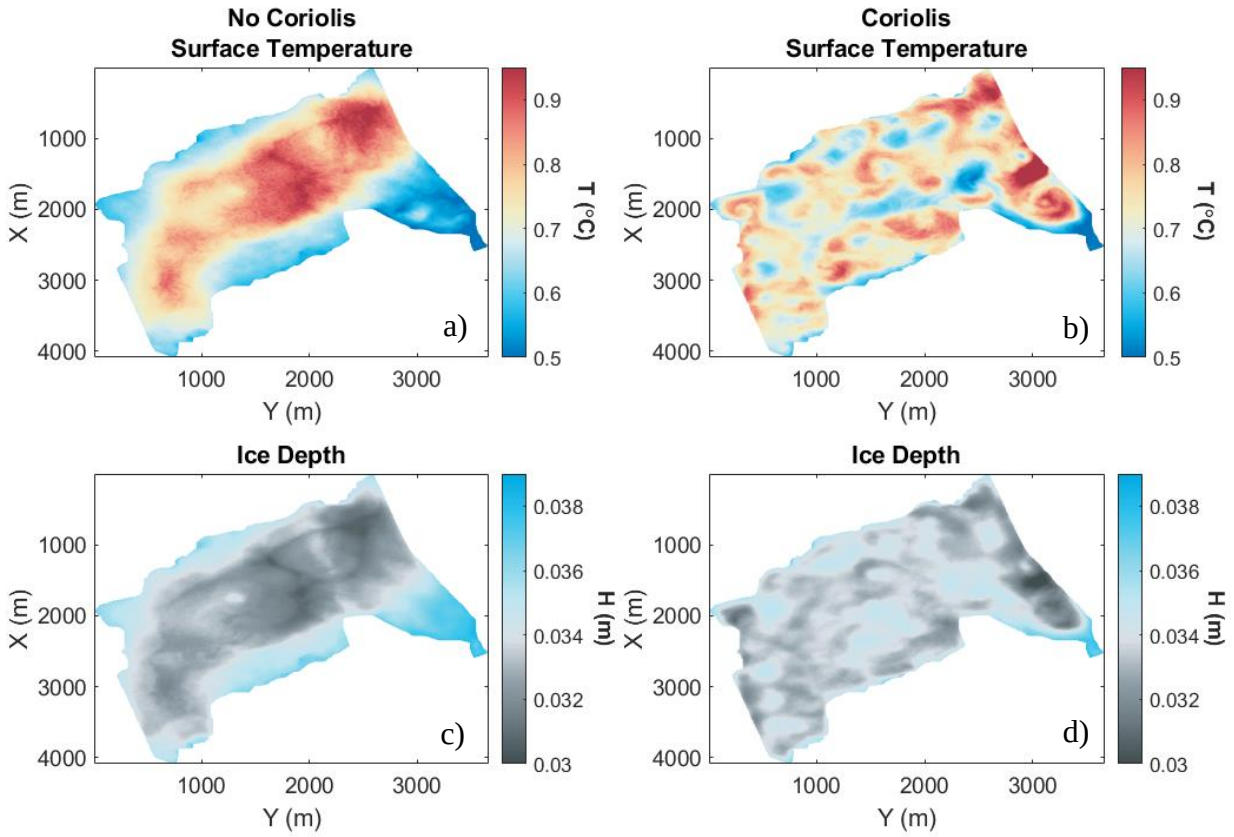

Figure 5-2. (a)-(b) surface temperature, and (c)-(d) ice depth on May 5th for the no Coriolis and Coriolis runs with the real bathymetry data

The results of the no Coriolis run are consistent with Chapter 3, where the central part of the lake (i.e., deepest) has surface temperatures that are warmer compared to the surface temperatures of the littoral zones. The signal of the lake bathymetry is also evident in the melting pattern, with the complexity of the deepest depth contours visible in the ice cover. The most important observation of the real bathymetry results in Figure *5-2* is the reinforcement of the overall trends discussed in the previous chapters: without Coriolis, ice will melt inside-out, whereas with Coriolis, melting is focused more along the outside first.

The temperature perturbation and velocity of the water column along the cross-sectional slice are given in Figure 5-3. Evidence of gravity currents is less distinct in these runs compared to the truncated cone bathymetry cases, but lateral heat transport is still expected to be a key process driving interior heating for the no Coriolis case. Although Base Mine Lake has roughly vertical side walls, its temperature structure did not match the idealized cylinder bathymetry results, because spatial variability in depth through the lake (rather than a flat bottom) contributed to differential heating in the water column. Figure 5-3c indicates two circulation cells moving in opposite directions, with surface waters moving to the shore on the east side and towards the center on the west side. In the Coriolis run, the temperature perturbation is more similar to Chapter 4 with a cooler region of water in the centre with trapped heat along the sides. Radial velocity under the influence of Coriolis displays multiple circulation cells along the cross-section moving negatively inwards at the surface.

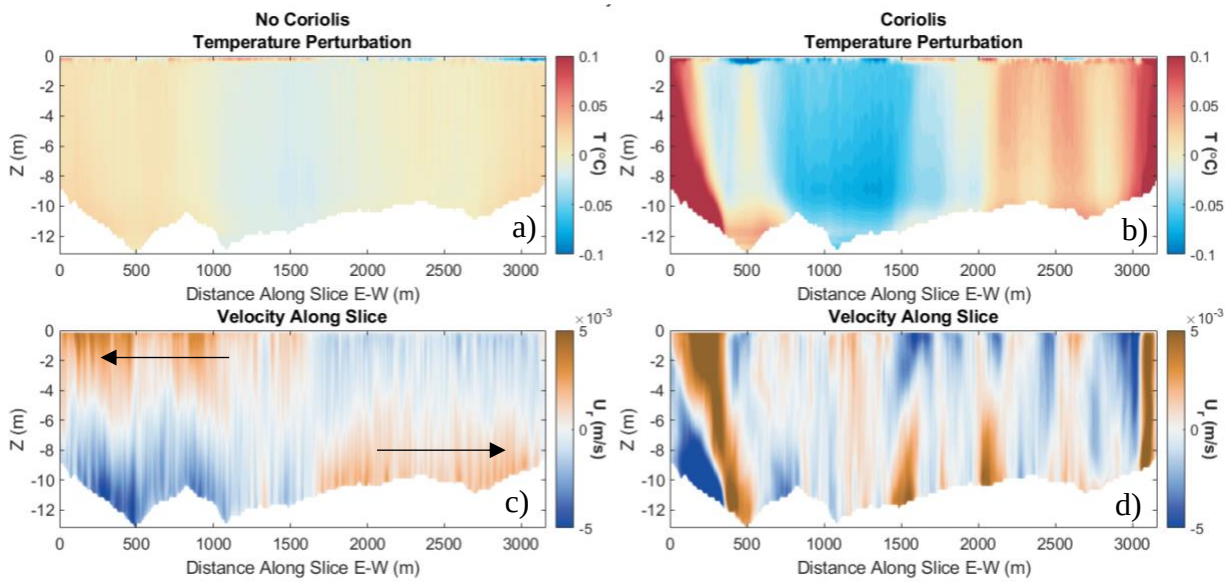

Figure 5-3. (a)-(b) temperature perturbation, and (c)-(d) radial velocity along cross-sectional slice on May 5th for the no Coriolis and Coriolis runs with the real bathymetry data

The modelled results can be qualitatively compared to satellite images of the ice melt at Base Mine Lake, shown for 3 consecutive years in Figure 5-4.

Figure 5-4. Satellite images of partially melted ice cover of Base Mine Lake (provided by Dr. Edmund Tedford)

The modelled ice depth from the no Coriolis run (Figure *5-2*c) agrees very well with the real ice melt photographs, even though it was initially expected that the real lake would be better represented by the Coriolis results. The results of these simulations suggest that bathymetry is less visible in the melting matter with Coriolis. AEM3D modelled peak radial velocities of $O(10^{-3})$, which would correspond with Rossby numbers (Ro) ranging between $O(10^{-3})$-$O(10^{-2})$ if the characteristic length scale is approximately half of the cross-section length (~1500 m). Based on the latitude of Base Mine Lake at 57.1° and modelled velocities, the Rossby radius would range between approximately 8 – 70 m, which is smaller than the Rossby radius values predicted for the idealized bathymetries at roughly 20 – 130 m because the f value is higher. This indicates a regime in which Coriolis will be important, but the satellite images suggest that Coriolis-driven mixing is likely not occurring in the way presented by this thesis. It is also possible that the true

Ro value in Base Mine Lake is higher. There was no available data to validate the modelled velocities, so their order of magnitude could be higher. Other factors unique to Base Mine Lake whose influence on the ice melt was not considered is the ebullition of methane from the sediment at the deepest depth region (Zhao et al., 2022), salt concentration affecting stratification, sediment heat flux, and turbidity affecting light penetration (Tedford et al., 2019).

5.3 Conclusions

In terms of the bathymetric influence on the ice cover of a lake where rotational effects either do not or do matter, AEM3D was found to produce a consistent trend with more complex bathymetry. This conclusion helps validate the observations from Chapter 3 and 4. Despite the fact that this idealized setup ignores any real properties of this particular lake, such as its salt concentration, location-specific meteorological conditions, ice cover structure, stratification, or methane bubbles, AEM3D can still capture the ice melt pattern well when Coriolis is turned off. This suggests that the influence of bathymetry on ice melt might transcend the influence of other factors. Applying hypothetical atmospheric warming and a linear weak stratification condition did not prevent this result from being observed, regardless of its dissimilarities with the real lake. It is recommended that future work investigate the satellite ice melt data for other lakes to compare with the results of these simulations.

5.4 References

Tedford, E., Halferdahl, G., Pieters, R., & Lawrence, G. A. (2019). Temporal variations in turbidity in an oil sands pit lake. *Environmental Fluid Mechanics*, *19*(2), 457–473. https://doi.org/10.1007/s10652-018-9632-6

Zhao, K., Tedford, E. W., & Lawrence, G. A. (2022). Ebullition Regulated by Pressure Variations in a Boreal Pit Lake, *Frontiers in Earth Science*, 959. https://doi.org/10.3389/feart.2022.850652

Chapter 6 :

Conclusions

The melting patterns and hydrodynamics for an idealized ice-covered lake subjected to warming conditions were modelled using the Aquatic Ecosystem Model 3D (AEM3D) with the objective of capturing and characterizing the influence of lake shape on differential melting of the ice cover. Past work has provided the foundation for understanding heat transport and mixing in ice-covered lakes driven by penetrative radiation and Coriolis, where circulation systems induced by gravity currents with (Huttula et al., 2010; Kirillin et al., 2015; Ramon et al., 2021) and without (Farmer, 1975; Salonen et al., 2014; Ulloa et al., 2019) the influence of the Earth's rotation have been observed. However, a missing piece in other studies has been linking both the ice cover melting patterns and possible signature of bathymetry to these circulation observations. This thesis begins to address the open question by analysing the complete picture of bathymetry, circulation, and ice melt with a simplified, systematic setup.

In Chapter 3, a series of simplified truncated cone bathymetry cases were constructed with seven side slope variations and tested under base conditions. The main under-ice physical processes simulated by AEM3D were found to be driven by penetrative convection, consisting of density currents and convection plumes. Aside from the reference cylinder case with vertical walls, each case displayed similar characteristics of warmer temperatures along the sloping region bottom waters aligned with negative inwards radial velocity, and cooler water along the sloping region surface waters with positive outwards radial velocity. The dominant circulation system identified here was the sinking of warm, dense water along the lake sides that transported heat towards the interior, where intersecting currents drove an upwelling of warmer water that

forced the cooler water at the surface back towards the sides to compensate. A conceptual model delineating the lake into three major compartments revealed that on average, the upper layer of the sloping region was consistently cooler than the centre of the lake, and furthermore, at the boundary between the three compartments, the advective heat flux showed a persistent movement of heat towards the centre. AEM3D modelled the thinnest ice at the lake centre, and thicker ice at the sides, consistent with the heterogeneity of the surface layer temperature structure. The overarching trends of circulation and ice melt were similar between differing bathymetries, but in each case the final ice shape changed in parallel to the changes to bathymetry (i.e., radius of the region with thinnest ice decreased with decreasing bottom radius). This result confirmed that there is a direct influence of bathymetry on ice melt. The lateral location in which the density currents stabilized (the lake bottom for this unstratified lake) dictated an approximate boundary for the upwelling current. Chapter 3 provided a foundation for understanding this relationship between bathymetry and ice melt that can still have implications to real lakes. Regardless of the source of heat, horizontal convection is a process commonly observed in lakes, and the scale of a lake can be small enough to be both below the scale of meteorological variability and unaffected by Coriolis. A lake under these criteria may display a similar trend of melting from the inside-out.

In Chapter 4, two selected bathymetry cases were run with Coriolis turned on for latitudes of 0°, 15°, 20°, 30°, and 45°. The Rossby Numbers (Ro) for latitudes above zero were calculated to be on the order of magnitude of 10^{-1}-10^{-2}. Each run was thus placed within a similar regime of Coriolis force but still presented different circulation responses. Increasing latitude (as a proxy for Ro) displayed a transition in mixing from the horizontal convection advecting heat to the centre shown in Chapter 3 to a basin-scale gyre inhibiting offshore currents. Strengthening the

rotational effect was found to produce a region of cooler water trapped within the bounds of the gyre because the heat from the gravity currents was restricted from travelling inwards. The associated effect on the ice cover was a reversal of the regions subjected to quicker melting, where the thinnest ice was now predicted to be along the sides where the heat was trapped and thickest ice in the centre. This shift was predicted to occur between the latitude 15° (Ro = 0.172) and 20° (Ro = 0.119) cases, where Ro crossed a threshold of 0.15 and the circulation displayed more characteristics of a geostrophic regime. Again, the changes to ice melt and hydrodynamics for the two bathymetry cases considered here with decreasing Ro were overall similarly trended. However, the slight differences to the final ice shape can be confidently attributed the differences between the two bathymetries given this is the only variance. The centre of the ice cover that is increasing in thickness with increasing latitude is approximately aligned in radius to the bottom radius, meaning the bathymetry with the larger sloping region has a corresponding larger area of thinner ice. The main conclusion of this chapter was that Coriolis will influence currents such that the ice will melt in a opposite pattern to a non-rotating system (i.e., outside-in), but the signal of bathymetry will still be present in influencing the boundary of thicker/thinner ice regions. Many lakes in the Northern Hemisphere that fall within ice zone latitudes can be affected by some degree of the Earth's rotation, effectively making Coriolis a foundational flow feature that will have implications on heat transport and mixing. This work can thus be applied to better understand the ice melt patterns observed on lakes large enough for rotational effects to matter, as well as providing a possible explanation for why lakes may melt on the outsides first beyond the general interpretation of it being a result of shallow water warming.

In Chapter 5, the bathymetry of Base Mine Lake was run through AEM3D with the same idealized input. A complete validation of the results was not performed due to lack of winter

observations, but a simple analysis of the hydrodynamics and ice melt was performed for simulations with and without Coriolis. The model maintained the trend that without Coriolis, ice melted inside-out, and with Coriolis, ice melted outside-in. In comparison to satellite images of the partially melted ice cover of Base Mine Lake, the no Coriolis model results agreed better than the run with Coriolis. This result was unexpected but may suggest Base Mine Lake has other factors reducing rotational effects. Chapter 5 helped consolidate the conclusions of the previous chapter by demonstrating that bathymetry's signal can be captured in the ice melt regardless of other lake-specific processes present. This provides confidence in the idealized results and brings this study closer to being applicable to real lakes.

There is a lot of opportunity to build upon this work to continue learning from idealized simulations how various lake properties will interact with bathymetry, while also using this information as a predictive measure of a melting response to a given bathymetry. Suggestions for future work are summarized in the following points.

1. Validation of the melting pattern trends for physical lakes that are expected to be either affected or unaffected by Coriolis through compiling a photographic dataset of ice covers during melting season over multiple years. The conclusions here would also be further advanced by modelling a real lake that can be compared with field data and observations.
2. Increase complexity of simulations, first with the inclusion of snow to test the sensitivity of bathymetry's signal in the ice shape when warming of the water column is restricted by a snow or white ice layer. Sediment heating, inflows, and stronger stratification are not expected to affect the density current generation but are still realistic features of many lakes that should be investigated with this setup.

3. Varying additional bathymetry features other than side slope while maintaining a similar simulation setup simplicity to explore which features have the strongest potential to alter the circulation and the resulting ice melt.

6.1 References

Farmer, D. M. (1975). Penetrative convection in the absence of mean shear. *Quarterly Journal of the Royal Meteorological Society*, *101*(430), 869–891. https://doi.org/10.1002/qj.49710143011

Huttula, T., Pulkkanen, M., Arkhipov, B., Leppäranta, M., Solbakov, V., Shirasawa, K., & Salonen, K. (2010). Modelling circulation in an ice-covered lake. *Estonian Journal of Earth Sciences*, 59(4), 298. https://doi.org/10.3176/earth.2010.4.06

Kirillin, G. B., Forrest, A. L., Graves, K. E., Fischer, A., Engelhardt, C., and Laval, B.E. (2015). Axisymmetric circulation driven by marginal heating in ice-covered lakes. *Geophysical Research Letters*, 42, 2893–2900. https://doi.org/10.1002/2014GL062180.

Ramón, C. L., Ulloa, H. N., Doda, T., Winters, K. B., & Bouffard, D. (2021). Bathymetry and latitude modify lake warming under ice. *Hydrology and Earth System Sciences*, 25(4), 1813–1825. https://doi.org/10.5194/hess-25-1813-2021

Salonen, K., Pulkkanen, M., Salmi, P., & Griffiths, R. W. (2014). Interannual variability of circulation under spring ice in a boreal lake. *Limnology and Oceanography*, 59(6), 2121–2132. https://doi.org/10.4319/lo.2014.59.6.2121

Ulloa, H. N., Winters, K. B., Wüest, A., & Bouffard, D. (2019). Differential Heating Drives Downslope Flows that Accelerate Mixed-Layer Warming in Ice-Covered Waters. *Geophysical Research Letters*, 46(23), 13872–13882. https://doi.org/10.1029/2019GL085258

Appendix A

AEM3D Ice Model Bug

When completing a heat budget for the ice during freezing period, we identified that the wrong latent heat was used when calculating the rate of ice growth. The source code indicated that latent heat of vaporization was being used, while the latent heat of fusion is what should be used. It was also noted during this process that the fraction of incoming radiation divided into visible and near infrared spectral bands (A_1 and A_2) differed from the values given by Oveisy e al. (2012). Rather than a ratio of 70% visible and 30% near infrared, the source code splits solar radiation into 49% visible and 51% near infrared (refer to Chapter 2.2.1 equation 10-11). This change was done to maintain consistency with the Water Quality code in AEM3D.

A test simulation was run with constant freezing conditions for a cylinder bathymetry, where the ice depth was assumed to be controlled only by the accretion equation at the blue ice-water interface (i.e., Q_f, Q_w, and Q_o are the fluxes that matter). There was no snow or rainfall included in the simulation, simplifying the ice model to a single blue ice layer. The simulation timestep and output timestep were set to be identical to avoid any interpolation issues. The atmospheric-ice conduction heat flux (Q_o) and water-ice heat flux (Q_w) were found to agree well with the variables output from AEM3D, however this was not the case for the ice-water heat flux (Q_f).

At each time step, ice depth was calculated based on the following steps with an initial condition assumption of $h_{i(1)}$ = 0.001 m. This is calculated:

$$\rho_i L_W \frac{dh}{dt} = Q_f + Q_w \quad (1)$$

$$dh_{i(t-1)} = \frac{-(Q_{f(t-1)} + Q_{w(t-1)})}{\rho_i L_w}\, dt \quad (2)$$

$$h_{i(t)} = h_{i(t-1)} - dh_{i(t-1)} \quad (3)$$

However, the blue ice depth determined from the above calculations were found to be very different from the AEM3D output depth. The left side and right side of equation (1) was computed, and the results are presented in Figure A-1.

Figure A-1 shows the difference between the right side and left side of equation (1) to be off by a factor of approximately 8.5 (see the difference between the purple and blue lines). The source of this scaling error was found to result from the AEM3D code using the latent heat of vaporization for ice in the ice depth calculations rather than the latent heat of fusion for water (See line 1599 from aem3d_thermodynamics.f90). Figure A-*2* provides a snapshot of the ice ablation and accretion subroutine in the thermodynamics ice algorithm (AEM3D source code - developers branch), where the latent heat of vaporization for ice is shown being referenced. This value is defined in the thermodynamics utilities script (line 58) as 2.833×10^6 J/kg, which is roughly 8.5x higher than the expected latent heat of fusion for water, 3.34×10^5 J/kg. Although not shown in Figure A-*2*, the same reference issue was found for the ice depth calculation in the ice surface melt subroutine (beginning on line 1474 in aem3d_thermodynamics.f90).

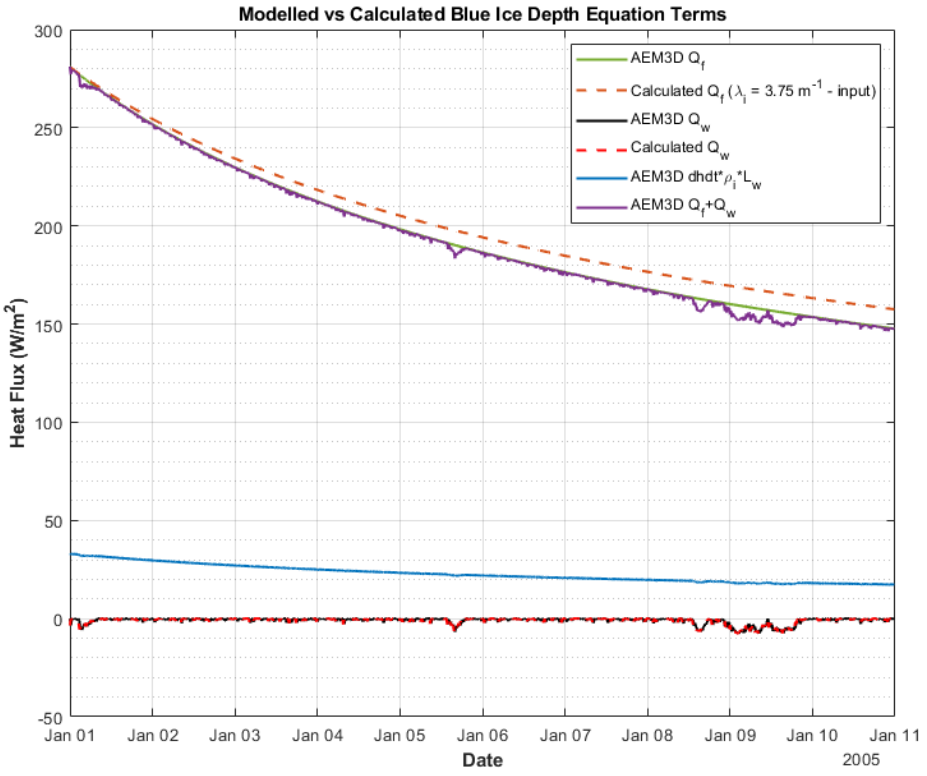

Figure A-1. AEM3D output vs calculations of heat fluxes in blue ice depth equation. This plot is before the bug fix, where the blue and purple lines should match but do not.

```
1596
1597      heat_flux = ice_water_heat_flux + water_ice_heat_flux
1598
1599      dhdt = - (heat_flux) / RHO_BLUE_ICE / LATENT_HEAT_VAP_ICE
1600
1601      dh = dhdt*del_t ! +ve dh is loss of ice to water
1602
1603      if (dh <= blueice_depth) then  ! will account for all accretion and ablation up to depth of blue ice
1604        blueice_depth = blueice_depth - dh
1605        ice_volflux = ice_volflux + dhdt * RHO_BLUE_ICE / surf_density
1606      else
1607        blueice_depth = 0
1608        ice_volflux = ice_volflux + blueice_depth/del_t * RHO_BLUE_ICE / surf_density
1609        heat_flux = heat_flux - (dh-blueice_depth) * RHO_BLUE_ICE * LATENT_HEAT_VAP_ICE / del_t
```

Figure A-2. Snapshot of thermodynamics ice algorithm in the AEM3D developer's branch

This issue was communicated to Chris Dallimore at Hydronumerics, and the code was updated with the proper latent heat with new model executables published on their website Nov 27, 2023.

Appendix B

Base Case Development

The first iteration of the base case consisted of a horizontal resolution of 25m, vertical resolution of 0.25m, and time step of 180s, with a freezing period of approximately three months that allowed for virtually uniform ice growth to a depth of 0.35m, and a melting period of nearly two months. The air temperature and solar radiation inputs for this setup were designed to be extreme, with a switchover between the cooling and warming conditions occurring over one day. One issue observed with this base case was a consistent kink causing an abrupt change in the result trends that was improved by fixing an initial ice thickness condition and starting the simulation directly into the melting period. Thus, the subsequent simulations discussed here were all run with an initial uniform ice thickness of 0.35m and subjected to "spring" conditions right away. The following schematic details the final base case components in red outline alongside the other runs tested at the same time (Figure B-1).

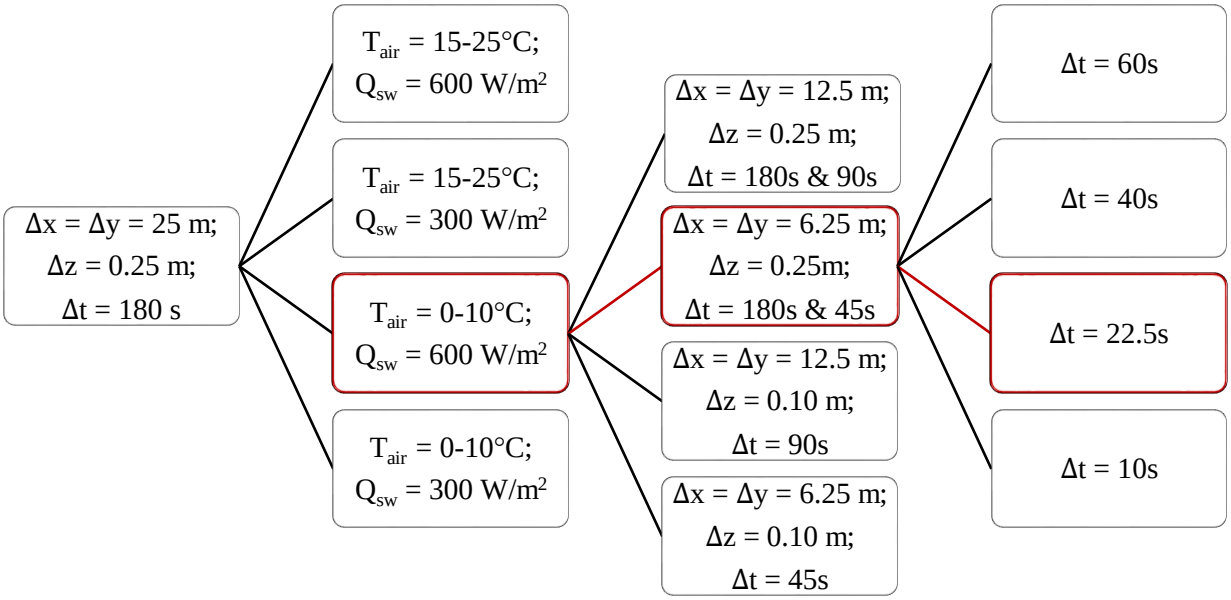

Figure B-1. Schematic of test runs performed with varied meteorological input, grid resolution, and time step in development of the base case

The impact of extreme vs mild meteorological input was checked by varying the air temperature (T_{air}) and solar radiation (Q_{sw}). Mean temperatures of 5°C and 20°C were considered to represent lower and higher ranges of realistic spring conditions, while the solar radiation was tested at the 5-year peak average calculated from Kingston, ON weather data of 600 W/m^2 as well as half of this value at 300 W/m^2. As shown in Figure B-2, the warmer air temperatures caused all the ice to melt within 8-10 days, whereas the milder temperatures prolonged the melting period. The effect of the solar radiation on increasing/decreasing the melting period was much weaker when air temperatures are higher but for the 0-10°C conditions, the lower solar radiation stretched the melting period beyond 2 months. The higher air temperatures were concluded as undesirable for the intended analysis since they only allow for about 2 weeks of

output. Between the 0-10°C air temperature runs, the 600 W/m^2 peak solar radiation input was chosen because a melting period of around 1.5 months was found to be enough time to obverse melting trends and this peak solar-radiation value was also validated to be close to realistic peak values.

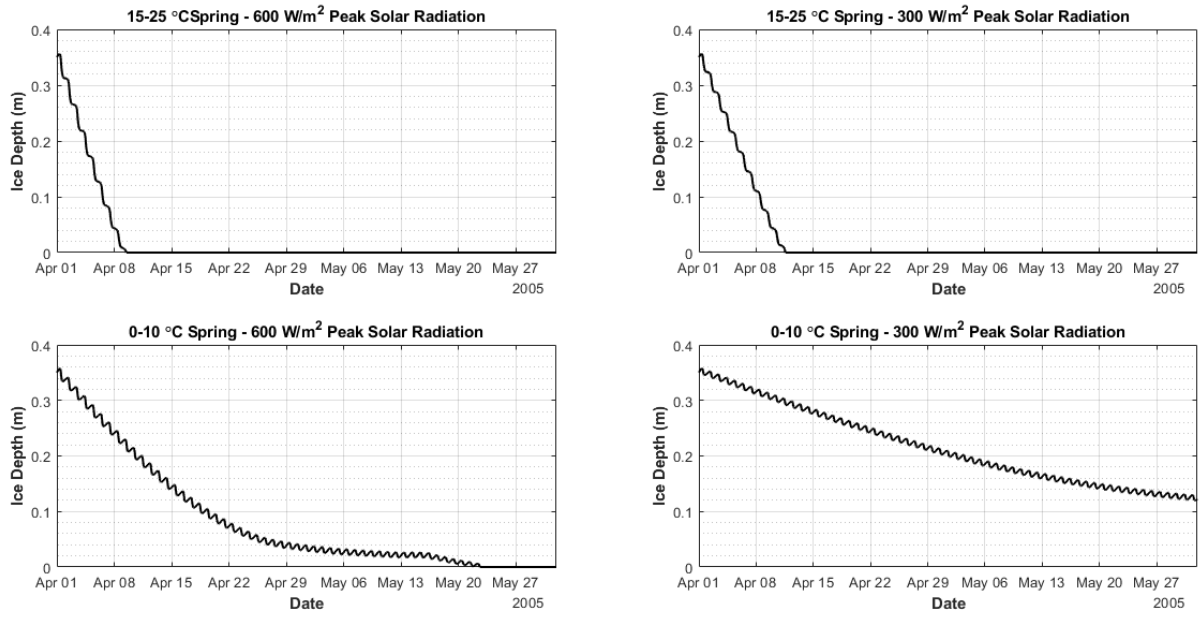

Figure B-2. Centre ice thickness in time for extreme and mild air temperature and solar radiation combinations, tested for the 25m horizontally spaced and 0.25m vertically spaced case with 180s time step

The horizontal resolution was investigated to address the possibility of spatial aliasing from the grid being too coarse and to ensure that the simulations resolved significant flow features. The horizontal resolution was tested at a half (12.5m) and a quarter (6.25m) of the original spacing. Figure B-3 shows the average temperature of a curtain through the centre of the lake, with solid lines representing runs with the time step kept consistent at 180s and dashed lines indicating the runs with the time step halved and quartered to match the change made to the

horizontal resolution. The highest resolution run at 6.25m is very different for a time step of 180s where it is clear the model is unstable with such a high time step; however, the remaining runs were all very similar. With the matching reductions made to the time step, the lines are observed to converge better. On May 1st, for instance, the difference in temperature as resolution decreased between the dashed red to dashed black line is 0.2°C. Since the overall results do not change much with the finest grid, a smaller spacing was not tested and a horizontal resolution of 6.25m was chosen. We subsequently varied the vertical resolution, and smaller vertical resolution also did not greatly change the mean temperature, thus the larger spacing of 0.25m was chosen because it reduced by run times by approximately half.

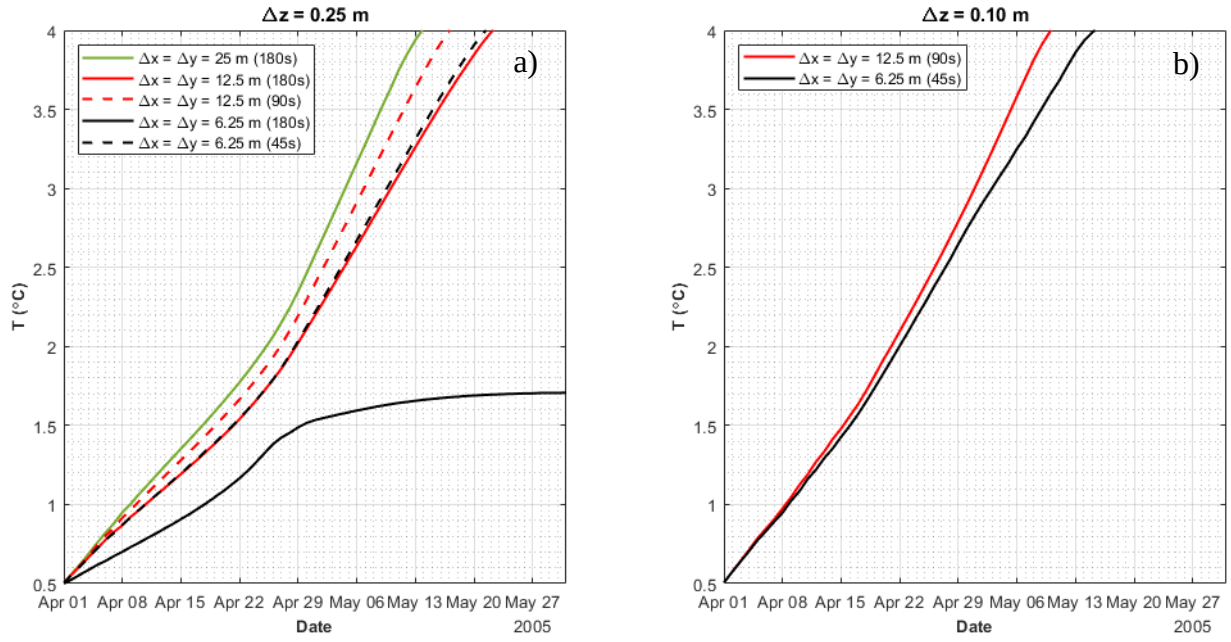

Figure B-3. (a) Centre mean temperature (daily averaged) for horizontal resolution tests of 25m, 12.5m (both 180s and 90s time step) and 6.25m (both 180s and 45s time step) for vertical resolution of 0.25m; (b) Centre mean temperature (daily averaged) for horizontal resolution tests of 12.5m (90s time step) and 6.25m (45s time step) for vertical resolution of 0.10m;

Finally, with the chosen horizontal and vertical resolution of 6.25m and 0.25m, respectively, the time step was tested to ensure the Courant-Friedrichs-Lewy (CFL) condition was satisfied. Figure B-4 provides the mean centre temperature and CFL for time steps of 60s, 40s, 22.5s, and 10s. Each run resulted in very similar temperature profiles as well as CFL <1, but it wasn't until a time step of 22.5s that the temperature profile mostly overlapped with the next time step reduction of 10s (<0.1°C difference for the entire simulation period), so this value was selected.

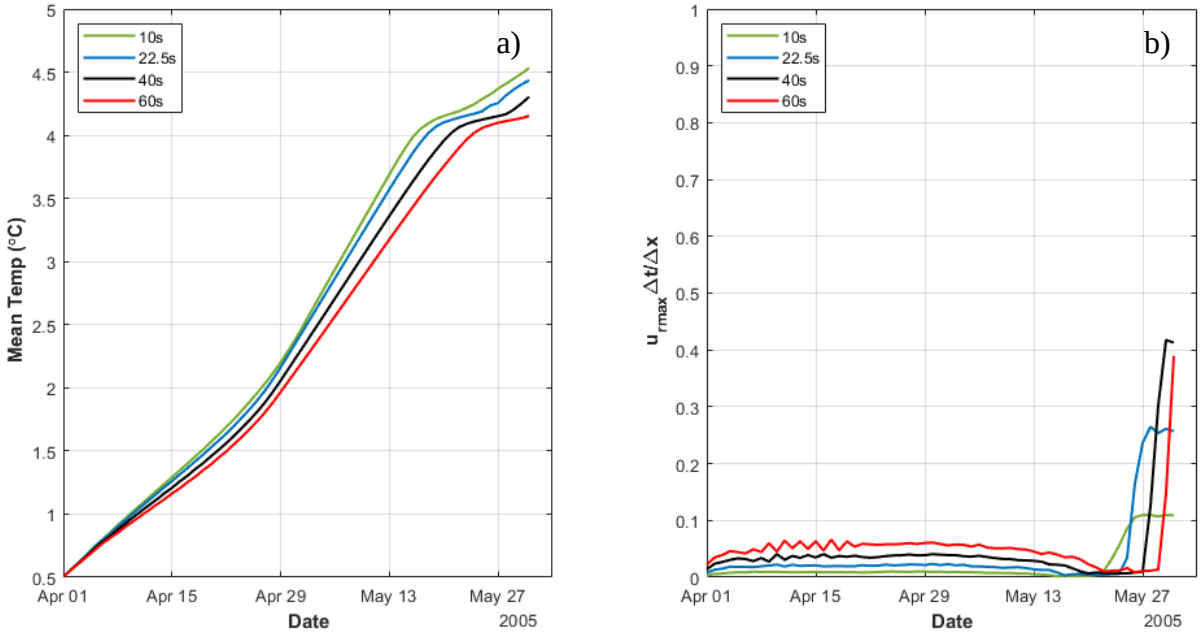

Figure B-4. (a) Centre mean temperature (daily averaged) and (b) CFL for time steps tests of 60s, 40s, 22.5s, and 10s

Appendix C

Additional Slope Case Figures

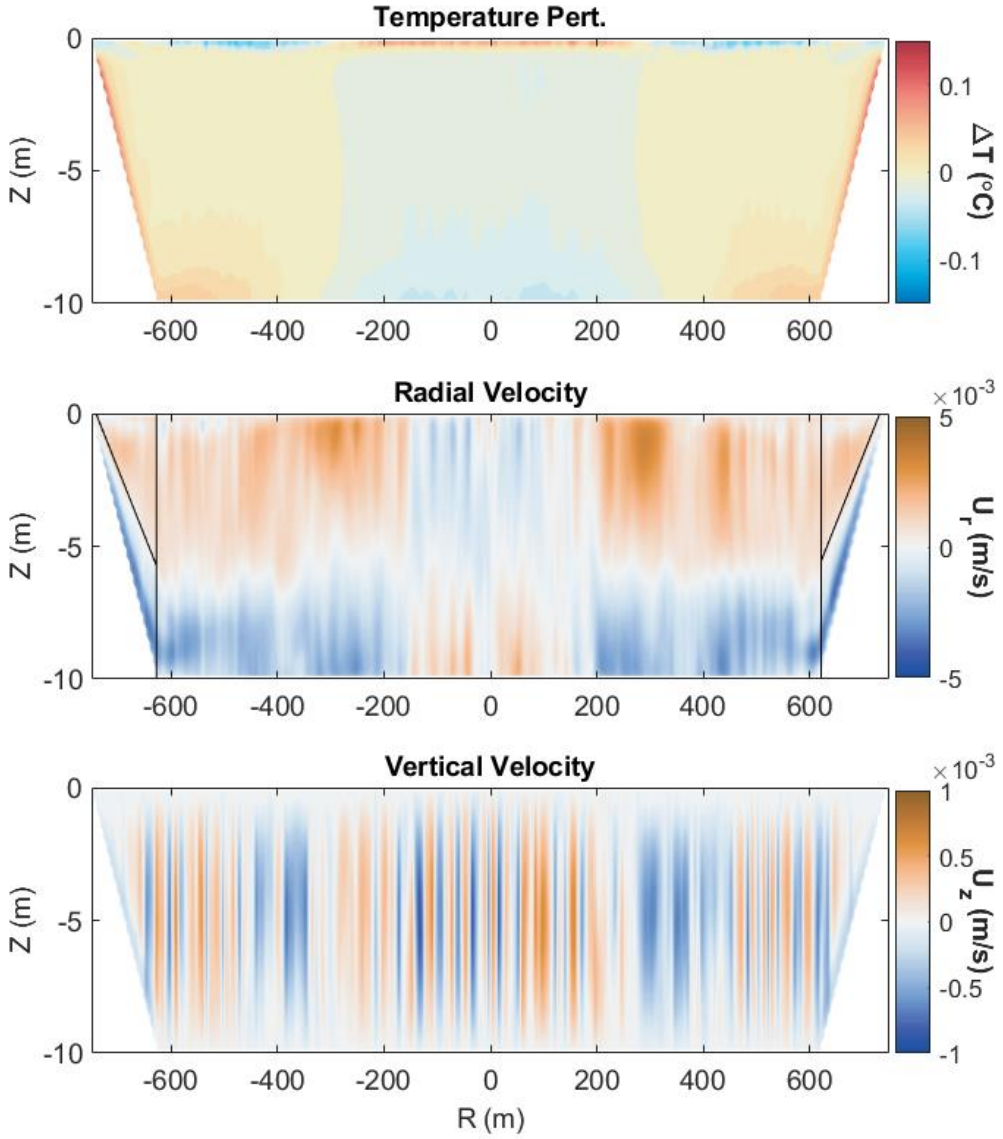

Figure C- 1. Hydrodynamics of Slope 2 in a daily-averaged snapshot of the cut off date of the simulation of May 5th: (a) temperature perturbation, (b) radial velocity with black lines denoting the boundaries to three key regions of the lake, and (c) vertical velocity

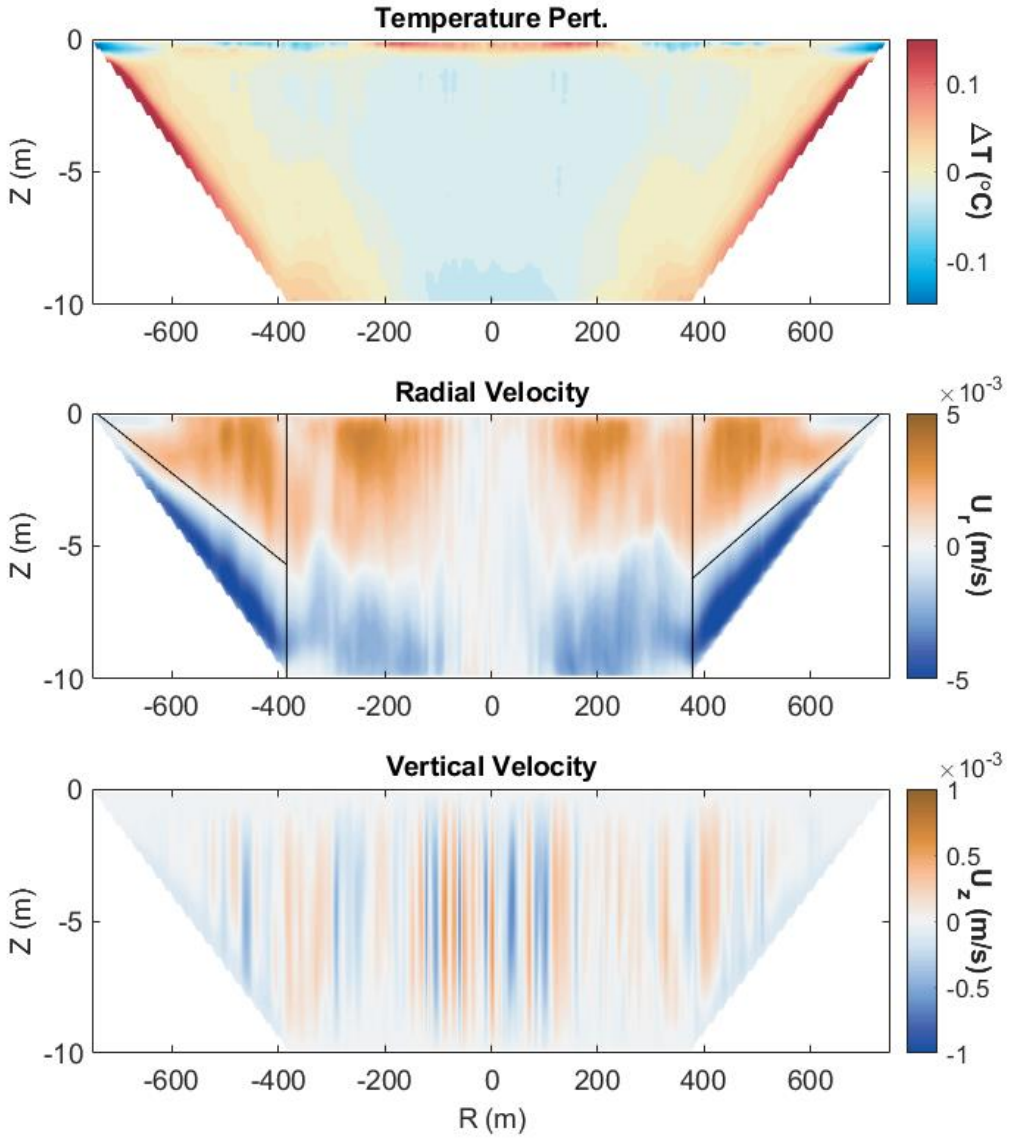

Figure C- 2. Hydrodynamics of Slope 4 in a daily-averaged snapshot of the cut off date of the simulation of May 5th: (a) temperature perturbation, (b) radial velocity with black lines denoting the boundaries to three key regions of the lake, and (c) vertical velocity

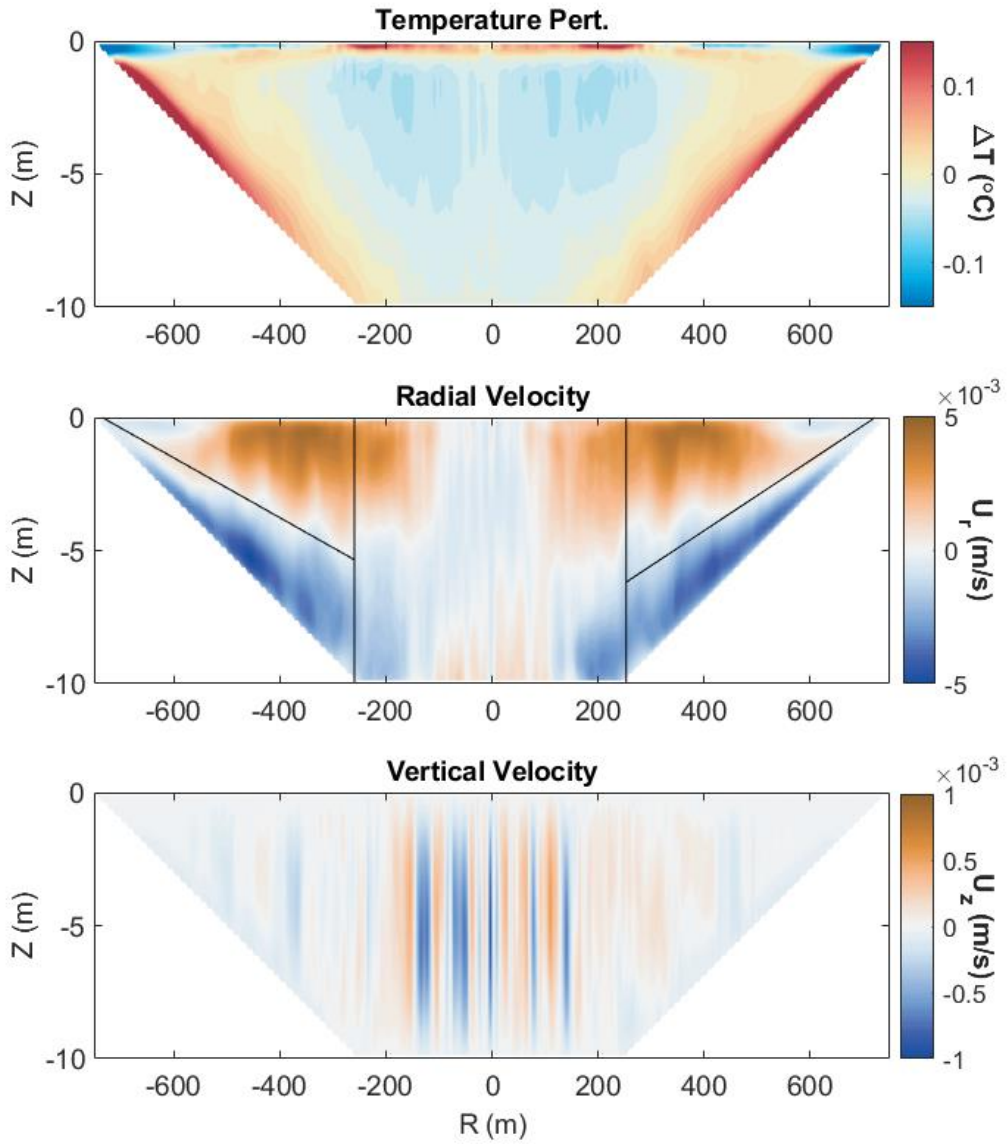

Figure C- 3. Hydrodynamics of Slope 5 in a daily-averaged snapshot of the cut off date of the simulation of May 5th: (a) temperature perturbation, (b) radial velocity with black lines denoting the boundaries to three key regions of the lake, and (c) vertical velocity

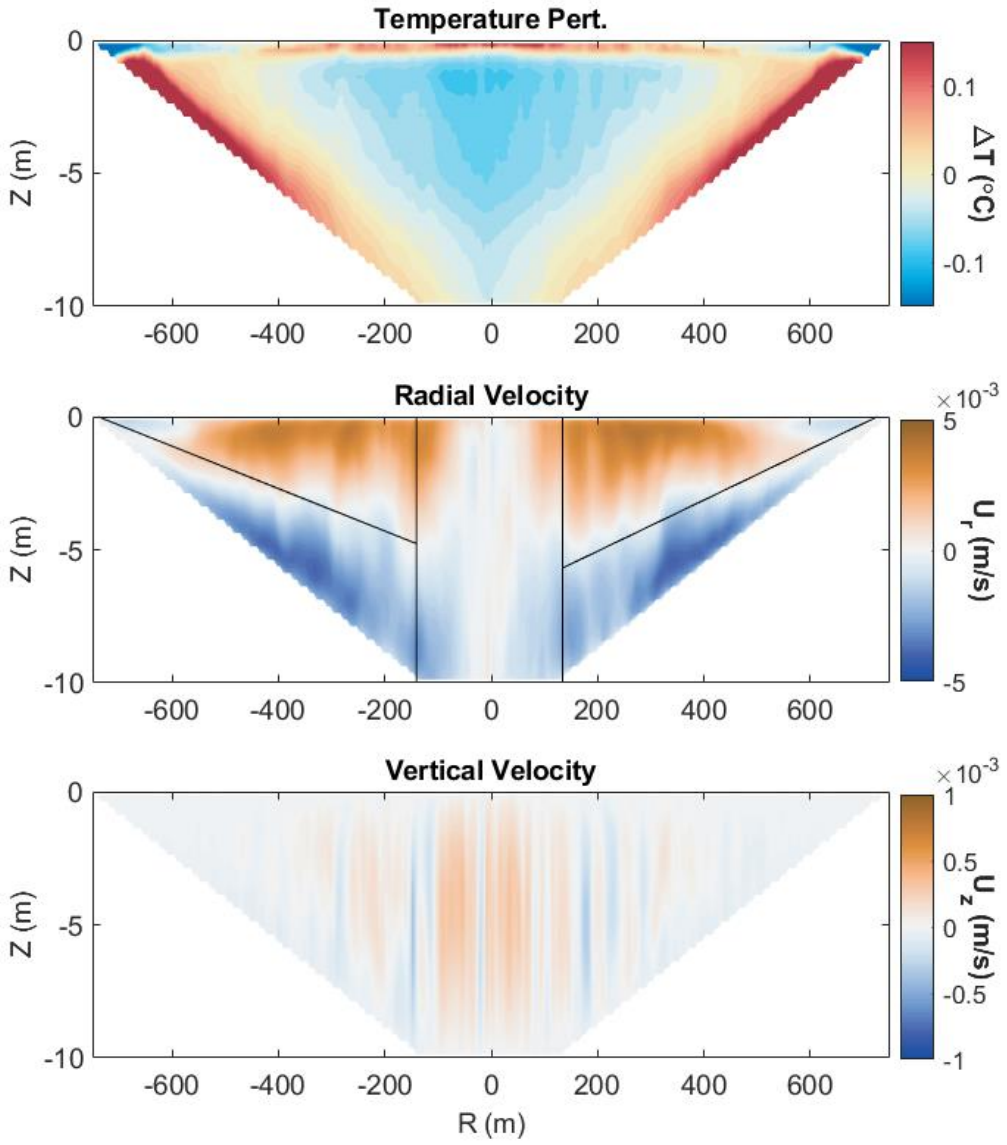

Figure C- 4. Hydrodynamics of Slope 6 in a daily-averaged snapshot of the cut off date of the simulation of May 5th: (a) temperature perturbation, (b) radial velocity with black lines denoting the boundaries to three key regions of the lake, and (c) vertical velocity

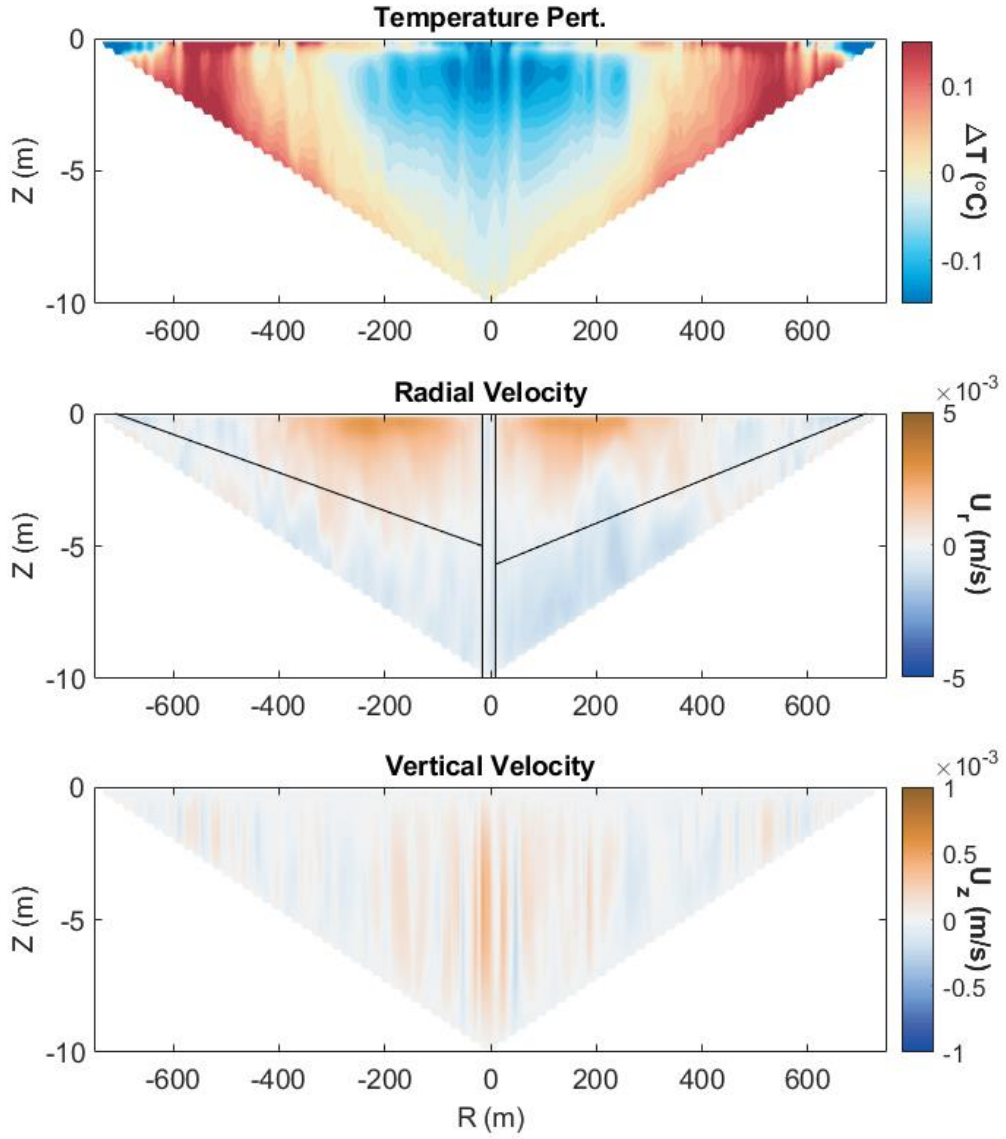

Figure C- 5. Hydrodynamics of Slope 7 in a daily-averaged snapshot of the cut off date of the simulation of May 5th: (a) temperature perturbation, (b) radial velocity with black lines denoting the boundaries to three key regions of the lake, and (c) vertical velocity

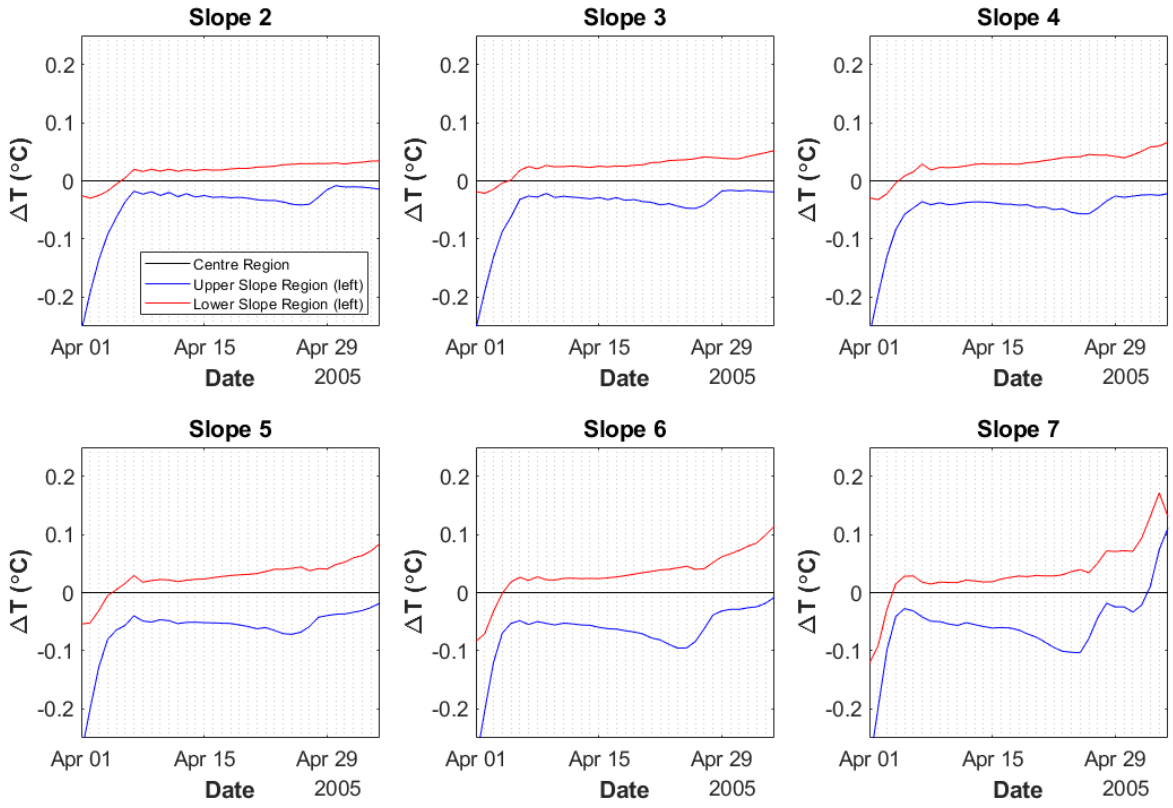

Figure C- 6. Average temperature in upper and lower layers of sloping region relative to the mean temperature of centre region (for all Slope cases, except cylinder bathymetry)

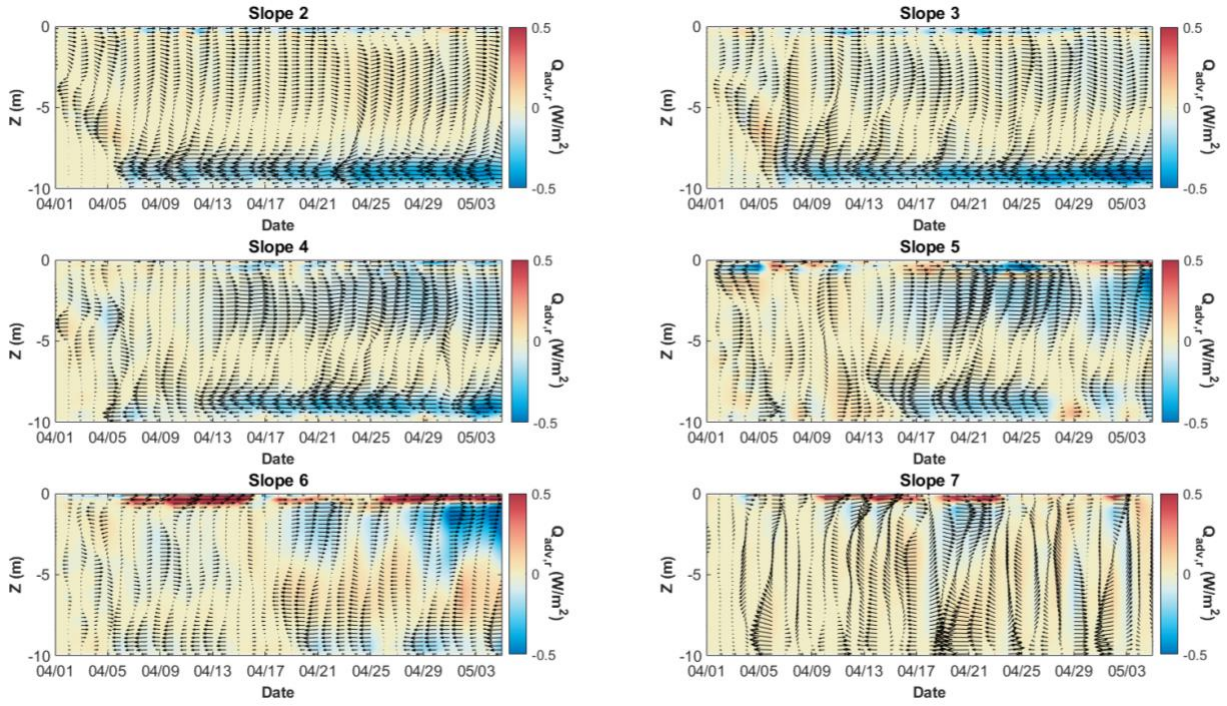

Figure C- 7. Advective heat flux based on temperature perturbation and radial velocity, plotted at the sloping/centre region boundary (for all Slope cases, except cylinder bathymetry)